

This work is protected by copyright and other intellectual property rights and duplication or sale of all or part is not permitted, except that material may be duplicated by you for research, private study, criticism/review or educational purposes. Electronic or print copies are for your own personal, non-commercial use and shall not be passed to any other individual. No quotation may be published without proper acknowledgement. For any other use, or to quote extensively from the work, permission must be obtained from the copyright holder/s.

Convective boundary structure and mixing in stellar interiors

Laura Jane Alexandra Scott

Doctor of Philosophy

Keele University

October 2021

Abstract

The treatment of convection remains one of the key uncertainties in stellar evolution. In particular, mixing processes at the boundaries of convective regions are complex and difficult to define analytically. Therefore, hydrodynamic simulations are used to model fluid flow in convective regions and the neighbouring stable regions, allowing the convective boundary mixing to be characterised. Hydrodynamic simulations currently provide the most accurate modelling of convection and convective boundary mixing, but are limited to time-spans which are a negligible fraction of the stellar lifetime. One way of mitigating this limitation is to transfer the key results of hydrodynamic simulations into 1D evolution models, which are able to model the whole life of a star. This is the aim of this thesis, in which two forms of convective boundary mixing (turbulent entrainment and convective shear) have been implemented into the Geneva stellar evolution code.

The entrainment prescription has been used to compute a grid of models from $1.5 M_{\odot}$ to $60 M_{\odot}$ on the main sequence. These were compared both to standard 1D models and to observational limits on the main sequence width. The strength of mixing due to entrainment was found to increase with mass, in line with observational evidence. The convective boundaries in previously calculated hydrodynamic simulations of the carbon shell have been reanalysed and compared to 1D convective shear models. It was found that the boundary shapes seen in the hydrodynamic simulations can be better modelled using an additional layer of mixing above the shear layer. Finally, a more general, multi-layered boundary structure has been discussed and future work outlined.

Acknowledgements

I would like to thank my supervisor Raphael Hirschi for his support and encouragement during my time as his student, particularly during the long periods of social isolation in the pandemic. I would also like to thank the other staff and PhD students in the physics department at Keele University, who have been great friends since I first arrived.

Chapter 4 was formed from a recent publication in MNRAS (Scott et al. 2021). Whilst the content of the paper was produced by me, the discussion of the models and results by the co-authors provided a valuable contribution. These co-authors are Raphael Hirschi, Cyril Georgy, David Arnett, Casey Meakin, Etienne Kaiser, Sylvia Ekström and Norhasliza Yusof. The developers of the Geneva code, particularly Cyril Georgy and Sylvia Ekström, have been very helpful in answering my questions on the code, and also developed plotting tools for the models which have been used extensively in this thesis. The plots involving 3D simulation results in Ch. 5 were adapted from scripts by Andréa Cristini and Federico Rizutti.

Contents

Abstract	i
Acknowledgements	ii
1 Introduction	1
1.1 Importance of convection in stellar evolution	1
1.2 The problem of convective boundary mixing	4
2 Theory	11
2.1 Overview of convection	11
2.2 Modelling convection	16
2.2.1 Multi-dimensional modelling	16
2.2.2 1D modelling using mixing length theory	19
2.3 Convective boundaries	25
2.3.1 Boundary location	25
2.3.2 Convective boundary mixing	26
3 The Geneva stellar evolution code	33
3.1 Overview of GENEC	33
3.2 Convection in GENEC	35
3.3 New convective boundary mixing prescriptions	37
3.3.1 Changes related to entrainment	37
3.3.2 Changes related to convective shear	40
3.4 Resolution	41
4 Models with entrainment	47
4.1 Methods	48
4.1.1 Entrainment law algorithm	48
4.1.2 Geneva code model grid	50
4.2 Results	53
4.2.1 Time dependence of boundary penetrability and mass entrain- ment rate	53
4.2.2 Mass dependence of boundary penetrability	57
4.2.3 Dependence of entrainment on the entrainment law parameters	59
4.2.4 Impact of entrainment on main sequence width	63
4.2.5 Impact of entrainment on helium core masses and lifetimes	67
5 Models with shear mixing	70
5.1 3D carbon shell models	70
5.2 1D main sequence models	81
5.3 Carbon shell comparison of 3D and 1D models	88
6 Discussion	98

6.1	Entrainment	98
6.2	Shear	103
6.2.1	Behaviour of the 1D shear models compared to other CBM types	103
6.2.2	Mechanism of mixing at the boundary	109
6.3	Modelling the multi-layered boundary	111
7	Conclusions	118
7.1	Thesis Summary	118
7.2	Future work	120
	Bibliography	122

List of Figures

1.1	Size of convection zones in the Sun compared to a main sequence $15 M_{\odot}$ star.	2
1.2	Convection zones throughout the evolution of a $15 M_{\odot}$ star.	3
1.3	Effect of CBM on main sequence evolutionary tracks.	5
1.4	Spectroscopic Hertzsprung-Russell diagram for galactic stars with overlaid model tracks (Fig. 1 from Castro et al. 2014).	7
2.1	Diagram of adiabatic versus non-adiabatic convection.	13
2.2	A selection of hydrodynamic simulation visualisations.	18
2.3	Temperature gradients in a star with a convective core.	27
3.1	A schematic representation of the buoyancy jump integration region in GENE.	39
3.2	A schematic representation of convective shear CBM	42
3.3	Variation of main sequence lifetime with spatial resolution.	44
3.4	Variation of main sequence lifetime with temporal resolution.	46
4.1	Time evolution of the bulk Richardson number for $15 M_{\odot}$ models with either the default step overshoot parameter $\alpha_{ov} = 0.1$ or entrainment parameters $A = 10^{-4}$ and $n = 1$	54
4.2	Profiles of the buoyancy frequency at three different central hydrogen mass fractions	56
4.3	Mass dependence of the Bulk Richardson number and its components	58
4.4	Comparison of the evolution of the convective core mass for $2.5 M_{\odot}$ models with step overshoot and entrainment	59
4.5	Minimum value of effective temperature on the main sequence for models with entrainment and step overshoot	62
4.6	Spectroscopic HRD in the mass range 8 to $32 M_{\odot}$ with $\alpha_{ov} = 0.1$ step overshoot and two entrainment values, $A = 10^{-4}$ and 2×10^{-4}	63
4.7	Final helium core mass, M_{He} , for various values of step overshoot α_{ov} and entrainment parameter A	66
4.8	Main sequence lifetime of various entrainment and step overshoot models relative to the default step overshoot models	68
5.1	Structure diagram showing the initial 1D model for the 3D carbon shell simulations (Fig. 1 from Cristini et al. 2017), with the time and location of the 3D simulations marked.	72
5.2	Profiles of average atomic mass and its spatial derivatives at the convective boundaries of the 1000 times boosted 3D carbon shell simulation.	74
5.3	Individual profiles of mean atomic mass for the 1000 times boosted 3D carbon shell simulation.	76

5.4	Profiles of horizontally-averaged mean atomic mass and its spatial derivative for 3D carbon shell simulations with four different boosting factors.	78
5.5	Logarithm of the change in mean atomic mass with respect to the convective region value against radius for the 3D carbon shell simulations.	79
5.6	Comparison of boundary shape normalised by boundary width in 3D carbon shell simulations for four different boosting factors.	80
5.7	Example profiles of the diffusion coefficient for models with shear mixing.	84
5.8	Time evolution of the mass of the shear mixing region on top of the convective core for a $15 M_{\odot}$ model.	85
5.9	Spectroscopic Hertzsprung-Russell diagram of the shear model grid along with some step overshoot models for comparison.	87
5.10	Profile of the diffusion coefficient in a 1D carbon shell model with shear mixing.	89
5.11	Profiles of average atomic mass and its spatial derivative at the convective boundaries of the carbon shell for two 1D models with shear mixing and the 1000 times boosted 3D simulation.	91
5.12	Comparison of boundary shape normalised by boundary width for two 1D models with shear mixing and the 1000 times boosted carbon shell simulation.	92
5.13	Profiles of average atomic mass and its spatial derivative at the convective boundaries of the carbon shell for two 1D models with double- f shear mixing and the 1000 times boosted 3D simulation.	93
5.14	Profiles of average atomic mass and its spatial derivative at the convective boundaries of the carbon shell for two 1D models with shear mixing (single- and double- f) and the 1000 times boosted 3D simulation. . . .	95
5.15	Comparison of boundary shape normalised by boundary width for 1D shear mixing (single- f and double- f) and the 1000 times boosted 3D carbon shell simulation.	96
6.1	Step overshoot parameter scaled according to the average convective velocity.	100
6.2	Minimum main sequence effective temperature for step overshoot, entrainment and shear models.	104
6.3	Main sequence lifetime for step overshoot, entrainment and shear models.	106
6.4	Helium core mass at the end of the main sequence for step overshoot, entrainment and shear models.	107
6.5	Diagram of proposed convective boundary sub-layers.	112
6.6	Profiles of mean molecular weight and buoyancy frequency for models with pure entrainment and a combination of entrainment and shear. . .	114

List of Tables

- 3.1 Number of grid points on the main sequence for step overshoot and entrainment models. 44
- 3.2 Number of main sequence time steps for step overshoot and entrainment models. 45
- 4.1 Summary of the CBM parameters used in the entrainment model grid along with key quantities. 52
- 5.1 Summary of the CBM parameters used in the shear model grid along with key quantities. 82
- 6.1 Properties of models on the main sequence with pure entrainment, pure shear and a combination of entrainment and shear. 113

1 Introduction

Convection is one of the most influential processes affecting stellar structure and therefore stellar evolution. It occurs during all stages of a star's life, yet it remains one of the key uncertainties in stellar evolution. The work in this thesis focuses on the boundaries of convective regions, both in terms of their structure and their effects on stellar evolution. Hydrodynamic simulation results have played a key part in shaping the mixing prescriptions implemented in the 1D code. This work therefore is part of a synergy between 1D and multidimensional models of stars (the 321D process).

1.1 Importance of convection in stellar evolution

Convection is ubiquitous in stellar evolution, affecting nearly all parts of a star's life. Beginning on the main sequence, stars with masses $\gtrsim 1.1$ to $1.3 M_{\odot}$ have convective cores. Stars lower than this mass do not have convective cores, but do have convective envelopes. Fig. 1.1 shows the internal structure of the Sun, with its convective envelope, and a $15 M_{\odot}$ star at roughly the equivalent point in the main sequence. The orange region representing the convective envelope of the Sun encompasses the outer $\sim 30\%$ of its radius. Conversely, the dark blue region in the $15 M_{\odot}$ star is a convective core which occupies $\sim 15\%$ of its radius (this also happens to be comparable in size to the Sun). In terms of mass, however, the convective core of the $15 M_{\odot}$ star contains just under a third of its mass, whereas the Sun's convective region contains only around 2% of its total mass. This stark difference in density between convective envelopes and cores has consequences for the efficiency of the convective heat transport (see Sec. 2.1).

The effects of convection are greatest for stars with convective cores, since it allows the star to burn all the fuel throughout the core. In the case of stars of $\sim 1.7 M_{\odot}$ or smaller with convective cores, the core grows during the main sequence. More massive stars have a receding core. This receding core can be seen in Fig. 1.2, which shows a structure evolution (a. k. a. Kippenhahn) diagram of the evolution of

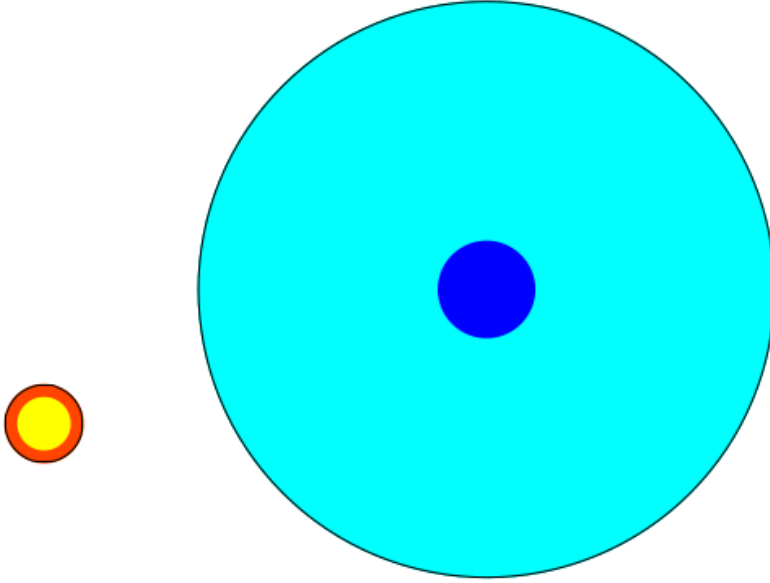


Figure 1.1: Slice through the Sun (*left*) showing the radial extent of its convection zone compared to a main sequence $15 M_{\odot}$ star (*right*). Here the darker regions are convective whereas the light regions are not convective.

a $15 M_{\odot}$ 1D stellar model, with convection zones shaded in grey. The y -axis extends from the core to just over halfway to the surface (in mass coordinates). The x -axis shows the time left until the last model time step is reached (during silicon burning¹). Since the evolution becomes faster as each burning stage progresses, the x -axis scale is logarithmic to allow the detail to be seen in the later phases.

In Fig. 1.2, convective core on the main sequence ($\gtrsim 10^6$ yr before last model) recedes from $\sim 6 M_{\odot}$ to just over $2 M_{\odot}$. Afterwards are a series of convective cores which are caused by the ignition of different fuels. These then progress to shells at higher mass coordinates as areas which still have significant amounts of fuel become hot enough for it to ignite. After the main sequence, a deep convective region forms in the outer layers due to the expansion and cooling of the envelope, which encompasses

¹Silicon burning is the last burning stage in massive stars. The order of burning goes as H, He, C, Ne, O and Si.

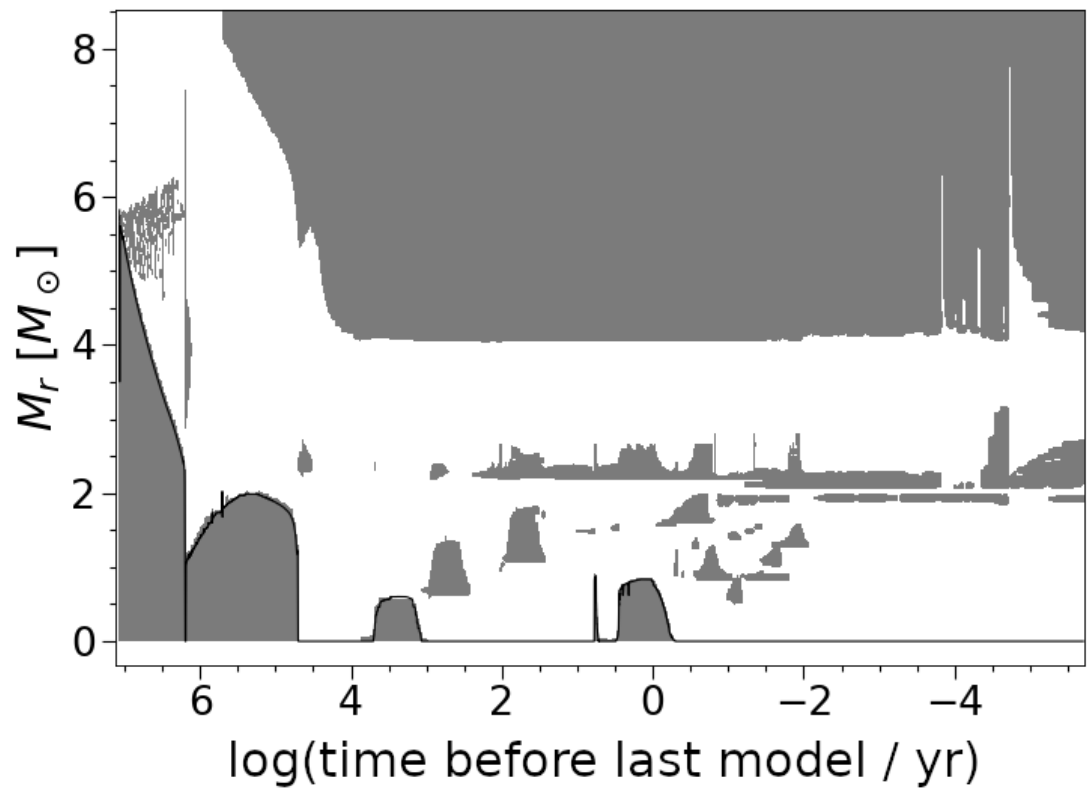


Figure 1.2: Convection zones throughout the evolution of a $15 M_\odot$ 1D stellar model. Convection zones are shaded in grey. The outermost parts of the model are not shown.

a significant fraction of the star’s mass. Convection in these three places (core, shell and envelope) occurs throughout the evolution and the star always has at least one convection zone in its interior.

1.2 The problem of convective boundary mixing

The boundary between convective and radiative zones presents a problem for 1D stellar models. Whilst local criteria do exist for determining the locations of convective boundaries (see Eqs. 2.27 and 2.28 in Ch. 2), convection is inherently a non-local phenomenon due to the inertia of the fluid in the convective region. The position of the boundary, defined in terms of where fluid velocities are effectively zero, may be some significant distance away from the formal boundary defined by local criteria, which use the location where buoyant acceleration is zero instead. The extent of this extra momentum-driven mixing, often called overshoot, can only be determined approximately from the global properties of the convective region. In addition, other mixing processes, such as instabilities at the boundary or waves rely on different physics which are also closely linked to the turbulent properties of convection. All these mixing processes will be referred to with the more general term convective boundary mixing (CBM) in this thesis.

The principal effect of CBM is to increase the effective size of the convective region. In the case of convective regions associated with nuclear fusion, this increases the amount of fuel available for burning. It also changes the evolutionary track on the Hertzsprung-Russell diagram (HRD). Fig. 1.3 shows an example of this effect on the main sequence for two $15 M_{\odot}$ stars, where only one of the models includes CBM. In this case, the core has been extended by a tenth of a pressure scale height, meaning that the model is able to build up a larger mass of helium at the end of the main sequence and has a longer main sequence lifetime. The two y -axis scales are the luminosity and the spectroscopic luminosity \mathcal{L} (Langer & Kudritzki 2014), given by

$$\mathcal{L} = \frac{T_{\text{eff}}^4}{g}. \quad (1.1)$$

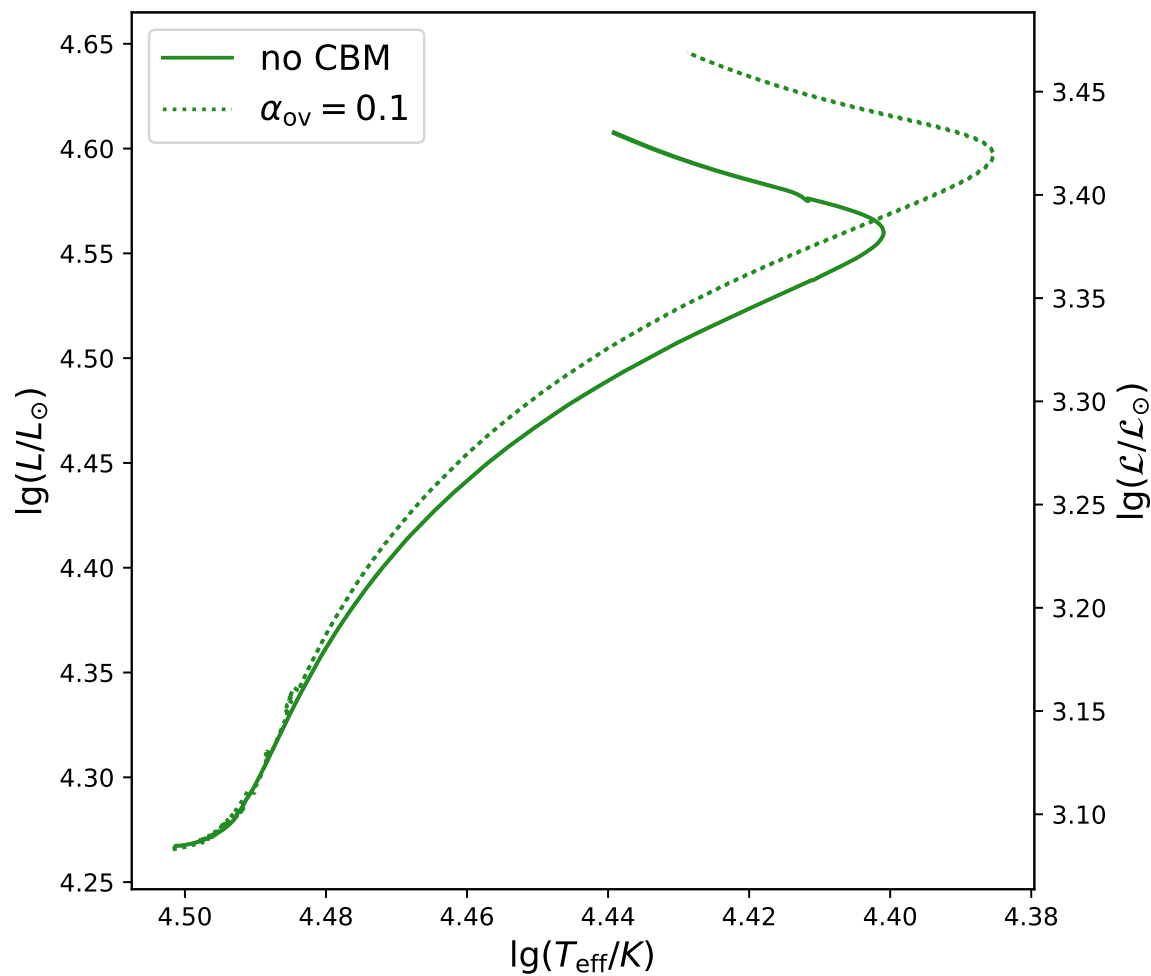


Figure 1.3: Hertzsprung-Russell diagram for two $15 M_{\odot}$ stellar models on the main sequence, one with CBM and one without. The y -axis scales are luminosity, L (*left*), and spectroscopic luminosity, \mathcal{L} (*right*).

where T_{eff} is the effective temperature and g is the surface gravity of the star.

Convection and CBM in 1D evolution codes is parameterised, so calibration of these parameters to observations is important for the accuracy of stellar models. For core convection, CBM increases the luminosity of stars and allows them to reach cooler temperatures before leaving the main sequence (Fig. 1.3). Both the luminosities and (via modelling of stellar atmospheric spectral lines) temperatures of stars are accessible to observation. Therefore, one important test of CBM is whether the models fit the observed positions of stars on the HRD. Observations of stars in clusters (which have formed from the same cloud and thus can be assumed to have the same age) can be compared to isochrones made from grids of models with different amounts of mixing, as done by e.g. Maeder & Mermilliod (1981). The necessary amount of convective core extension can be deduced from which models are able to fit single isochrones. Another use of the HRD in calibrating CBM is the main sequence (MS) width, that is the span in temperature of the MS on the HRD. Stronger core CBM in the models produces a wider MS, which can then be fitted to observations to retrieve the correct CBM parameter, similarly to the isochrone fitting (Schaller et al. 1992; Ekström et al. 2012).

Figure 1.4 shows an example of observed spectroscopic HRD (sHRD) positions of 575 galactic stars from Castro et al. (2014). This figure shows an example of CBM uncertainties in massive stars, since the models give a main sequence width (between the dashed orange and purple lines) which does not match the observed main sequence width (black dashed lines). The empirical cool edge of the main sequence seen in this figure will be revisited in Ch. 4.

CBM can also affect the lifetimes of various evolutionary stages. For example, the models with stronger CBM spend less time in the helium-burning phase compared to the MS than models with less CBM and in the later stages, the expansion of massive stars' carbon-rich cores by CBM reduces the lifetime of the WN stage of Wolf-Rayet stars compared to the WC stage (Maeder & Meynet 1989). The time spent by stars in the blue and red supergiant phases is also known to depend strongly on mixing (e.g. Langer & Maeder 1995; Georgy, Saio & Meynet 2014; Schootemeijer et al. 2019).

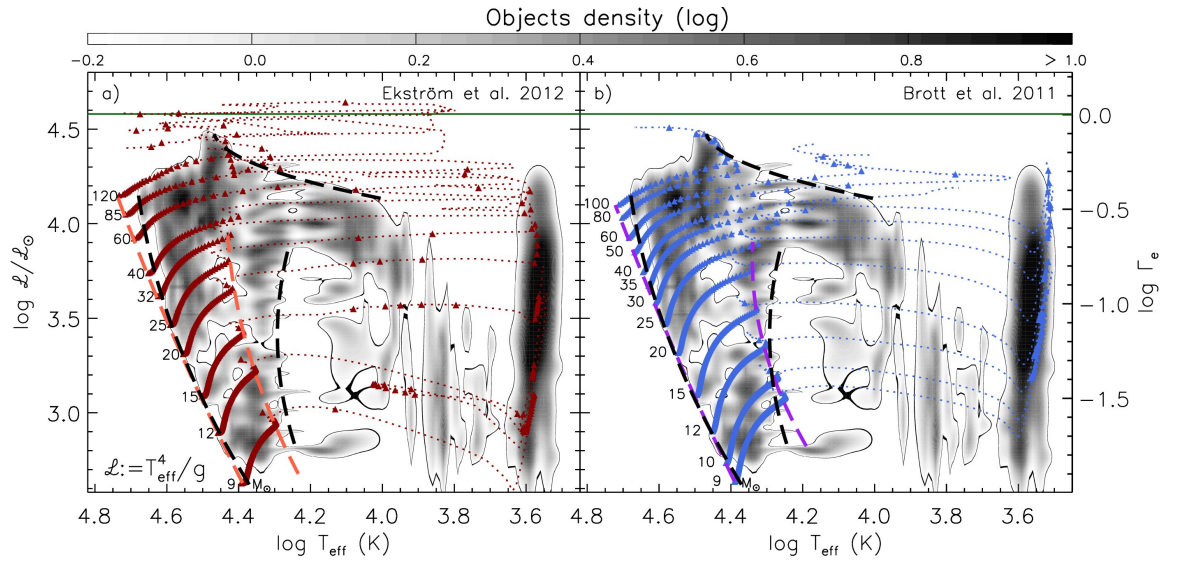


Figure 1.4: Spectroscopic Hertzsprung-Russell diagram for galactic stars with overlaid model tracks (Fig. 1 from Castro et al. 2014). The right y -axis is the Eddington factor (the ratio of the luminosity to the Eddington luminosity), which is proportional to the spectroscopic luminosity on the left axis. The grey shading represents the probability density distribution of the 575 galactic stars from the sample, whilst the coloured points and dotted lines are model tracks from **a)** Ekström et al. (2012) and **b)** Brott et al. (2011).

This is important because the amount of time stars spend in an evolutionary stage is reflected in the number of stars which populate that region of the HRD. One can expect to find that the ratio of the number of stars in one region compared to the other is roughly the same as the ratio of the lifetimes. This is useful so long as the evolutionary phase of a star can be accurately determined from its position in the HRD, which can become difficult in the cooler parts.

Asteroseismology presents another method for testing CBM by observing the pulsation modes of stars. The frequencies of these modes are sensitive to the interior structure, which is affected by mixing. One type of asteroseismic mode is the p-mode (where the p stands for pressure). P-modes are acoustic in nature and so travel at the sound speed, which is mostly dependent on the ratio of temperature to mean molecular weight, T/μ ; this increases with depth in the star. Therefore, p-modes refract away from the centre of the star and are mostly sensitive to the structure in the outer regions. Sudden changes in the sound speed (such as would be found at the boundary of a convective region, where μ may change rapidly) affect the spectrum of p-modes excited in the star; this is reflected in the frequency spectrum and can be used to determine the position of the base of the convective envelope (Verma et al. 2014).

Another type of asteroseismic mode is the g-mode (where g stands for gravity). These waves have buoyancy as the restoring force and have a larger range of frequencies in regions with larger gradients in μ . They are unable to propagate in convective regions. This makes them useful probes for CBM, which is also able to affect g-mode frequencies by erasing μ gradients. G-modes are sensitive to the value of μ gradients throughout the star, so the strength of CBM can affect the asteroseismic frequencies predicted by models (Miglio et al. 2008). There are some stars with rich g-mode spectra, e.g. the slowly-pulsating B star KIC 7760680. The frequencies of this star were compared to models with different CBM prescriptions by Moravveji et al. (2016), who found that CBM modelled by an exponentially decaying diffusion coefficient provided a better fit to the data than a flat extension of the core. CBM parameters have been found for numerous single stars (e.g. Dupret et al. 2004; Desmet et al. 2009; Briquet et al. 2011; Aerts et al. 2003) as well as for ensembles of stars in

binary systems (Claret & Torres 2017; Claret & Torres 2019).

Apart from modes, asteroseismic observations may also be useful in constraining mixing due to internal gravity waves excited by the convective boundary. Edelmann et al. (2019) were able to produce a spectrum similar to the low-frequency power excess seen in asteroseismic spectra (Bowman et al. 2019). Further hydrodynamic simulations may be able to help characterise these waves by comparison to asteroseismic spectra.

If a single value of the parameter cannot fit the observations, it can suggest that another confounding factor in the models must be corrected first (e.g. improving opacity tables to include more metals, as in Iglesias & Rogers 1996). Alternatively, the CBM prescription may not describe the boundary physics adequately if a good fit to the observations cannot be reached. The fact that standard CBM prescription parameters seem to have mass dependence (Maeder & Mermilliod 1981; Ribas, Jordi & Giménez 2000; Castro et al. 2014) hints at boundary physics which is not yet well understood. The mass dependence of CBM will be explored in more detail in Ch. 4.

Hydrodynamic simulations represent an important way to study convection. In this case the CBM arises naturally from the fluid motion. The problem for stellar evolution is that hydrodynamic time scales required to resolve this fluid motion are very short compared to evolutionary time scales. A typical 3D hydrodynamic simulation may only simulate $\sim 10^7$ s of physical time, or significantly less depending on the evolutionary phase, before available computing resources are used up. 2D simulations are computationally cheaper and can offer a way to simulate longer stretches of time (see Tab. 1 in Pratt et al. 2020), but they still do not come close to stellar evolutionary time scales.

The role of modelling stellar evolution can thus currently only be done using 1D models, assuming spherical symmetry. However, convection is not a spherically symmetric process, so many of its features, including CBM, must be parameterised in 1D codes. The aim of this thesis is to use the results from hydrodynamic simulations to improve these CBM parameterisations.

Ch. 2 will provide more background on the current understanding of convection and convective boundary mixing, both through 1D and multidimensional modelling.

Chapter 3 will describe the Geneva stellar evolution code, which was used throughout this work. This chapter will also describe two additional convective boundary mixing prescriptions along with other extensions made to the code as part of this thesis work. Chapter 4 will then describe the results of one of these prescriptions, entrainment, on the main sequence. The other prescription, shear, will be described both on the main sequence and in the carbon shell burning stage in Ch. 5, where it will be compared to 3D simulation results. The implications of the results of Chs. 4 and 5 will be discussed in Ch. 6. Finally, Ch. 7 will summarise the thesis and discuss future work.

2 Theory

In this chapter, I will review convection in three parts: Sec. 2.1 will cover the physical properties of convection in stars, Sec. 2.2 will show how it is modelled and Sec. 2.3 will focus on the boundaries between convective and stable regions.

2.1 Overview of convection

Convection happens in a density-stratified medium when a fluid element is perturbed from equilibrium and has a density difference compared to its surroundings that causes it to continue travelling in the direction of the perturbation rather than returning to its previous equilibrium. As density differences drive the motion, the force that accelerates the fluid element is buoyancy. Whether or not convection is active depends on the temperature gradients, $\nabla = d \ln T / d \ln P$ (see Eqs. 2.27 and 2.28). If the temperature of a fluid element changes more slowly than its surroundings as it is perturbed, then its density will also change more slowly (this assumes that the speed of the element is much less than the sound speed, such that the pressure inside and outside the element can be considered to be equal, and that the fluid is chemically homogeneous). In this case, an element perturbed upwards would have a temperature excess over its surroundings and as such would be less dense than the surroundings also, and convection would set in.

Therefore, in terms of temperature gradient ∇ and absolute change in density along the path $|\Delta\rho|$, with subscripts e and s for the element and its surroundings respectively, there are two situations:

1. $\nabla_e > \nabla_s \implies |\Delta\rho_e| > |\Delta\rho_s|$, buoyancy acts against perturbation,
2. $\nabla_e < \nabla_s \implies |\Delta\rho_e| < |\Delta\rho_s|$, buoyancy acts to increase perturbation.

In situation 1, fluid elements are forced back to their equilibrium position, about which they oscillate. In situation 2, convection occurs, with the temperature gradient of the

surroundings being greater than that of isolated fluid elements. According to the inequality $\nabla_e < \nabla_s$, convection can be expected to take place in regions of a star where the background temperature changes rapidly, that is in places with either heat sources (e. g. nuclear fusion) or heat sinks (e. g. ionisation layers).

The second temperature gradient inequality also suggests that convection can occur for particularly low ∇_e . However in practice this is not important, since the minimum value for ∇_e is close to the adiabatic temperature gradient, which does not usually change much from its ideal gas monatomic value of 0.4 (apart from in regions such as the ionisation layers in the envelopes of some stars). If non-local effects are negligible, ∇_e is between the adiabatic temperature gradient, ∇_{ad} , and ∇_s .

To understand why this is the case, Fig. 2.1 shows how T and P change for a fluid element undergoing a perturbation in convection. In order for convection to occur, the temperature gradient of the surroundings, ∇_s , must be higher than the temperature gradient of the element, ∇_e ; thus the black lines (showing the temperature and pressure of the element as it is perturbed) have a smaller gradient than the pink line showing the temperature and pressure of the background. The element can either move adiabatically (solid black lines) or with some heat exchange with the surroundings (dashed black line). When heat exchange occurs between the element and the background, the temperature is intermediate between the background and the adiabat. Convection in which this occurs and $\nabla_e > \nabla_{\text{ad}}$ is called superadiabatic.

There is a temperature difference between the yellow elements at their final positions and the background temperature in Fig. 2.1; this difference is greater for adiabatic convection than superadiabatic. In either case, the element will eventually be subsumed into the surroundings, at which point it will transfer its heat excess (or lack) into the rest of the fluid. This process of heat transport is more efficient for adiabatic convection since the temperature excess of an element is greater for a given distance moved. Convective heat transport affects the background temperature gradient, reducing it to be closer to that of the convective elements.

The degree to which convection is adiabatic in stars depends on the importance of radiative heat transfer. This can be measured by the Péclet number, Pe , which

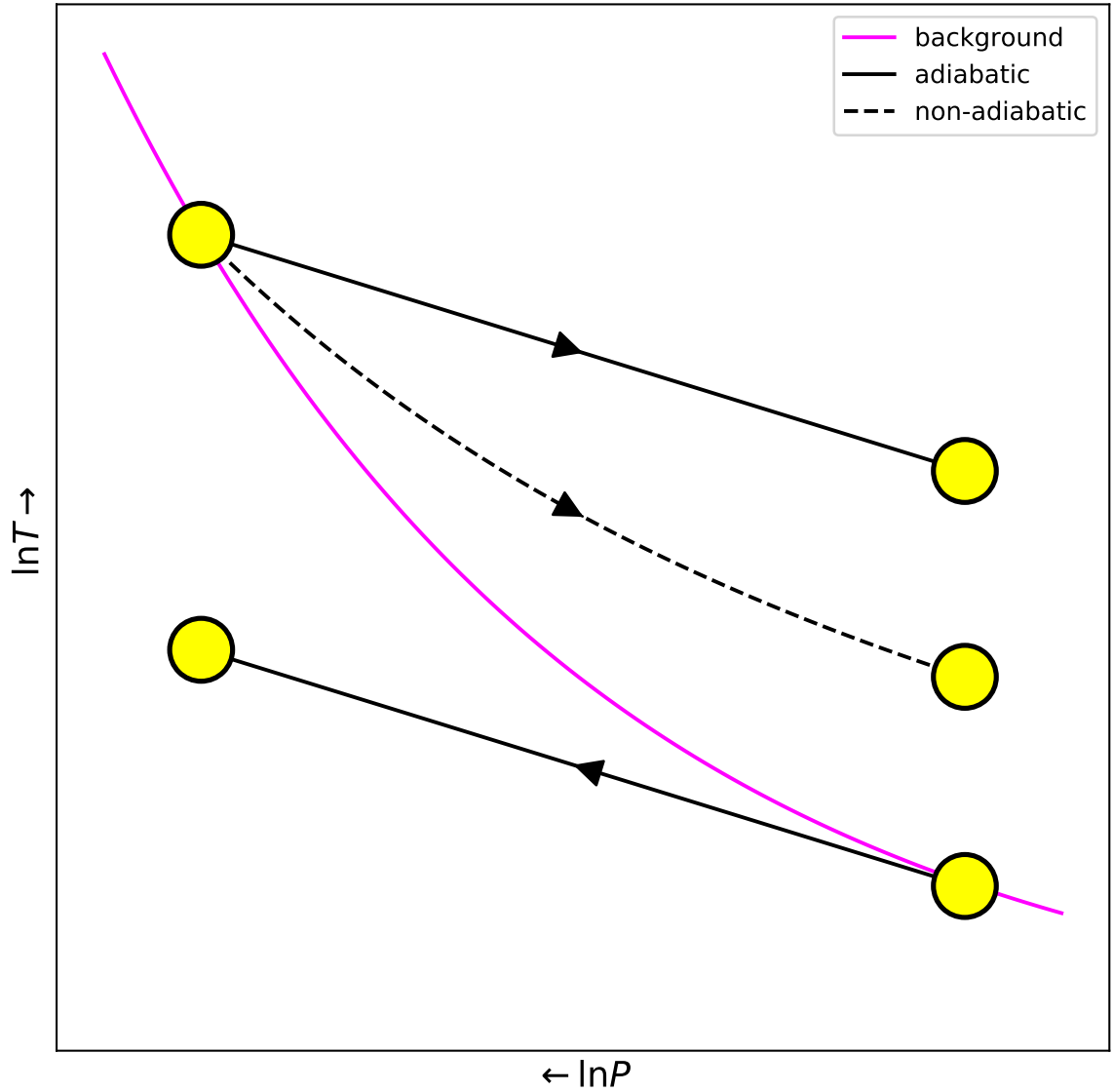


Figure 2.1: Diagram of adiabatic convection versus convection with some heat transfer between the element and the surroundings (non-adiabatic). The yellow bubbles show the start and end positions of elements as they are perturbed from the background temperature, T , and pressure, P . The solid black lines show how T and P change for elements expanding or contracting adiabatically as they move; both an upwards and a downwards perturbation are shown. Also shown with the dashed line is an upwards perturbation of an element which exchanges heat with the surroundings.

gives the ratio of timescales for radiative and advective heat transport. If $Pe \gg 1$, then radiative heat transfer between a convecting fluid element and its surroundings does not have enough time to act before the element moves a significant distance. In stellar interiors, Pe can be written as

$$Pe = \frac{lv}{K}, \quad (2.1)$$

where l and v are the typical length scale and velocity of advected elements and K is the thermal diffusivity, given by

$$K = \frac{4ac}{3} \frac{T^3}{\kappa\rho^2c_P}, \quad (2.2)$$

where a is the radiation density constant, c the speed of light, κ the Rosseland mean opacity, ρ the density and c_P the specific heat capacity at constant pressure. The dominant quantity in Eq. 2.2 is ρ^2 , since ρ changes so drastically from a star's surface to its upper layers compared to the other quantities. The result is that K becomes larger near the star's surface and Pe decreases correspondingly. This can also be understood as the mean free path of photons (which is approximately $1/\kappa\rho$) increasing as the density drops, allowing radiative transfer of energy to be more effective. Conversely, high density in the deep interior makes convective heat transfer very efficient, since even a small element of fluid can contain a lot of heat. Hence, the effects of radiative transfer on convection are more important in convective envelopes than in interiors. The temperature gradient is mostly superadiabatic in envelopes and is close to adiabatic in interiors. Determining the temperature gradient quantitatively requires a theory such as the mixing length theory (MLT), which will be described in Sec. 2.2.

It should be noted that even in the case of inefficient convection, chemical species can still be mixed effectively by the bulk advection characterising the flow. Thus, in the case of low Pe convection, chemical species are mixed well whilst entropy is not, whereas high Pe convection mixes both chemical species and entropy well.

In stars, convection is a turbulent process. Turbulence can be described as chaotic, where fluids move in many different directions, as opposed to laminar flow, in which layers of fluid move without disrupting each other. The degree to which a fluid

is turbulent can be described using the Reynolds number:

$$Re = \frac{vl}{\nu}, \quad (2.3)$$

where v and l are velocity and length scales typifying the flow, and ν is the kinematic viscosity. The viscosity on the denominator of Eq. 2.3 is governed by the collisions of ions inside a star and is defined as

$$\nu = l_{\text{mfp}}v_{\text{th}}, \quad (2.4)$$

where l_{mfp} is the mean free path between ion collisions and v_{th} is the thermal velocity. This gives typical stellar values of $\nu \sim 1 \text{ cm}^2 \text{ s}^{-1}$ (Kippenhahn & Weigert 1990). On the other hand, the numerator of Eq. 2.3 is much higher, with length scales of $\sim 10^8 \text{ cm}$ and velocities greater than 10^3 cm s^{-1} in convective regions. Thus stellar convection has $Re \gtrsim 10^{11}$ and can be considered highly turbulent.

According to Kolmogorov (1941), turbulent flows are characterised by a cascade of energy from the largest scales to the smallest as fluid structures are shredded. The largest length scale at which energy is injected is called the integral scale, Λ , whilst the smallest fluid structures are at the dissipation scale, λ . Below this scale, kinetic energy is converted into internal energy. The range of length scales between Λ and λ is called the inertial range. In the case of stellar convection, the heat source or sink sets large structures into motion, which then break up into smaller pieces before dissipating completely elsewhere in the star, contributing to the transport of heat, chemical species and angular momentum. With the assumption of homogeneous, isotropic turbulence, Kolmogorov showed that the rate of energy dissipation at the smallest scales, ϵ , can be related to the velocity of the largest scales, v , and the integral scale by the relation

$$\epsilon \sim \frac{v^3}{\Lambda}. \quad (2.5)$$

Thus, turbulent convection can be considered to be driven by large scale motions to the degree that the convection is homogeneous and isotropic. These conditions are generally true in the bulk of a stellar convective region, although they begin to break down at the boundaries.

2.2 Modelling convection

2.2.1 Multi-dimensional modelling

Modelling stellar convection numerically allows insight into how convection affects stellar evolution. As a chaotic, turbulent process, the details of convection are best captured with multi-dimensional hydrodynamic simulations. These simulations model the fluid flow directly. The fluid equation of motion used in the simulations is usually derived from the Navier-Stokes equation of motion, with various forms resulting from different assumptions. For a homogeneous, viscous and compressible fluid, the Navier-Stokes equation is

$$\rho \left[\frac{\partial \mathbf{v}}{\partial t} + (\mathbf{v} \cdot \nabla) \mathbf{v} \right] = -\nabla P + \rho \mathbf{g} + \eta \nabla^2 \mathbf{v} + \left(\xi + \frac{1}{3} \eta \right) \nabla (\nabla \cdot \mathbf{v}), \quad (2.6)$$

where t is time, η is the dynamic viscosity (related to the kinematic viscosity by $\nu = \eta/\rho$) and ξ is the second viscosity, a component of the viscous stress tensor (Eq. 15.3 in Landau & Lifshitz 1959). In the case of an incompressible fluid, the last term of Eq. 2.6 can be neglected. If the viscosity η is considered negligible, then the third term on the right hand side disappears also, giving the Euler equation

$$\frac{\partial \mathbf{v}}{\partial t} + (\mathbf{v} \cdot \nabla) \mathbf{v} = -\frac{1}{\rho} \nabla P + \rho \mathbf{g}. \quad (2.7)$$

Whether these simplifications are suitable depends on the requirements of the simulation. For example, the assumption of incompressibility is valid as long as the Mach number of the convection is $\ll 1$. For high Mach flows, acoustic energy flux becomes important, which requires compressibility. Similarly, the assumption of zero viscosity required for the use of the Euler equation is only valid so long as the length scales simulated do not approach the Kolmogorov dissipation scale at which viscosity becomes important.

Other necessary equations include mass conservation, energy transfer and (in the case of multi-component fluids) an equation for the mixing of nuclear species. For the PROMPI code (Meakin & Arnett (2007), used by Cristini et al. (2019) in the simulations

analysed in Ch. 5) the equations solved are

$$\frac{\partial \rho}{\partial t} + \nabla \cdot (\rho \mathbf{v}) = 0; \quad (2.8a)$$

$$\rho \frac{\partial \mathbf{v}}{\partial t} + \rho \mathbf{v} \cdot \nabla \mathbf{v} = -\nabla P + \rho \mathbf{g}; \quad (2.8b)$$

$$\rho \frac{\partial E}{\partial t} + \rho \mathbf{v} \cdot \nabla E + \nabla \cdot (P \mathbf{v}) = \rho \mathbf{v} \cdot \mathbf{g} + \rho(\epsilon_{\text{nuc}} + \epsilon_{\nu}); \quad (2.8c)$$

$$\rho \frac{\partial X_i}{\partial t} + \rho \mathbf{v} \cdot \nabla X_i = R_i, \quad (2.8d)$$

where E is the total energy, ϵ_{nuc} and ϵ_{ν} are the energy generation rates due to nuclear burning and neutrino losses respectively, X_i is the mass fraction of nuclear species i and R_i is the corresponding rate of change of mass fraction for that nuclear species.

With Eqs. 2.8a to 2.8d or some variants, multidimensional hydrodynamic simulations are able to produce a detailed view of convection. A selection of snapshots from simulations of convection are presented in Fig. 2.2, showing some of the diversity in the simulation setup and the information available from them. Fig. 2.2a (Cristini et al. 2017; Arnett et al. 2019) shows the box-in-a-star setup, in which a small portion of a star is simulated (simulations of this type will be revisited in Ch. 5). The geometry of this setup is advantageous for the resolution of the convective boundaries. The colour scale shows velocity magnitude, clearly showing the convective region and the stable regions above and below. Fig. 2.2b (Pratt et al. 2020) shows a wedge setup, which is similar to a box but with the advantage of non-plane-parallel geometry, which can be important for the physics of the flow (especially for envelope convection as seen here). The colour scale shows vorticity magnitude, with bright spots indicating the presence of strong vortices typically seen in 2D simulations of convection. Finally, Fig. 2.2c (Andrassy et al. 2020) shows the fractional volume of carbon-rich fluid for a 3D simulation of an oxygen burning shell with Cartesian geometry. Here the entrainment of carbon into the convective shell is highlighted.

All hydrodynamic simulations, no matter the setup, must use time steps small enough to resolve the convective motions when solving the fluid equations. This is a major limiting factor, since hydrodynamic time scales and stellar evolutionary time scales are vastly different. Depending on the exact setup, 3D simulations can only

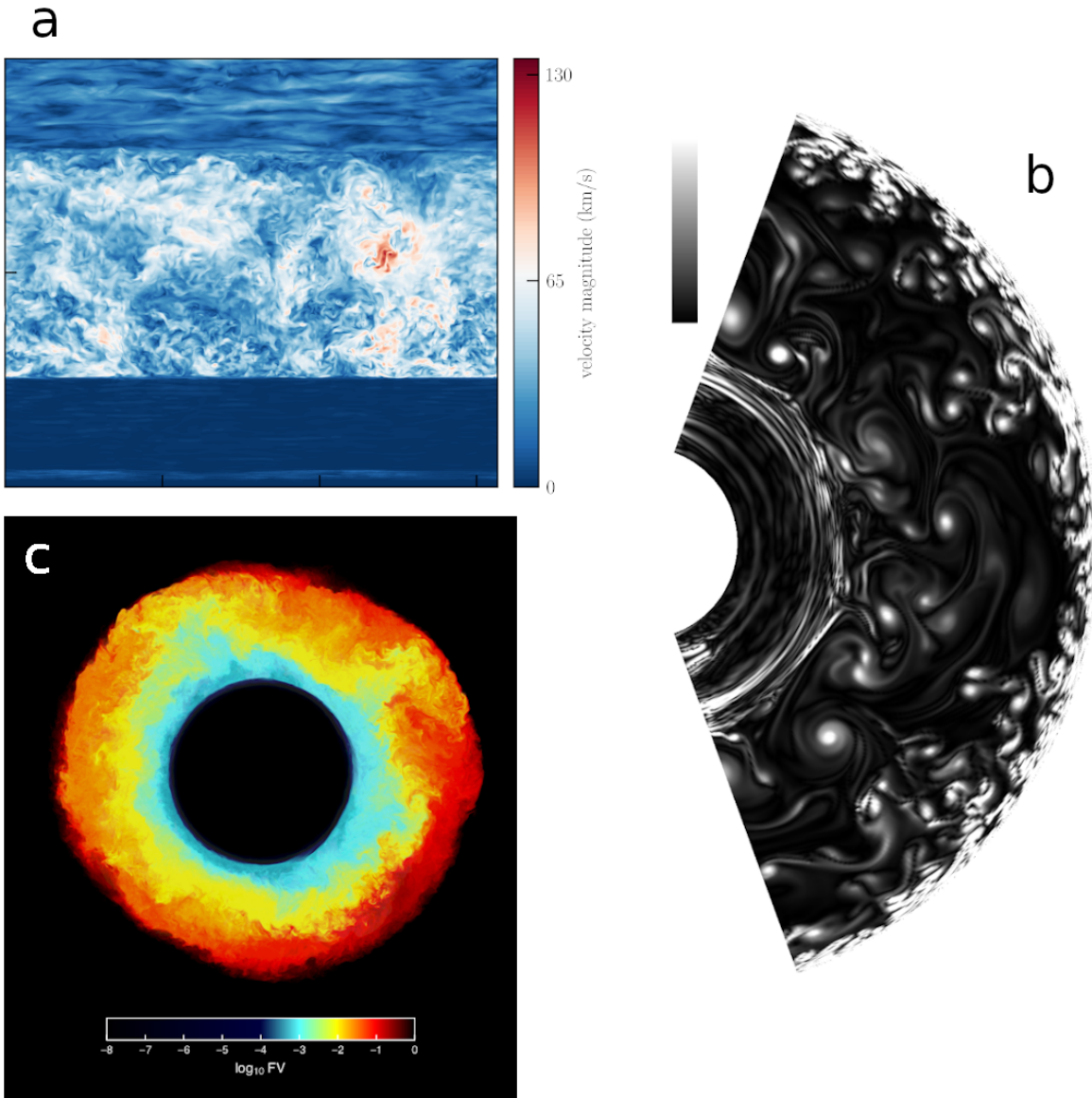


Figure 2.2: A selection of hydrodynamic simulation visualisations. **a.** Velocity magnitude in a 3D simulation of carbon shell burning by Cristini et al. (2017) (Fig. 1 Arnett et al. 2019). **b.** Vorticity magnitude in a 2D pre-main sequence star simulation (Fig. 3 Pratt et al. 2020). **c.** Fractional volume of carbon-rich fluid entraining into an oxygen-burning shell (Fig. 21 Andrassy et al. 2020).

typically simulate a short time scale (e. g. up to the order of 10^3 s of physical time for the carbon shell simulations of Cristini et al. (2019)), which can take months to compute on supercomputers, depending on the resolution. Reducing the computational cost may mean compromising on spatial resolution, which is important for studying narrow features such as convective boundaries. Simulating convection in 2D can mitigate some of these computational costs, with the caveat that the physics of the flow is affected by the geometry (e. g. the strong vortices in Fig. 2.2b; see Pratt et al. (2020) for a comparison of 2D and 3D simulations). However, the sheer difference in time scales between convection and stellar evolution mean that multi-dimensional models are limited to snapshots of the star’s life. From the modelling perspective, 1D models offer the best insight into global stellar evolution.

2.2.2 1D modelling using mixing length theory

In 1D models, the spherically-averaged stellar structure is computed in discrete time steps of the order of 10^3 to 10^4 yr for massive stars on the main sequence, and with only one spatial dimension (the radial direction), it is relatively computationally cheap to calculate stellar evolution. Much like the 2D and 3D simulations, a set of equations must be solved at each time step, but this time for the stellar structure rather than the fluid flow. Chapter 3 goes over these equations for the case of the Geneva stellar evolution code.

Convection must be significantly simplified in order to be modelled in 1D. In some cases, the mixing due to convection may be considered so fast compared to evolutionary time scales that it is effectively instantaneous. This approximation becomes less appropriate for the later stages of evolution, where evolutionary time scales become short enough to be comparable to the mixing time scales for convection. As an alternative, convection is often treated as a diffusive process, with diffusion coefficients governing the mixing speed for chemicals and angular momentum. In the case of convection, the

diffusion coefficient can be approximated as

$$D \approx \frac{1}{3}vl, \quad (2.9)$$

where v and l are the typical speed and mean free path respectively of fluid elements in the convection. Therefore, an estimate of these quantities is needed to calculate the mixing due to convection in 1D.

Apart from the strength of mixing, the temperature gradient in the convective region is also important, as it describes the efficiency of heat transport. Very efficient convection may be assumed to be adiabatic, and thus have a temperature gradient of

$$\nabla_{\text{ad}} = \frac{P\delta}{T\rho c_P}, \quad (2.10)$$

where $\delta = -(\partial \ln \rho / \partial \ln T)_P$. On the other hand, if the efficiency of convection is zero (as in non-convective regions), then the radiative temperature gradient is used:

$$\nabla_{\text{rad}} = \frac{3}{16\pi acG} \frac{\kappa L_r P}{M_r T^4}, \quad (2.11)$$

where G is the gravitational constant, L_r is the local luminosity and M_r is the mass contained within a shell with radius r . Whilst adiabatic convection dominates in the interior, superadiabatic convection is important in envelopes due to their low density, as described above in Sec. 2.1. The correct temperature gradient is needed for solving the equations of stellar structure (see Eq. 3.4 in Ch. 3), and is somewhere between ∇_{ad} and ∇_{rad} .

One method for calculating these needed quantities is the mixing length theory (MLT) of Böhm-Vitense (1958), which provides the theoretical framework for convection in many 1D stellar models¹. MLT allows the calculation of the velocities and temperature gradients necessary to describe the convection by making assumptions about the flow. One of the key assumptions is that the convection can be described as bubbles rising or falling a certain distance, l_m (the mixing length), before they dissipate into their surroundings.

¹In describing the quantities calculated in MLT, I will follow roughly the structure of Ch. 7, Kippenhahn & Weigert (1990)

In this picture of rising and falling bubbles, the velocity v is related to the difference in temperature gradient between the bubble and its surroundings as it travels a distance l_m . This is because the buoyant acceleration to which the bubble is subjected depends on its density compared to its surroundings, which is related to the temperature excess through the equation of state. As previously seen in Fig. 2.1, the bubble's temperature excess over its surroundings, ΔT , is determined by the temperature gradients, with ΔT being larger for adiabatic convection compared to superadiabatic convection. A convective energy flux, F_c , can be defined using this temperature excess:

$$F_c = \rho v c_P \Delta T, \quad (2.12)$$

with $v\Delta T$ properly representing a mean of all bubbles over a spherical shell. In convective regions, F_c represents a significant portion of the energy flux, but despite this, some energy is still transported by radiation (especially for low Pe). Therefore a radiative flux, F_r , is also needed and can be defined by

$$F_r = \frac{4acG T^4 M_r}{3 \kappa P r^2} \nabla, \quad (2.13)$$

where ∇ is the true temperature gradient in the convective region. The two quantities in Eqs. 2.12 and 2.13 summed give the total flux, where heat conduction is included in F_r by using an appropriate value² for κ . This total can be written in terms of ∇_{rad} as

$$F_c + F_r = \frac{4acG T^4 M_r}{3 \kappa P r^2} \nabla_{\text{rad}}. \quad (2.14)$$

To link the temperature gradients and the velocity, the kinetic energy of a bubble can be related to the work done on the bubble by buoyancy. The buoyant force per unit mass, $k = -g\Delta\rho/\rho$, is related to the gravitational acceleration g and the relative density difference between a bubble and its surroundings, $\Delta\rho/\rho$. However, since ΔT

²In degenerate conditions, heat conduction by electrons can be significant. This is accounted for in the opacity calculation, with $1/\kappa = 1/\kappa_{\text{rad}} + 1/\kappa_{\text{con}}$, where $1/\kappa_{\text{rad}}$ and $1/\kappa_{\text{con}}$ are the average radiative and conductive opacities respectively.

has already been used in Eq. 2.12, it is better to use the relative temperature excess

$$\begin{aligned}\frac{\Delta T}{T} &= \frac{1}{T} \frac{\partial \Delta T}{\partial r} \frac{l_m}{2} \\ &= \frac{\partial \ln \Delta T}{\partial P} \frac{\partial \ln P}{\partial r} \frac{l_m}{2} \\ &= (\nabla_e - \nabla) \frac{1}{P} \frac{\partial P}{\partial r} \frac{l_m}{2},\end{aligned}\tag{2.15}$$

where it is assumed that a typical bubble has moved a distance $l_m/2$. Using the definition of the pressure scale height $H_P = -P(dr/dP)$, Eq. 2.15 can then be written as

$$\frac{\Delta T}{T} = (\nabla - \nabla_e) \frac{l_m}{2H_P}.\tag{2.16}$$

This can then be related to the fractional density excess by $\Delta\rho/\rho = -\delta\Delta T/T$. The work done on the bubble is the buoyancy force multiplied by the distance travelled by the bubble ($l_m/2$), which is

$$k \frac{l_m}{2} = g\delta (\nabla - \nabla_e) \frac{l_m^2}{4H_P}.\tag{2.17}$$

Assuming that half of this work is converted into kinetic energy and the other half is used by the bubble to push through the fluid, then the velocity can then be given by

$$v^2 = g\delta (\nabla - \nabla_e) \frac{l_m^2}{8H_P}.\tag{2.18}$$

A last equation is needed to be able to solve for the quantities needed; this equation determines how close the temperature gradient of the bubble is to adiabatic. The departure of the bubble's temperature gradient from adiabatic is equal to the temperature change per unit distance due to heat loss, transformed into a dimensionless quantity:

$$\nabla_e - \nabla_{\text{ad}} = \frac{L_e H_P}{\rho V c_P v T},\tag{2.19}$$

where L_e is the luminosity of the bubble (in terms of heat loss) and V is its volume. L_e is given by

$$\begin{aligned}L_e &= \frac{8acT^3}{3\kappa\rho} \frac{S}{d} \Delta T \\ &= \frac{4acT^4}{3\kappa\rho} \frac{S}{d} (\nabla - \nabla_e) \frac{l_m}{H_P},\end{aligned}\tag{2.20}$$

where S and d are the surface area and diameter of the bubble respectively and Eq. 2.16 has been used for ΔT . Subbing Eq. 2.20 into Eq. 2.19 then gives

$$\begin{aligned}\nabla_e - \nabla_{\text{ad}} &= \frac{4acT^3}{3\kappa\rho^2c_Pv} \frac{Sl_m}{Vd} (\nabla - \nabla_e) \\ &= \frac{4acT^3}{3\kappa\rho^2c_Pv} \frac{9}{2l_m} (\nabla - \nabla_e),\end{aligned}\tag{2.21}$$

where the form factor Sl_m/Vd has been replaced by the typical value $9/2l_m$.

These equations are now all that is needed to solve for the velocity, temperature gradients and fluxes. Making use of the dimensionless quantities

$$U = \frac{3acT^3}{c_P\rho^2\kappa l_m^2} \sqrt{\frac{8H_P}{g\delta}};\tag{2.22a}$$

$$W = \nabla_{\text{rad}} - \nabla_{\text{ad}},\tag{2.22b}$$

then Eq. 2.21 and Eq. 2.18 give

$$\nabla_e - \nabla_{\text{ad}} = 2U \sqrt{\nabla - \nabla_e}.\tag{2.23}$$

Then, the flux equations Eq. 2.13, Eq. 2.12 (with Eq. 2.16 subbed in), and Eq. 2.14 give

$$(\nabla - \nabla_e)^{3/2} = \frac{8}{9} U (\nabla_{\text{rad}} - \nabla).\tag{2.24}$$

Finally, these two equations can be reduced into one cubic equation

$$(x - U)^3 + \frac{8U}{9} (x^2 - U^2 - W) = 0\tag{2.25}$$

where $x = \nabla - \nabla_{\text{ad}} + U^2$. This equation can be solved numerically in a stellar evolution code to give ∇ , which can then be used in Eqs. 2.18 and 2.24 to find the velocity.

The mixing length is calibrated to models, usually as a fraction of H_P , with the calibrated solar value for $l_m \sim 1.6$ used in the Geneva code (Ekström et al. 2012). There are disagreements with the solar oscillation frequencies using a constant fraction of H_P as the mixing length (Paterno et al. 1993; Gabriel 1995). In addition, although l_m stays $\sim H_P$, it is different for stars of different masses and temperatures (Stothers & Chin 1997; Ludwig, Freytag & Steffen 1999). MLT velocities are similar (within an

order of magnitude) to velocities seen in hydrodynamic simulations (e. g. Mocák et al. 2010, Cristini et al. 2017, Arnett et al. 2018).

Despite its usefulness for 1D stellar models, MLT has a number of limitations. The mixing length l_m is not known from theory and must be treated as a free parameter. It is treated both as the distance travelled by the bubble and the bubble’s size, which, for convective cores, l_m can be a significant fraction of the core size. In turbulent convection, whilst energy can be expected to be injected into the system at large scales (i. e into large bubbles), smaller eddies form a significant portion of the convection. The chemical abundances in the fluid are also assumed to be constant, which is not necessarily a good approximation for convection in the later stages of stellar evolution where convective time scales and nuclear burning time scales become similar. Another feature of convection, seen in hydrodynamic simulations but not accounted for in MLT, is that fluid does not simply move vertically; convection has a strong tendency towards horizontal flows near boundaries.

In addition, the classical MLT is a local theory, where convective velocities only depend on the local quantities. This presents a problem at the convective boundaries, where buoyant acceleration may be zero, but the speed of most convective elements will be non-zero. This creates the phenomenon of convective overshoot (see Sec. 2.3.2), which MLT does not describe. Some attempts have been made to use non-local variations of MLT to calculate the size of this overshoot region using a ballistic approach (Shaviv & Salpeter 1973; Maeder 1975; Langer 1986). However, as pointed out by Renzini (1987), these attempts suffer from having to use some local quantities, such as the convective flux, along with non-local equations for temperature excess and velocity.

A great deal of work has been done to extend or replace MLT (Unno 1961; Gough 1967; Stellingwerf 1976; Kuhfuss 1986; Canuto & Mazzitelli 1991; Deng, Xiong & Chan 2006). However, whilst some of these methods provide significant improvements (e. g. more accurate convective flux and no parameter needed for the mixing length in Canuto, Goldman & Mazzitelli 1996), none of them solved the major problem of a need for parameterised CBM in stellar evolution. Therefore, the simplicity of MLT and its ability to approximate the main features of convection needed for 1D modelling allows

it to remain a staple in stellar evolution codes.

2.3 Convective boundaries

Convective boundaries, as transition regions between turbulent and stable regions, contain complex physics such as shear, wave generation and CBM. As explained in the previous section, the MLT, which is commonly used in stellar evolution codes, does not describe the boundaries. Therefore other prescriptions must be used to locate convective boundaries and characterise their mixing.

2.3.1 Boundary location

As explained in Sec. 2.1, the temperature gradient of a perturbed fluid element, ∇_e , must be less than the temperature gradient of the background, ∇_s , in order for the region to be convectively unstable. Otherwise, the element oscillates around its equilibrium position. The frequency of this oscillation is given by the buoyancy frequency (also known as the Brunt-Väisälä frequency):

$$N^2 = \frac{g\delta}{H_P} \left(\nabla_{\text{ad}} - \nabla + \frac{\phi}{\delta} \nabla_{\mu} \right), \quad (2.26)$$

where $\phi = \partial \ln \rho / \partial \ln \mu$, $\nabla_{\mu} = d \ln \mu / d \ln P$ and μ is the mean molecular weight. It can be seen that this frequency is only real if the bracketed part on the right hand side is positive. If it is negative, then the fluid element will not oscillate but will instead accelerate away from its former equilibrium position, as in the case of convection.

Considering that $\nabla = \nabla_{\text{rad}}$ in stable regions, the Ledoux criterion for stability against convection (Ledoux 1947)

$$\nabla_{\text{rad}} < \nabla_{\text{ad}} + \frac{\phi}{\delta} \nabla_{\mu} \quad (2.27)$$

makes use of this fact. Thus, the Ledoux criterion gives a formal definition of a convective boundary when both sides of Eq. 2.27 are equal. The situation becomes simpler if the μ gradient is zero, in which case it reduces to the Schwarzschild criterion

(Schwarzschild 1958):

$$\nabla_{\text{rad}} < \nabla_{\text{ad}} \quad (2.28)$$

Parts of a star which are Schwarzschild unstable but Ledoux stable are said to undergo semiconvection. The assumed mixing speed of semiconvection determines whether it is appropriate to use the Ledoux or Schwarzschild criterion. If semiconvection is fast, then the Ledoux stable region will quickly become mixed, ∇_{μ} becomes zero, and the Schwarzschild criterion may be used. Otherwise, the Ledoux criterion is used along with a prescription which describes the mixing due to semiconvection beyond the Ledoux boundary. It is not currently known which of these is the more correct approach, although some differences do occur between Ledoux and Schwarzschild in particular phases, e. g. the convective shell which appears at the end of the main sequence (Kaiser et al. 2020).

Figure 2.3 shows an example of the temperature gradients in the interior of a stellar model with a convective core. The core at a fractional mass of $\lesssim 0.15$ is Schwarzschild unstable since $\nabla_{\text{rad}} > \nabla_{\text{ad}}$.

2.3.2 Convective boundary mixing

As explained in Sec. 2.2.2, the exact location of convective boundaries cannot be determined by any current theory of convection. Simply by virtue of inertia, any flows reaching the boundary of zero acceleration according to the Schwarzschild or Ledoux criterion will continue for some distance into the formally stable region. The mixing that occurs due to this phenomenon is called CBM. How far CBM extends, and to what degree it mixes the stellar interior, depends on the physics of the convection and the structure of the stable region.

Viallet et al. (2015) presented three regimes for CBM depending on the Péclet number and the range of length scales contributing to the CBM. As stated above in Sec. 2.1, the Péclet number, Pe , is the ratio of the advective time scale to diffusive time scale for heat transport and represents the importance of diffusion in the heat

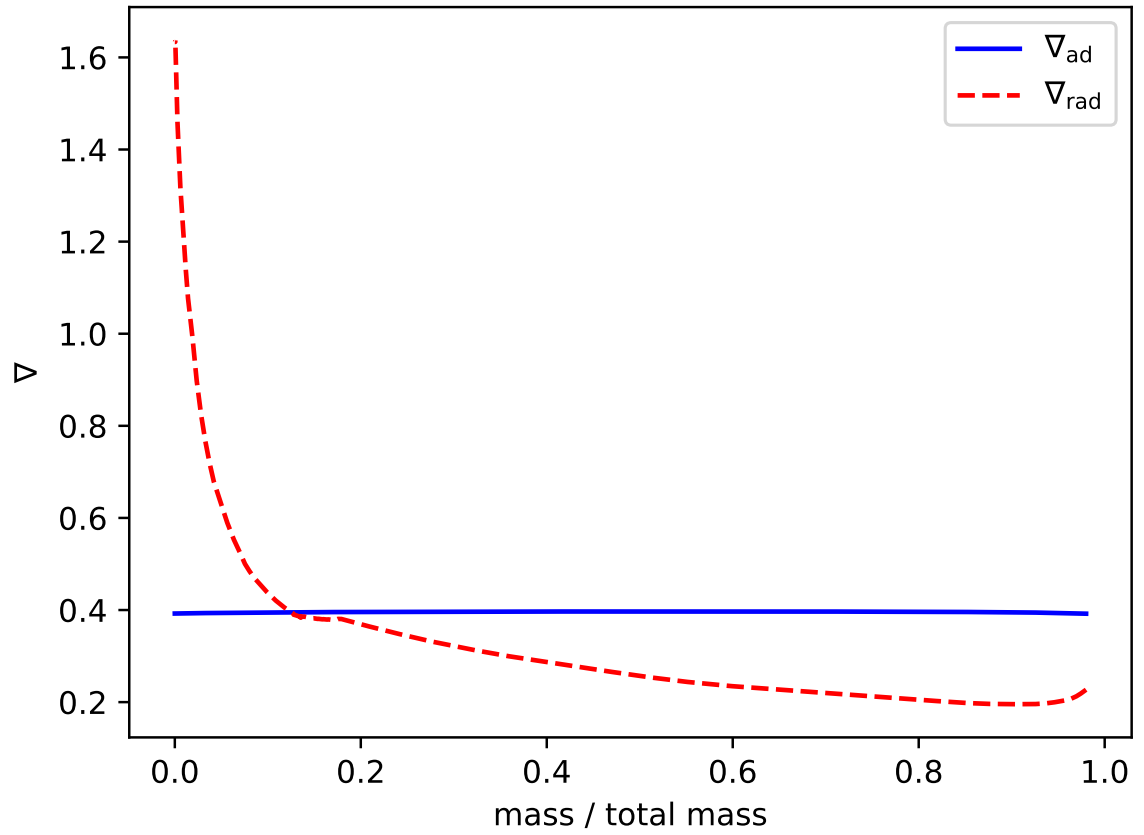


Figure 2.3: Temperature gradients in a star with a convective core. The radiative and adiabatic temperature gradients are labelled with the subscripts ‘rad’ and ‘ad’ respectively. The x -axis represents fractional mass, such that the centre of the star is on the left whereas the surface is on the right.

transport of the flow. This can be diffusion by radiation or by other processes such as electron conduction in degenerate conditions. According to Eq. 2.1, a critical length scale, l_d , can be defined as the value for the length scale l at which $Pe = 1$ for the CBM; by comparing this length scale to the largest and smallest length scales involved in the CBM, l_{\max} and l_{\min} , Viallet et al. (2015) defined three regimes for CBM:

1. $l_d > l_{\max}$ - diffusion regime;
2. $l_{\max} > l_d > l_{\min}$ - penetrative regime;
3. $l_{\min} > l_d$ - entrainment regime.

In regime 1., all the scales involved in the CBM, from l_{\min} to l_{\max} result in $Pe < 1$. Radiative diffusion of heat is therefore very important in this regime. If the critical length scale lies between l_{\min} and l_{\max} , the larger length scales in the CBM have $Pe > 1$ whilst the smaller have $Pe < 1$. CBM in regime 2. is therefore expected to have a transition between advection-dominant and diffusion-dominant mixing at some length scale. Lastly, regime 3. covers the case where all length scales involved in the CBM are larger than the critical length scale, and thus radiative diffusion is negligible and the CBM can be considered adiabatic.

Diffusive CBM can be expected to occur in shallow surface convection zones, e.g. in A-type stars, where the density drops to such a degree that radiative diffusion becomes more efficient and convection becomes significantly superadiabatic. As heat is rapidly transferred between fluid elements and their surroundings as the elements are moving, entropy is not mixed by this kind of CBM. However, chemical mixing by the fluid motion still occurs. This was the kind of CBM seen by Freytag, Ludwig & Steffen (1996) in their 2D simulations, which could be described by an exponential decay in velocity. This velocity can be related to diffusion (Eq. 2.9) and used in 1D codes, as done by Herwig (2000) and later incorporated into other codes such as MESA (Paxton et al. 2011).

This exponentially decaying diffusion is a widely used CBM prescription. The

diffusion coefficient in the CBM region is given by

$$D_{\text{CBM}} = D_0 \exp\left(\frac{-2z}{fH_P}\right), \quad (2.29)$$

where D_0 is a reference value of the diffusion coefficient within the convective region, z is the distance from the reference point, f is a parameter describing the strength of mixing and H_P is the pressure scale height.

The penetrative regime dominates at the bottom of deeper convective envelopes, where radiative diffusion is able to affect the temperature gradient in the CBM region. In these cases, cold plumes penetrate into the stable layer whilst gaining heat from the surroundings, leading to a subadiabatic temperature gradient in the CBM region. This heat transfer is slow enough that there is still significant entropy mixing in the CBM region. The subadiabatic temperature gradient in the CBM actually acts to allow plumes to penetrate deeper than they would have otherwise, since the buoyant braking on the plumes becomes less as their temperature gradient becomes more similar to that of their surroundings. The derived diffusion coefficient due to penetrating plumes is different to the diffusion dominated case, e. g. the Gumbel profile suggested by the 2D simulations of Pratt et al. (2017).

The penetrative regime has also been suggested to be appropriate for core convection on the main sequence by hydrodynamic simulation (e. g. Edelmann et al. 2019). At this point, core convection is less vigorous than at later stages due to the comparatively weak temperature dependence of hydrogen burning compared to heavier elements. Thus, the convective time scales are the longest of any burning phase and radiative effects have more time to act on convective elements. The default CBM prescription used in the Geneva code accounts for penetration by extending the adiabatic core by a fraction of a pressure scale height. However, the temperature gradient in the entire CBM region is approximated to be adiabatic, since the subadiabatic layer is relatively narrow (Zahn 1991).

The extension of the core by penetrative overshoot, also called step overshoot, is usually taken as the distance

$$d_{\text{ov}} = \alpha_{\text{ov}}H_P \quad (2.30)$$

where α_{ov} is a parameter which must be calibrated to observations. The mixing in this region is treated in the same way as the core. In the case of diffusive convection, there is no MLT velocity outside the formal convective region with which to calculate a diffusion coefficient, so the diffusion coefficient is taken to be the value just inside the convective region. The temperature gradient is assumed to be close to adiabatic in this case, since step overshoot models penetration of the stable region by convective elements. The step overshoot prescription is used by e.g. Schaller et al. (1992) and more recently Ekström et al. (2012), who use $\alpha_{ov} = 0.1$ following calibration to the MS width.

In the regime where $Pe \gg 1$ for all scales involved in the CBM, turbulent entrainment is dominant. This occurs primarily in the advanced phases of evolution, particularly when neutrino cooling is significant and evolutionary time scales are short. Due to the high Pe , the temperature gradient in the CBM layer (the entrained region) is very close to adiabatic. As seen in many hydrodynamic simulations of convection (e.g. Woodward, Herwig & Lin 2015; Müller et al. 2016; Stephens et al. 2021), turbulent entrainment occurs when material from the stable region is transported across the boundary by instabilities induced by shear. The convective region gradually grows into the stable region as more fluid is incorporated. The progression of the boundary due to entrainment can be described using the entrainment law (Fernando 1991)

$$\frac{v_e}{v} = ARi_B^{-n}, \quad (2.31)$$

where v_e is the boundary progression speed, v is the typical speed of convective flows, A and n are parameters, and Ri_B is the bulk Richardson number. Ri_B is a dimensionless number quantifying how well the boundary resists the destabilising effects of the adjacent convective flows. It can be written as

$$Ri_B = \frac{l\Delta b}{v^2}, \quad (2.32)$$

where l is a typical length scale for the eddies contributing to the entrainment and Δb is the buoyancy jump, an integral over the buoyancy frequency N^2 . The numerator of Eq. 2.32 represents something like the potential energy stored by the boundary when

perturbed by the size of a typical eddy, whereas the denominator represents the kinetic energy of the convection. Typical values for Ri_B vary; Cristini et al. (2017) gives values between 10^2 and 10^4 for different boundaries up to the point of oxygen burning in a $15 M_\odot$ star.

CBM prescriptions replicating turbulent entrainment are not widely used in stellar evolution codes, although Staritsin (2013) calculated massive star models on the main sequence using the entrainment law approach. His work will be compared to the new Geneva code entrainment prescription in Ch. 4 and Ch. 6.

As well as mixing through bulk motion of fluid, convective boundaries also excite instabilities which contribute to mixing. One of these instabilities is shear, the most familiar form of which in stars is due to differential rotation, for example in the solar tachocline. In this case, instability due to differences in rotational velocity at different radii in a star can lead to significant mixing (Maeder & Meynet 2000). In the case of a convective boundary, shear instabilities may develop even in a non-rotating or very slowly-rotating star (Arnett et al. 2015). In this case, the shear instability arises due to the motion of convective elements. In a real star (as opposed to 1D models), convection is not simply an up-down motion where elements come to a stop at the convective boundary before falling back into the convective region again. Instead, the deceleration of convective elements near the edge of the boundary (past the formally convective boundary) acts to turn the flow in a horizontal direction before it then returns into the convective region. The contrast in horizontal velocity between the eddies at the boundary and the stable region is what leads to shear instability.

Another form of instability excited by the boundary is wave production. The convective boundary surface undulates due to the turbulent motion beside it. This, along with events such as plume penetration, excites waves known as internal gravity waves (IGW) which propagate through the stable layer (Rogers & McElwaine 2017; Edelmann et al. 2019; Horst et al. 2020). IGW can contribute to mixing well into the stable region, although their mixing is slower than most other CBM. They have also been suggested as contributing to the transport of angular momentum (Rogers et al. 2013; Aerts, Mathis & Rogers 2019). Their mixing is usually modelled using a diffusion

coefficient (e.g. Herwig et al. 2007; Battino et al. 2016).

3 The Geneva stellar evolution code

The models presented in this work have been calculated using the Geneva stellar evolution code (**GENEC**), described in Eggenberger et al. (2008). As part of this thesis work, the code has been extended to include entrainment and convective shear as additional CBM prescriptions. The first part of this chapter is a brief overview of **GENEC**, with particular focus on convection and CBM. The second part describes each of the features added to **GENEC** to facilitate these new CBM prescriptions.

3.1 Overview of **GENEC**

Like other stellar evolution codes¹, **GENEC** calculates the structure of a model star at discrete time steps. The initial values needed to compute a model using **GENEC** are the mass and metallicity, which allow a first estimate of the stellar structure. A target rotation rate for the zero age main sequence may also be given. From there, the differential equations of stellar structure are solved to calculate the new structure at each time step. The following equations describe the non-rotating case, valid for the models presented in later chapters of this thesis. Further details on the derivation of these equations can be found in Kippenhahn & Weigert (1990). The first equation describes mass conservation, and can be written as

$$\frac{\partial r}{\partial M_r} = \frac{1}{4\pi r^2 \rho}, \quad (3.1)$$

where r is the radius, M_r is the mass contained with the radius r and ρ is the density.

The next is momentum conservation:

$$\frac{\partial P}{\partial M_r} = -\frac{GM_r}{4\pi r^4} - \frac{1}{4\pi r^2} \frac{\partial^2 r}{\partial t^2}, \quad (3.2)$$

¹There numerous stellar evolution codes, often specialising in different physical processes or stellar mass ranges, since many research groups write their own codes in-house. Here is a non-exhaustive list: **CLES** (Scuflaire et al. 2008), **FRANEC** (Degl’Innocenti et al. 2008), **KEPLER** (Weaver, Zimmerman & Woosley 1978), the Lyon code (Chabrier & Baraffe 1997), **MESA** (Paxton et al. 2011), **STAREVOL** (Forestini, Arnould & Paulus 1991), **STERN** (Langer et al. 1988) and **TYCHO** (Young & Arnett 2005).

where P is pressure, G the gravitational constant and t time. In the case of hydrostatic equilibrium, the second term on the right hand side can be ignored. The next equation describes energy conservation and is written as

$$\frac{\partial L_r}{\partial M_r} = \epsilon_{\text{nuc}} - \epsilon_\nu - c_P \frac{\partial T}{\partial t} + \frac{\delta}{\rho} \frac{\partial P}{\partial t}, \quad (3.3)$$

where L_r is the luminosity produced within the radius r , ϵ_{nuc} is the nuclear energy generation rate, $-\epsilon_\nu$ is the rate of energy loss due to neutrinos, c_P is the specific heat capacity at constant pressure, T is the temperature and δ is the partial derivative $-(\partial \ln \rho / \partial \ln T)_{P,\mu}$. The equation of energy transport is written as

$$\frac{\partial T}{\partial M_r} = -\frac{GM_r T}{4\pi r^4 P} \nabla, \quad (3.4)$$

where ∇ is the temperature gradient $\partial \ln T / \partial \ln P$. In **GENEC**, $\nabla = \nabla_{\text{ad}}$ in convective regions and $\nabla = \nabla_{\text{rad}}$ in stable regions (also known as radiative regions). Finally, there are a set of equations which relate to the changes in chemical species due to nuclear reactions. The change in amount of a chemical species i , given in terms of the mass fraction X_i , can be described by the following:

$$\frac{\partial X_i}{\partial t} = \frac{m_i}{\rho} \left(\sum_j R_{ji} - \sum_k R_{ik} \right), i = 1, \dots, I \quad (3.5)$$

where m_i is the mass of the element i , R_{ji} is the reaction rate for a reaction converting species j to species i and R_{ik} is the reaction rate for converting species i to species k . Thus the sum over R_{ji} represents the sum of all sources of the element i and the sum over R_{ik} is the sum over all its sinks. There are a set of I equations of this form, one for each isotope tracked by the code. An additional constraint on the set of equations is that the mass fractions must sum to unity.

In the case of rotating models, the shellular rotation scheme of Zahn (1992) is used. To allow the non-spherically-symmetric case of a rotating star to be modelled with a 1D code, the shellular rotation scheme assumes that strong turbulence along isobars produces a constant angular velocity on those isobars. The adjustments to the differential equations of stellar structure as used in **GENEC** are given in Eggenberger et al. (2008), with more details in Meynet & Maeder (1997).

The equation of state used by **GENEC** includes radiation pressure and partial degeneracy. As well as determining the relation between P , T and ρ , it also calculates thermodynamic quantities such as ∇_{ad} and the various derivatives (e. g. Eq.3.10) which are important for modelling convection.

For the solution of Eqs. 3.1 to 3.4, **GENEC** uses the Henyey method. In this method the derivatives are converted into difference equations, where the differences occur between discrete mass shells. If the differential equations are written as

$$\frac{dy_i}{dM_r} = f_i(y_1, \dots, y_4), \quad (3.6)$$

where y_i are each of four variables r, P, L_r and T , and f_i is a function of those variables, then a discretised function at each shell j can be defined:

$$A_i^j = \frac{y_i^j - y_i^{j+1}}{M_r^j - M_r^{j+1}} - f_i(y_1^{j+1/2}, \dots, y_4^{j+1/2}), \quad (3.7)$$

where $j + 1/2$ represents a value intermediate between shells. The difference equation for the mass interval M_r^j to M_r^{j+1} is then $A_i^j = 0$. Such equations exist for all the grid points in the model. An approximate guess at the variables y_i gives $A_i^j \neq 0$; this first value of A_i^j can then be used with Eq. 3.7 to calculate the corrections needed for each variable. This process is iterated until the values of the corrections are under certain tolerance, at which point the stellar structure is considered solved.

3.2 Convection in GENEC

As part of the solution of the stellar structure, the temperature gradient must be known in order to solve Eq. 3.4. The presence of convectively unstable regions strongly influences the temperature gradient, so the extent of these regions must be found before the final stellar structure is modelled. As discussed in Ch. 2, this can be done using the Schwarzschild criterion for convective instability,

$$\nabla_{\text{rad}} > \nabla_{\text{ad}}, \quad (3.8)$$

or the Ledoux criterion,

$$\nabla_{\text{rad}} > \nabla_{\text{ad}} + \frac{\phi}{\delta} \nabla_{\mu}, \quad (3.9)$$

where ∇_{rad} and ∇_{ad} are the radiative and adiabatic temperature gradients respectively and the other quantities are given by

$$\phi = \left(\frac{\partial \ln \rho}{\partial \ln \mu} \right)_{T, \mu}; \delta = - \left(\frac{\partial \ln \rho}{\partial \ln T} \right)_{P, \mu}; \nabla_{\mu} = \left(\frac{d \ln \mu}{d \ln P} \right)_{P, T}. \quad (3.10)$$

For ϕ , the simplification $\phi = 1$ is made, which is true for an ideal gas with radiation pressure equation of state. However, the Schwarzschild criterion is the default method in **GENEC**, which only requires the radiative and adiabatic temperature gradients. See Kaiser et al. (2020) for a discussion on the effects on stellar evolution of using either the Schwarzschild or the Ledoux criterion.

Once the convective regions in the star are determined, the appropriate temperature gradient must be applied to solve Eq. 3.4. **GENEC** assumes the radiative temperature gradient in all stable regions. In convectively unstable regions, the adiabatic temperature gradient is assumed for the interior and MLT is used to calculate a temperature gradient for the envelope.

In **GENEC**, there are two schemes of convective mixing: instantaneous and diffusive. In both cases, the locations of convectively unstable regions are determined first, according to the Schwarzschild or Ledoux criteria. Instantaneous mixing is used prior to core oxygen burning and is completely decoupled from nuclear burning. This means that the adjustment of chemical abundances according to Eq. 3.5 is calculated before any diffusion.

The diffusion of chemical abundances is calculated according to

$$\left(\frac{dX_i}{dt} \right)_{\text{diff}} = \left(\frac{\partial}{\partial M_r} \right)_t \left[(4\pi r^2 \rho)^2 D \frac{\partial X_i}{\partial M_r t} \right] \quad (3.11)$$

where D is the total diffusion coefficient. If the model includes rotation, then D includes contributions from convection, meridional circulation, dynamical shear and optionally magnetic fields. Otherwise, only convection contributes to the diffusion coefficient, in which case $D = D_{\text{conv}}$. D_{conv} is only non-zero in convective regions unless shear CBM is turned on; see Sec. 3.3.2 in this chapter.

The convective diffusion coefficient is calculated using the MLT velocity. To prevent numerical difficulties, an upper limit, D_{\max} , is imposed using the size of the convective region ΔR_{conv} and the time step Δt :

$$D_{\max} = \frac{10\Delta R_{\text{conv}}^2}{\Delta t}. \quad (3.12)$$

If $D_{\text{conv}} = D_{\max}$, then the convective region could be considered very well mixed and using a higher value of D_{conv} would have negligible consequences. Typically, $D_{\text{conv}} = D_{\max}$ for interior convective regions whilst the envelope retains the MLT value, since ΔR_{conv} can become very large for convective envelopes.

3.3 New convective boundary mixing prescriptions

3.3.1 Changes related to entrainment

Entrainment is a major new feature which I added to **GENEC** as part of this thesis work. As described in Chapter 2, the entrainment of material from a stable region into a convectively unstable region can be described by the entrainment law:

$$\frac{v_e}{v_c} = ARi_B^{-n}, \quad (3.13)$$

where v_e is the progression speed of the entrainment boundary, v_c is the typical speed for convective flows, Ri_B is the bulk Richardson number and A and n are parameters. The unknown to be found from this equation is v_e ; all other quantities can either be calculated from the stellar structure with some assumptions (v_c , Ri_B) or given appropriate values upon running the model (A , n).

The typical convective speed v_c is calculated using a mass-weighted root mean square of the mixing length theory (MLT) velocity, v_{MLT} , in the Schwarzschild convective region:

$$v_c = \sqrt{\frac{\sum_i v_{\text{MLT},i}^2 \Delta m_i}{\sum_i \Delta m_i}}, \quad (3.14)$$

where i represents the model mesh point and Δm is the mass contained between the midpoints of shells $i + 1$ and i , and $i - 1$ and i .

The bulk Richardson number is defined as

$$Ri_B = \frac{l_c \Delta b}{v_c^2}, \quad (3.15)$$

where l_c is a length-scale for turbulent motions in the convective region, v_c is the typical speed of convective flows (as in Eq. 3.14) and Δb is the buoyancy jump. l_c is defined as a number of pressure scale heights (of order 1 pressure scale height). The boundary pressure scale height $H_{P,b}$ is taken at $r = r_b$, where r_b is the radius of the convective core. If there is no instantaneous CBM included in the model, r_b is equivalent to the Schwarzschild boundary. Otherwise, it is the radius to which the CBM extends. The buoyancy jump is an integral of the squared buoyancy frequency N^2 with respect to radius r , given by

$$\Delta b = \int_{r_1}^{r_2} N^2 dr, \quad (3.16)$$

where r_1 and r_2 encompass the boundary of the convective core, centred at $r = r_b$. Fig. 3.1 shows how the N^2 integration limits are placed around the boundary in the calculation of Δb .

The distance of r_1 and r_2 from r_b can be controlled by the variable $f_{\Delta b}$, which is by default set to $f_{\Delta b} = 0.25$. Thus, $r_1 = r_b - f_{\Delta b} H_P$ and $r_2 = r_b + f_{\Delta b} H_P$. If the radius of r_1 is less than the radius of the Schwarzschild boundary, then r_1 is instead positioned at the Schwarzschild boundary. This prevents negative N^2 regions, which do not contribute to buoyancy braking, from being included in the buoyancy jump integration. The equation for the buoyancy frequency is

$$N^2 = \frac{g\delta}{H_P} (\nabla_{\text{ad}} - \nabla + \frac{1}{\delta} \nabla_{\mu}), \quad (3.17)$$

where g is the gravitational acceleration, H_P the pressure scale height, δ the density gradient with respect to temperature ($-\frac{\partial \ln \rho}{\partial \ln T}$), ∇_{ad} the adiabatic temperature gradient, ∇ the actual temperature gradient, and ∇_{μ} the mean molecular weight gradient.

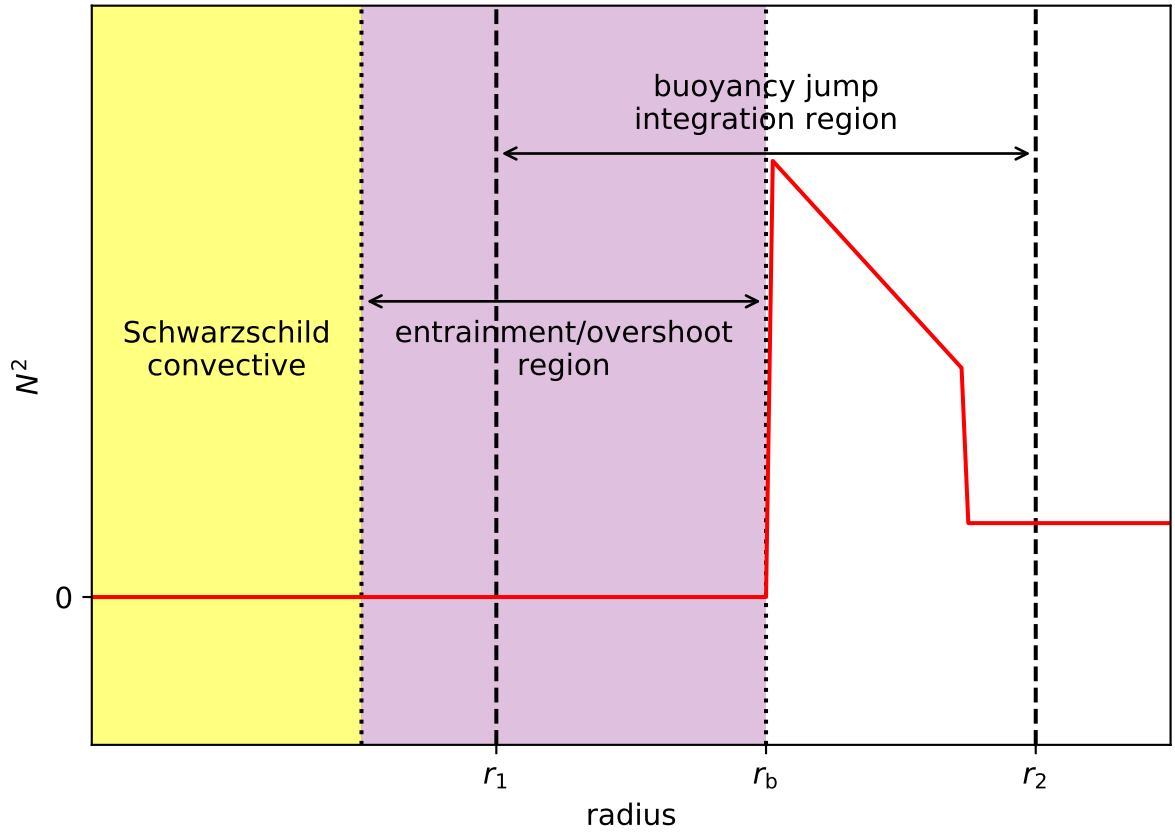


Figure 3.1: A schematic representation of the buoyancy jump integration region on the upper boundary of an interior convective region. The value of the buoyancy frequency N^2 is approximated to 0 in the Schwarzschild convective (yellow shaded) and overshoot/entrained region (purple shaded), since here the temperature gradient is assumed to be adiabatic. The region over which N^2 is integrated to calculate the buoyancy jump is bounded by r_1 and r_2 . Note that the only contribution to the buoyancy jump comes from the region between r_2 and the upper edge of the CBM region, marked by r_b ; this would no longer be true if the temperature gradient in the entrained region were non-adiabatic.

3.3.2 Changes related to convective shear

The next CBM prescription which I have implemented in `GENEC` is exponentially decaying diffusion. However, its use in the interiors of stars, whilst supported by e.g. Moravveji et al. (2016), must represent a different form of mixing than the outer layer mixing seen in Freytag, Ludwig & Steffen (1996), from which this prescription was derived and implemented into 1D codes (Herwig 2000). As suggested by Arnett et al. (2015) and Battino et al. (2016), a shear layer at the edge of the convective region may produce partial mixing, which is consistent with this prescription. I therefore refer to the exponential decay of mixing at the boundary as convective shear.

The equation controlling the exponential decay of the diffusion coefficient is written as

$$D_{\text{CBM}} = D_0 \exp\left(\frac{-2z}{fH_P}\right), \quad (3.18)$$

where D_{CBM} is the diffusion coefficient due to convective boundary mixing, D_0 is the original value of the diffusion coefficient in the convective region, z is the distance away from the boundary, f is the parameter controlling the slope of the decay and H_P is the pressure scale height. This equation follows the results of Freytag, Ludwig & Steffen (1996) based on 2D simulations of convection. In `GENEC`, the exponential decay begins a distance fH_P inside the convective region and continues until the diffusion coefficient drops to a value of 100 cm s^{-2} . Below this value (also used by the `MESA` stellar evolution code) the amount of mixing by diffusion would be negligible and so can be ignored.

Since the shear can occur on multiple convective regions in a star, the exponentially decaying diffusion coefficient can encounter another region of exponential decay related to another convective region. In this case, the final value of the diffusion coefficient is taken to be the sum of the diffusion coefficient from each convective boundary.

In addition to the original exponential decay formulation in Eq. 3.18 (known as single- f), there is also the double- f shear mixing, where the slope of the exponential decay changes some way away from the convective boundary. This is supposed to simulate the effect of mixing due to gravity waves produced at the convective boundary. In the double- f scheme, the value of the f parameter increases from $f = f_1$ to a higher

value $f = f_2$ once the exponential decay decreases to a certain value D_2 . In the study of Battino et al. (2016), this value for D_2 is $10^5 \text{ cm}^2 \text{ s}^{-1}$ for interior convective regions and $10^{11} \text{ cm}^2 \text{ s}^{-1}$ for the envelope. This is based on the work of Denissenkov & Tout (2003) and Battino et al. (2016).

Thus, the equation for D_{CBM} in the case of double- f shear CBM becomes

$$D_{\text{CBM}} = D_{\text{ref}} \exp\left(\frac{-2z_{\text{ref}}}{fH_P}\right), \quad (3.19)$$

where $D_{\text{ref}} = D_0$, $f = f_1$ and z_{ref} is the distance to the convective boundary if $D_{\text{CBM}} > D_2$, otherwise $D_{\text{ref}} = D_2$, $f = f_2$ and z_{ref} is the distance to the point at which $D_{\text{CBM}} = D_2$. Figure 3.2 shows how the diffusion coefficient behaves for both single- and double- f CBM.

The code in `GENEC` has also been altered to allow the values of f to be controlled separately for the envelope and the interior. The shear mixing can also be applied in addition to overshoot or entrainment, in which case the extent of overshoot/entrainment will replace the convective boundary for determining the extent of shear mixing.

3.4 Resolution

Spatial resolution in the Geneva code is set by parameters controlling the allowed change in variables between model grid points. The controlled variables include pressure, luminosity, and the chemical species ^4He , ^{16}O , and ^{20}Ne . If a variable q is controlled by the resolution parameter `dgrq`, an extra grid point is added between points i and $i + 1$ when the following condition is met:

$$|q_i - q_{i+1}| > \text{dgrq}. \quad (3.20)$$

This results in the addition of grid points where the variable q changes quickly. The code also removes grid points where variables change slowly. In this case, the condition

$$|q_i - q_{i+1}| < \text{dklq} \quad (3.21)$$

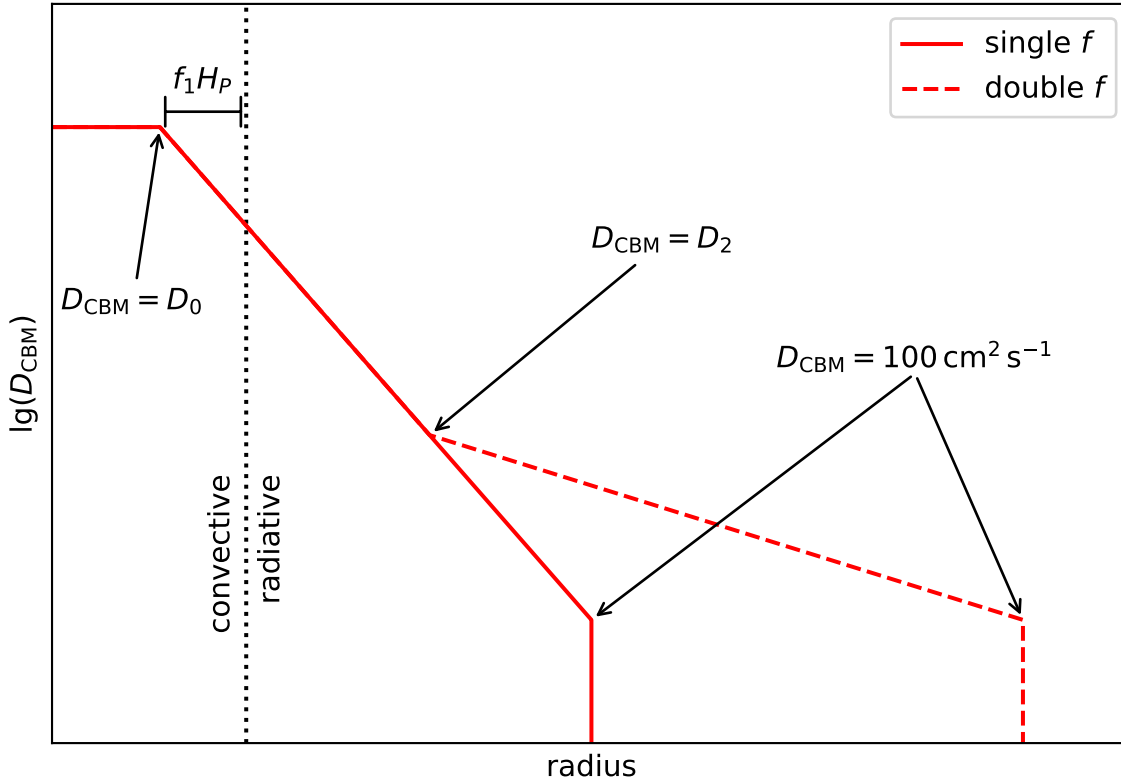


Figure 3.2: A schematic representation of convective shear CBM in GENEC on the upper boundary of an interior convective region. The formal convective boundary given by the Schwarzschild or Ledoux criterion is shown with a dotted line; the exponential decay in both cases begins a distance $f_1 H_P$ inside this boundary. Since the logarithm of the diffusion coefficient D_{CBM} is plotted against radius, the exponential decay given by Eqs. 3.18 and 3.19 appears linear. The single- and double- f prescriptions only differ when D_{CBM} decays to the value D_2 , at which point the double- f prescription switches from $f = f_1$ to the higher value of $f = f_2$. In both cases the diffusion coefficient is cut off at a minimum value of $D_{\text{CBM}} = 100 \text{ cm}^2 \text{ s}^{-1}$.

must be met for all variables q tracked in the resolution module, where $\mathbf{dklq} < \mathbf{dgrq}$.

In resolution studies performed as part of the work in Ch.4, the convergence of the MS lifetime with adjustment of the resolution parameters was used to judge good resolution. MS lifetime was chosen due to its relationship with MS width in the Hertzsprung-Russell diagram and its sensitivity to core size. The ${}^4\text{He}$ abundance was therefore identified as the most important variable for spatial resolution, having the greatest impact on number of grid points in the region of interest (the core boundary) compared to the other controlled variables. Other resolution parameters had little effect on MS lifetime.

Based on the lifetimes of the step overshoot models shown with filled circles in Figure 3.3, a resolution parameter value of $\mathbf{dgry} = 0.003$ was taken as appropriate for these models. Fig. 3.3 shows how MS lifetime varies for a $15 M_{\odot}$ model when changing $\mathbf{dgry} = 0.003$ by a factor λ_s (note that these MS lifetimes were calculated using models with $\lambda_t = 3$; see Fig 3.4). A similar set of lifetimes for the entrainment models is shown in Fig. 3.3 with open circles for comparison. Table 3.1 gives the mean number of grid points in the models presented in Fig. 3.3.

The use of integrals of the buoyancy jump in the calculation of Ri_B require particularly fine resolution at the convective boundary to ensure that Ri_B remains as stable as possible. Otherwise, Ri_B can increase sharply over a single time step before dropping again. Whilst this seems to be a transient effect that does not impact the MS lifetime, it can make analysis of the behaviour of Ri_B difficult. Therefore, included in the entrainment prescription is a new resolution condition for the addition of grid points:

$$|\ln r_i - \ln r_{i+1}| > \mathbf{dgrra}, \quad (3.22)$$

which is active within a small mass region centred on the furthest extent of CBM. The size of this region is 1% of the total mass of the star, which is both large enough to accommodate changes in the position of the boundary as the model converges and small enough to not impact MS lifetime. A value of $\mathbf{dgrra} = 0.0003$ generally produces the best-behaved Ri_B .

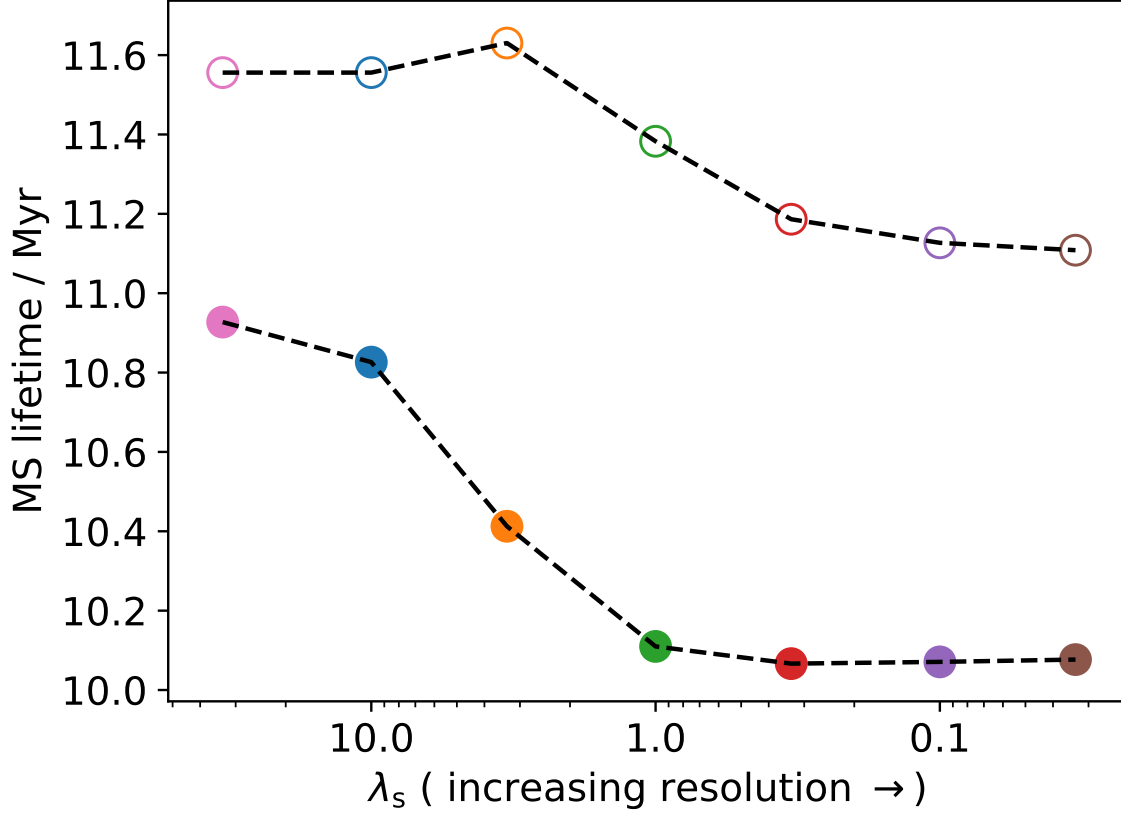


Figure 3.3: MS lifetime of $15 M_{\odot}$ models with varying spatial resolution. The filled circles represent step overshoot models with $\alpha_{ov} = 0.1$ whereas the open circles represent entrainment models with $A = 10^{-4}$ and $n = 1$.

Table 3.1: Mean number of grid points over the main sequence for the step overshoot and entrainment models presented in Fig. 3.3.

λ_s	number of grid points	
	step overshoot	entrainment
100/3	199	273
10	206	273
10/3	231	272
1	380	384
1/3	577	874
1/10	797	831
1/30	715	883

Table 3.2: Total number of time steps over the main sequence for the step overshoot and entrainment models presented in Fig. 3.4.

λ_t	number of time steps	
	step overshoot	entrainment
9	1292	881
3	3581	3855
1	10246	10913
1/3	30302	36155
1/9	91154	90261

Models including shear have a slightly different form of the spatial resolution parameter which uses the value of the diffusion coefficient, D , to determine whether a good resolution. A grid point is added between points i and $i + 1$ if

$$\frac{D_i - D_{i+1}}{\min(D_i, D_{i+1})} > \text{dgrd} \quad (3.23)$$

provided that both values of D are above the floor value of 10^{-10} . The grid points in profiles of models including shear are shown in Ch. 5 (e. g. Fig. 5.10).

The time step in **GENEC** is controlled using the energy generation rate in the centre. It is generally set so that the MS is split in several thousand time steps. Fig. 3.4 shows the effect on MS lifetime of changing time step length by a factor λ_t in a spatially resolved ($\lambda_s = 1$) $15 M_\odot$ model. The total number of time steps for each of these models is given in Table 3.2. As with the spatial resolution, the main sequence lifetimes of the step overshoot models shown in Fig. 3.4 can be used to judge good resolution. The entrainment model lifetimes shown for comparison display a similar behaviour to the step overshoot models.

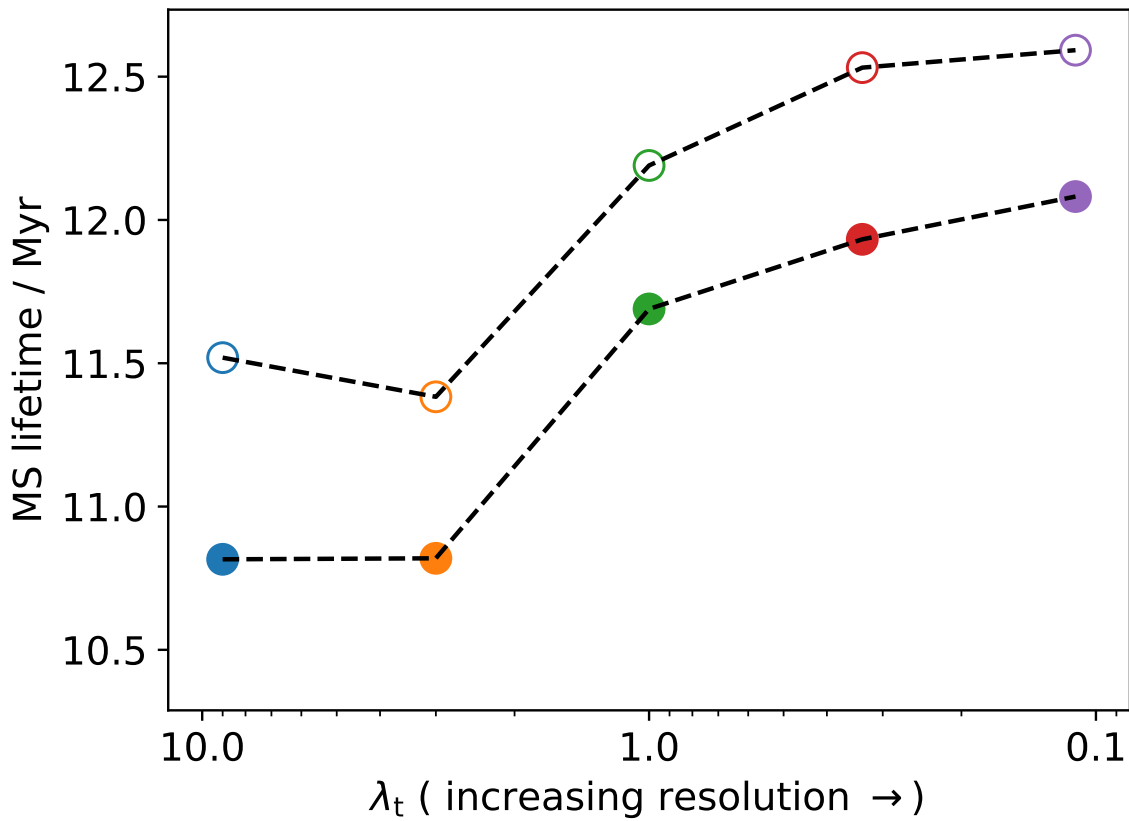


Figure 3.4: MS lifetime of $15 M_{\odot}$ models with varying temporal resolution. The filled circles represent step overshoot models with $\alpha_{\text{ov}} = 0.1$ whereas the open circles represent entrainment models with $A = 10^{-4}$ and $n = 1$.

4 Models with entrainment

In this chapter I will describe a grid of models with entrainment CBM and analyse the differences between these models and models with standard overshoot. The results contained in this chapter have been published in Scott et al. (2021).

It has long been known that convective boundary mixing must be included into stellar models in order to reproduce observations. The MS width of clusters is one of the best-known examples of such observations; other examples include large samples of wide binaries and asteroseismic measurements (e.g. Claret & Torres 2019, Deheuvels et al. 2016). As a result, stellar models' CBM schemes are calibrated to give results consistent with the observed reality. Castro et al. (2014) showed that current generations of models have MS widths on the HRD which are too narrow for high mass stars. The discrepancy in width grows larger with mass.

Currently, CBM is usually implemented in 1D stellar evolution codes in one of two ways. The first of these is step overshoot, which is an extension of the convective core by some fraction of a pressure scale height (see e.g. Ekström et al. 2012). Depending on the code, mixing in the overshoot region could be instantaneous or diffusive. The second is exponentially decaying diffusion, where mixing is governed by a diffusion coefficient which decays exponentially from a value near the Schwarzschild boundary (Freytag, Ludwig & Steffen 1996; Herwig 2000). The parameters in both can be calibrated in order to match observations such as post-MS spin down (Fig. 1 in Brott et al. 2011) and asteroseismic frequencies (Aerts et al. 2018).

Both 3D hydrodynamics simulations and observations can be compared to 1D models incorporating CBM and other mixing processes, such as waves (Meakin & Arnett 2007; Jones et al. 2017; Edelmann et al. 2019; Müller 2020; Pratt et al. 2020). Incorporating 3D hydrodynamics results, such as convective regions which grow as a result of entrainment, into 1D models also allows them to be studied on evolutionary timescales. It has been shown that the rate of entrainment of material at convective borders is dependent on the bulk Richardson number, Ri_B , a dimensionless measure

of the penetrability of a boundary by convection. For example, Cristini et al. (2019) showed that both the upper and lower boundaries in a convective shell followed the same entrainment law, suggesting that CBM is controlled by the global properties of the convective region. Despite these results from simulation, the entrainment law is not widely used in 1D stellar evolution codes.

Prior to this study, only Staritsin (2013) has published 1D entrainment law stellar models. Staritsin’s models of 16 and 24 M_{\odot} main sequence stars with entrainment were calibrated using asteroseismology values for the extent of mixing. In these models, the extent of extra mixing beyond the formally convective region (in units of pressure scale heights) decreased as the models evolved. This contrasts traditional CBM which typically stays constant.

4.1 Methods

4.1.1 Entrainment law algorithm

We use the entrainment law as described in Sec. 3.3.1 to calculate an entrainment rate. The quantity l_c used in the calculation of Ri_B represents the length-scale of the largest fluid elements in the turbulent region. We use $l_c = 0.5H_{P,b}$, motivated by the results of Meakin & Arnett (2007), who found that the horizontal correlation length-scale for velocity in their simulation of convection was approximately half a pressure scale height. We aim to be consistent with Cristini et al. (2019) by using this estimate of the horizontal correlation length-scale as a proxy for l_c .

In this study we use $r_2 = r_b + 0.25H_{P,b}$ for the calculation of Δb to be consistent with previous work (Cristini et al. 2019). Conversely, r_1 is the larger of either $r_b - 0.25H_{P,b}$ or the Schwarzschild boundary. The total size of the integration region encompassed by r_1 and r_2 is therefore between 0.25 and $0.5H_{P,b}$, depending on the size of the entrainment region. This is supposed to encompass the part of the boundary in which fluid elements are decelerated and turned back towards the convective region by

buoyancy. Cristini et al. (2019) Table 2 gives examples of their simulation boundary widths, which are all a fraction (0.1 to 0.6) of a pressure scale height. We cannot use a boundary width of $\sim 2v_c/N$ as in Staritsin (2013), since at our boundary we have $N = 0$, so we use the approach of Cristini et al. (2019). However, we cannot be sure if the boundary width does not vary with mass (other than what is already contained in the mass dependence of $H_{P,b}$), and the integration region size must still be considered a free parameter. The buoyancy jump and its dependence on these parameters is discussed in more detail in Section 4.2.1 and Fig. 4.2.

Note that if $n = 1$ (as is the case for most of our models), any uncertainty in l_c in Eq. 3.15 would inversely scale A . However, we are not targeting exact values for these parameters, and we can be fairly certain given the results of Meakin & Arnett (2007) that $l_c \sim H_{P,b}$ as we have assumed.

A mass entrainment rate, \dot{M}_{ent} , can be derived from Eq. 3.13 to give

$$\dot{M}_{\text{ent}} = 4\pi r_b^2 \rho_b v_c A Ri_B^{-n}, \quad (4.1)$$

with ρ_b being the density at $r = r_b$. The mass contained within the entrained region, M_{ent} , is then

$$M_{\text{ent}} = \sum_j \dot{M}_{\text{ent},j} \Delta t_j \quad (4.2)$$

where j denotes the model time step with length Δt . This region is then considered part of the convective core. This means that the region is then instantaneously mixed and the temperature gradient is set to ∇_{ad} (further discussed in Section 6.1).

In our implementation of the entrainment law, the entrained mass accumulates over the lifetime of the core with each time step, according to Eq. 4.2. Since the value of Ri_B controls $\dot{M}_{\text{ent},j}$ rather than M_{ent} directly, any previous history of entrainment in the models is unaffected by the instantaneous value of Ri_B . This contrasts the previous implementation of Staritsin (2013), in which the entrained distance at any time step is equal to $v_e \Delta t$. Thus, our prescription can be viewed as cumulative entrainment and Staritsin's as instantaneous (meaning that it depends only on the stellar structure at the current time step). 3D hydrodynamic simulations of stellar convection which exhibit

entrainment show that the convective region continuously accumulates material. This is the motivation for a cumulative entrainment method, as once material is entrained, it stays well-mixed. However, it is not known whether this holds true on evolutionary time-scales so it is not clear at this point which approach is more appropriate. Our method allows us to investigate the consequences of cumulative entrainment which is controlled by the changing value of the bulk Richardson number and we compare our results to Staritsin (2013) in Section 6.1.

4.1.2 Geneva code model grid

We use the Geneva stellar evolution code, **GENEC** (Eggenberger et al. 2008), to compute a grid of non-rotating MS models with solar metallicity ($Z = 0.014$). The masses included are 1.5, 2.5, 8, 15, 25, 32, 40 and $60 M_{\odot}$. For each mass we compute at least one standard CBM model and one entrainment model.

The standard CBM prescription in **GENEC** is step overshoot, where the convective core is extended by some distance $\alpha_{\text{ov}} H_{P,b}$. In **GENEC**, the default value for α_{ov} is 0.1 for models with initial mass $M_{\text{ini}} \geq 1.7 M_{\odot}$, 0.05 for $1.7 M_{\odot} > M_{\text{ini}} \geq 1.25 M_{\odot}$ and 0 for $M_{\text{ini}} < 1.25 M_{\odot}$. These default values were calibrated using the MS width of low mass stars (for details see Ekström et al. 2012). As in the core, the CBM (a.k.a. overshoot) region is mixed instantaneously (for both chemical species and entropy) and uses the adiabatic temperature gradient.

Table 4.1 lists the models computed and their key properties. The first four columns of Table 4.1 define the initial parameters of the model. These are the initial mass M_{ini} and the CBM parameters (either α_{ov} for step overshoot models or a combination of A and n for entrainment models). The τ_{MS} column is the main sequence lifetime. This is defined as the age of the model when the central hydrogen mass fraction has reached 10^{-4} . The next column, $T_{\text{eff,min}}$, is the minimum effective temperature reached by the model during the MS. Next is the mean of the bulk Richardson number, $\langle Ri_B \rangle$, taken over the duration of τ_{MS} , along with the means of its components, $\langle v_c \rangle$ and $\langle l_c \Delta b \rangle$. The final three columns pertain to the model attributes at the end of the

MS. These include the final mass, M_{fin} , the mass of the helium core, M_{He} , and the total mass entrained, $M_{\text{ent,tot}}$. M_{He} is defined as the mass of the convective core at a central hydrogen mass fraction of one per cent.

Both a default step overshoot model and an entrainment model with $A = 10^{-4}$ and $n = 1$ were calculated for each mass. This value of A was chosen to reproduce the MS lifetime of the $2.5 M_{\odot}$ standard overshoot model, as this mass is within the mass range originally used to calibrate the step overshoot. $A = 2 \times 10^{-4}$ was also used for some masses to explore the widening of the MS in the high-mass range.

Previous simulations of convection have found that $n \sim 1$, which guided our choice to keep $n = 1$ for the majority of our grid. However, the A values used for our 1D MS models ($A \sim 10^{-4}$) are substantially lower than those derived from 3D simulations. A values derived from 3D simulations include $A = 1.06$ (oxygen burning, Meakin & Arnett 2007), $A \approx 0.1$ (oxygen burning, Müller et al. 2016) and $A = 0.05$ (carbon burning, Cristini et al. 2019). The difference could simply be a matter of evolutionary phase, since these 3D simulations are all of later stages than the MS. One potential confounding factor is radiative diffusion. Since the burning stages from carbon onward are neutrino-cooled, the effect of radiative diffusion on the mixing process is minimal, in contrast to the MS. Another point is partial degeneracy, which plays a part in later-stage stellar evolution but not in MS convective cores. Finally, the entrainment law may not keep the same slope for all Ri_{B} values. Our 1D models have Ri_{B} in the range of $\sim 10^4$ to $\sim 10^7$, which is substantially higher than the upper limit of $Ri_{\text{B}} \sim 1000$ in the 3D simulations and may represent a different entrainment law regime. Alternatively, there may be other important physics which is not encompassed by the entrainment law in its current form.

Table 4.1: Summary of the CBM parameters used in the grid along with some key quantities. See Sec. 4.1.2 for a description of the columns.

M_{ini} [M_{\odot}]	α_{ov}	A	n	τ_{MS} [Myr]	$\lg(T_{\text{eff,min}})$ [K]	$\lg(Ri_{\text{B}})$	$\lg\langle v_c \rangle$ [cm s^{-1}]	$\lg(l_c \Delta b)$ [$\text{cm}^2 \text{s}^{-2}$]	M_{fin} [M_{\odot}]	M_{He} [M_{\odot}]	$M_{\text{ent,tot}}$ [M_{\odot}]
1.5	0.05	-	-	2093	3.82	7.54	3.29	14.2	1.50	0.0662	-
1.5	-	10^{-4}	1	2060	3.82	7.60	3.29	14.2	1.50	0.0723	0.0135
2.5	0.1	-	-	512	3.93	6.84	3.66	14.2	2.50	0.173	-
2.5	-	5×10^{-5}	1	486	3.94	6.87	3.66	14.2	2.50	0.181	0.0395
2.5	-	10^{-4}	1	519	3.92	6.86	3.66	14.2	2.50	0.227	0.0869
2.5	-	2×10^{-4}	1	582	3.90	6.86	3.67	14.2	2.50	0.319	0.199
2.5	-	3×10^{-4}	1	668	3.87	6.89	3.68	14.3	2.50	0.457	0.368
8	0.1	-	-	31.8	4.27	5.76	4.22	14.2	8.00	0.933	-
8	-	10^{-4}	1	33.1	4.26	5.80	4.23	14.3	8.00	1.25	0.403
8	-	2×10^{-4}	1	36.5	4.24	5.82	4.23	14.3	8.00	1.69	0.833
15	0.1	-	-	11.6	4.39	5.29	4.46	14.2	14.8	2.82	-
15	0.3	-	-	13.0	4.35	5.27	4.47	14.2	14.7	3.69	-
15	0.5	-	-	14.3	4.31	5.24	4.47	14.2	14.7	4.55	-
15	-	10^{-4}	1	12.3	4.37	5.34	4.47	14.3	14.8	3.72	0.960
15	-	2×10^{-4}	1	13.8	4.34	5.38	4.47	14.3	14.7	5.01	2.06
15	-	10^{-4}	0.9	15.1	4.27	5.49	4.48	14.5	14.6	6.24	3.24
15	-	10^{-4}	1.2	10.9	4.40	5.40	4.46	14.3	14.8	2.52	0.0881
15	-	10^{-4}	1.5	10.9	4.40	5.28	4.46	14.2	14.8	2.39	0.00350
25	0.1	-	-	6.54	4.43	5.00	4.62	14.2	24.2	6.64	-
25	0.3	-	-	7.14	4.37	4.97	4.62	14.2	23.8	8.14	-
25	0.5	-	-	7.70	4.25	4.95	4.63	14.2	23.0	9.54	-
25	0.7	-	-	8.18	3.96	4.94	4.63	14.2	20.4	10.8	-
25	-	10^{-4}	1	6.99	4.39	5.08	4.62	14.3	24.1	8.73	1.90
25	-	2×10^{-4}	1	7.63	4.31	5.11	4.63	14.4	23.3	10.9	3.72
32	0.1	-	-	5.30	4.43	4.85	4.68	14.2	30.1	9.55	-
32	0.3	-	-	5.72	4.32	4.82	4.69	14.2	28.9	11.4	-
32	0.5	-	-	6.09	3.78	4.80	4.69	14.2	24.9	13.1	-
32	-	10^{-4}	1	5.66	4.33	4.92	4.69	14.3	29.1	12.4	2.49
32	-	2×10^{-4}	1	6.08	4.00	4.94	4.69	14.3	25.3	15.4	4.87
40	0.1	-	-	4.51	4.40	4.71	4.73	14.2	36.5	13.0	-
40	0.3	-	-	4.84	3.88	4.69	4.74	14.2	30.0	15.2	-
40	0.5	-	-	5.11	3.83	4.67	4.74	14.1	24.6	17.1	-
40	-	10^{-4}	1	4.86	3.63	4.78	4.74	14.3	29.5	17.1	3.35
60	0.1	-	-	3.58	4.08	4.63	4.74	14.1	36.6	21.2	-
60	0.3	-	-	3.79	4.23	4.59	4.75	14.1	36.4	24.8	-
60	0.5	-	-	3.95	4.28	4.57	4.75	14.1	37.8	28.0	-
60	-	10^{-4}	1	3.75	4.10	4.66	4.75	14.2	34.6	26.2	3.51

4.2 Results

4.2.1 Time dependence of boundary penetrability and mass entrainment rate

The time dependence of the bulk Richardson number, Ri_B , for two $15 M_\odot$ models (step overshoot with $\alpha_{ov} = 0.1$, entrainment with $A = 10^{-4}$ and $n = 1$) is presented in Fig. 4.1. Over the MS, the variations in Ri_B are modest, within one order of magnitude. Nevertheless, we can see in Fig. 4.1 that Ri_B initially increases and later on decreases.

The increase in Ri_B can be understood by considering the evolution of the buoyancy jump Δb (the length-scale for turbulent motions, l_c , which is set to half of a pressure scale height, is roughly constant during the MS), which is an integration of the buoyancy frequency N^2 over the boundary region. In a massive star such as the $15 M_\odot$ model plotted, the convective core continuously recedes in mass over the MS. As the convective core recedes, it leaves behind a chemical gradient which contributes to an increase in N^2 and hence Δb . This leads to an increase in $l_c \Delta b$ (the numerator in Ri_B shown in the second row of Fig. 4.1), which is strongest at the very beginning of the main sequence since there is no chemical composition gradient to start with. After some time (age ~ 6.5 Myr), the core recedes far enough that the outermost limit of the buoyancy jump integration is lower than the original extent of the convective core. From this point onward, Δb remains roughly constant since the full extent of its integration region is already occupied by the chemical gradient left by the convective core. Note that this saturation would likely occur earlier in the evolution if the size of the integration region was smaller. The transient spikes in Ri_B also come from spikes in Δb . These originate from the finite differencing used in the code, since the boundary lies between two grid points. Fortunately, they have no impact on the results since they cause a temporary decrease in the entrainment mass rate (bottom row in Fig. 4.1). The spikes can be further explained by considering the integration of the squared buoyancy frequency. The buoyancy frequency depends on the gradient of the mean molecular weight, ∇_μ (see Eq. 3.17), which becomes the dominant part of N^2

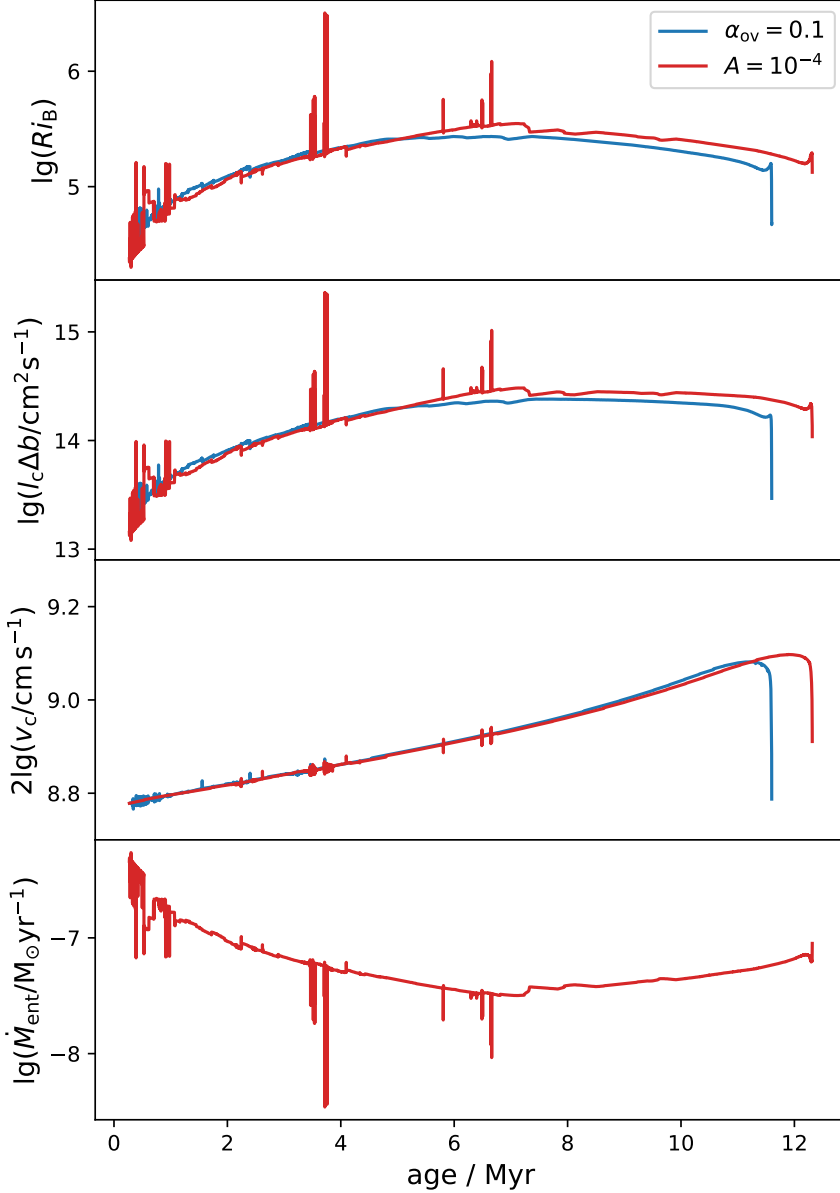


Figure 4.1: Time evolution of the bulk Richardson number for $15 M_{\odot}$ models with either the default step overshoot parameter $\alpha_{ov} = 0.1$ or entrainment parameters $A = 10^{-4}$ and $n = 1$. From top to bottom, the figure presents the bulk Richardson number, Ri_B , the buoyancy jump multiplied by the length-scale for turbulent motions, $l_c \Delta b$ (the numerator of Ri_B), the mass-weighted mean square of the MLT velocity, v_c , throughout the convective region (the denominator of Ri_B) and finally the corresponding mass entrainment rate, \dot{M}_{ent} (using Eq. 4.1).

at the upper edge of the CBM region. In the absence of mixing above this edge, ∇_μ can experience large local spikes. This is reflected in the mean molecular weight μ as step-like features rather than a smooth profile, and can cause transient increases in Ri_B . These perturbations in Ri_B do not cause pathological changes in the core mass, which evolves smoothly (see Fig. 4.4).

We intentionally did not include any shear mixing beyond the entrained region to study the effects of entrainment without any additional extension the MS lifetime from other factors. Any additional mixing processes such as shear would make it difficult to determine how much the entrainment itself affects the MS width and lifetime. However, we know from 3D simulations that there is a shear layer, which will smooth composition and structure profiles and probably prevent these spikes in the models (Arnett & Moravveji 2017; Jones et al. 2017). This shear layer could be modelled using an exponentially decaying diffusion coefficient (exp-D hereinafter, Freytag, Ludwig & Steffen 1996, Herwig 2000) at the edge of the entrained region. Preliminary results suggest that a combination of entrainment and exp-D improves the transient spikes in Ri_B seen in pure entrainment models. Since exp-D provides an extra source of CBM, smaller values of A might be needed in these combination models to produce the required MS widths.

Figure 4.2 shows the buoyancy jump integration region at three stages of the evolution of the $15 M_\odot$ entrainment model with $A = 2 \times 10^{-4}$. The dashed lines represent the position of the edge of the entrained region at $r = r_b$. The dotted lines represent the upper and lower limits of the integration. Both N^2 (*blue*) and Δb (*green*) are plotted, with Δb being the value obtained when integrating from the convective boundary to the corresponding radius on the x-axis. Hence, the value for Δb at $(r - r_b)/H_{P,b} = 0.25$ is the value plotted in Fig. 4.1. Values for Δb at higher radius would be obtained if the upper limit of the integration was larger.

Since the temperature gradient in the entrained region is adiabatic, N^2 is only positive in the stable region, which is the only region to contribute to the buoyancy jump in our current models. Fig. 4.2 also shows that the main contribution to the buoyancy jump is from the region close to $r = r_b$. Outside our chosen integration

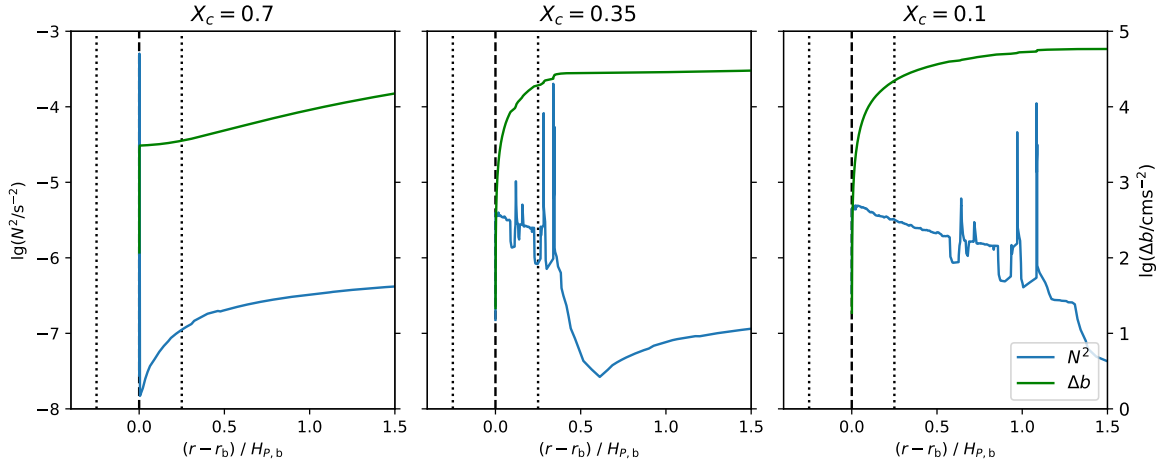


Figure 4.2: Profiles of the buoyancy frequency N^2 (blue) at three different central hydrogen mass fractions, X_c (indicated at the top of the panel), in a $15 M_\odot$ entrainment model with $A = 10^{-4}$ and $n = 1$. Also shown is the buoyancy jump Δb (green, right axis) when integrated out to the corresponding number of pressure scale heights from the boundary, shown on the x-axis. The dashed line at $(r - r_b)/H_{P,b} = 0$ is the border between the entrained region and the stable region at $r = r_b$. The dotted lines represent the limits of the buoyancy jump integration as used in our models ($r_b \pm 0.25H_{P,b}$).

region, Δb remains at a similar order of magnitude. If the integration region is in fact significantly smaller than our chosen value, e.g. $0.05H_P$, then the buoyancy jump would also be significantly smaller.

Finally, the modest decrease in Ri_B towards the end of the MS is due to the gradual increase in convective velocities (third row in Fig. 4.1). The increase in convective velocities is due to the luminosity of the star gradually increasing over the MS. Since velocity and luminosity are related by $v_c^3 \propto L$ (Biermann 1932)¹, convective velocities also increase over the MS. Compared to Δb , however, the variation in v_c is small, which explains why Δb has the greatest effect on the overall changes of Ri_B during the MS.

¹This can be understood in terms of the Kolmogorov cascade (Eq. 2.5), in which the rate of energy dissipation by turbulence is proportional to v^3 . The luminosity, being the source of the energy which then cascades down to the smallest scales, is equal in magnitude to (though out of phase with) the energy dissipation.

Over the MS, Ri_B varies between a few tens of thousands and a few hundreds of thousands (excluding short spikes explained above). Using the entrainment law (Eq. 3.13) with $A = 10^{-4}$ and $n = 1$, this leads to mass entrainment rates between $10^{-6.3}$ and $10^{-7.5} M_\odot \text{yr}^{-1}$ in a $15 M_\odot$ model. The mass entrainment rate, which is inversely proportional to Ri_B , first decreases during the first part of the MS and later on increases slightly. The mass entrainment rate in this model leads to a total entrained mass of $0.960 M_\odot$ (see last column of Table 4.1).

4.2.2 Mass dependence of boundary penetrability

Current observations seem to suggest that convective boundary mixing is mass dependent. For instance, Claret & Torres (2019) presented the dependence of CBM as a function of mass for stars of less than $\sim 4 M_\odot$ in binary systems, finding a steep dependence for the lowest mass stars with growing convective cores on the MS. Schootemeijer et al. (2019) found a mild dependence of CBM on mass for stars in the Small Magellanic Cloud. Higgins & Vink (2019) compared models to the massive star binary HD 166734, concluding that a step overshoot parameter of $\alpha_{\text{ov}} = 0.5$ was suitable for stars above 30 to $40 M_\odot$, which is much larger than the value of $\alpha_{\text{ov}} = 0.1$ determined for lower mass stars by Ekström et al. (2012). Castro et al. (2014) performed a large study on Milky Way stars and found significant broadening of the MS at higher masses; we compare to this work in particular in Sec. 4.2.4. In this section, we explore if this dependence can be explained by the mass dependence of stellar structure and properties.

It is well known that the luminosity has a strong mass dependence. For low-mass stars, the dependence is steep with $L \propto M^3$. For massive stars, it flattens and approaches a linear dependence with mass above about $20 M_\odot$ (see Fig. 6 in Yusof et al. 2013). A higher luminosity leads to higher convective velocities ($v_c^3 \propto L$, Biermann 1932). Since the bulk Richardson number, Ri_B , contains a velocity term, it would also be expected to show mass dependence.

The left panel of Figure 4.3 shows the logarithm of the time average of two values: Ri_B and v_c^2 (sign reversed, since it is the denominator of Ri , and scaled by a constant

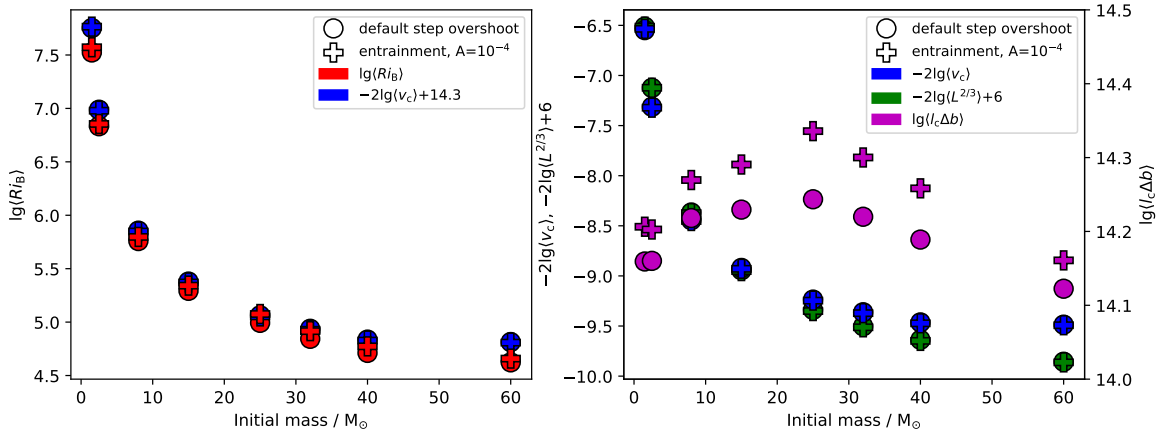


Figure 4.3: Mass dependence of the Bulk Richardson number and its components. The left hand panel shows the time-average of the \log_{10} of the bulk Richardson number over the MS against initial mass. Circles represent default step overshoot models ($\alpha_{\text{ov}} = 0.05$ for $1.5 M_\odot$, $\alpha_{\text{ov}} = 0.1$ otherwise) and pluses represent entrainment models with $A = 10^{-4}$ and $n = 1$. The right panel shows the \log_{10} of the time average of the two components of Ri_B . For the denominator (v_c^2), a minus sign is used so that adding the values of the two components yields the value of Ri_B .

value to fit on the same axis). This panel demonstrates that Ri_B is mass dependent and its dependence is dominated by the velocity term. The right panel shows the velocity term compared to total luminosity (again scaled by a constant), demonstrating that the mass dependence of velocity is also very similar to that of luminosity, as expected from the mass luminosity relation. Conversely, the buoyancy jump term also plotted in the right-hand panel does not demonstrate mass dependence since its logarithm varies by less than 0.5 dex. Despite this, the buoyancy jump term does dominate the variation of mass entrainment rate with time (Fig. 4.1) and so cannot be ignored when considering entrainment at the convective boundary. Note also that this only holds if our assumptions on the buoyancy jump integration region (see Sec. 4.1.1) are correct.

In this section, we showed that convective boundary properties have a clear mass dependence, which can be measured via Ri_B . Next, we want to explore whether the entrainment law, which uses Ri_B can provide the mass dependence of the convective

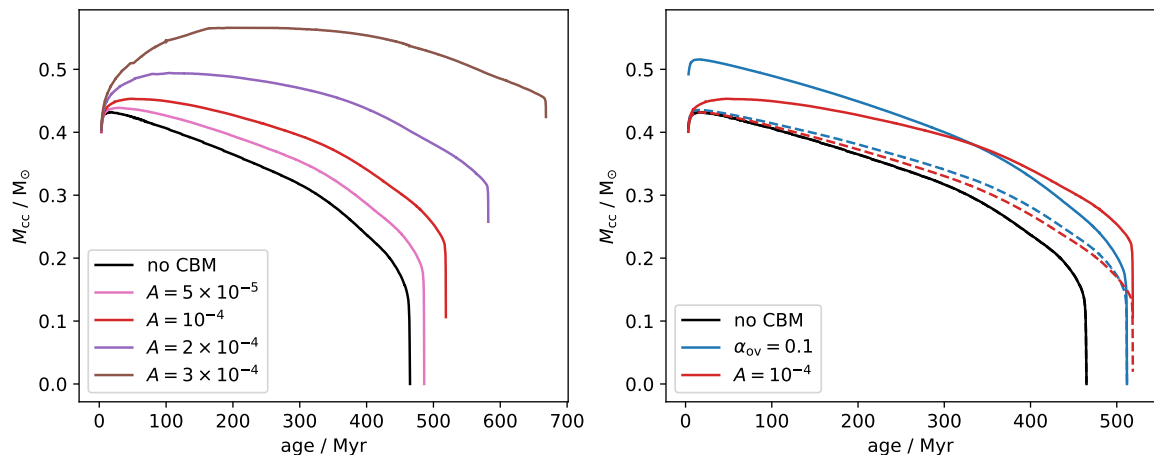


Figure 4.4: Comparison of the evolution of the convective core mass (Schwarzschild convective region plus CBM region), M_{cc} , for $2.5 M_{\odot}$ models with step overshoot $\alpha_{ov} = 0.1$ and entrainment. Entrainment models use $n = 1$. *Left*: Time evolution of M_{cc} for various values of A , including $A = 0$ (no CBM). *Right*: The step overshoot model compared to the entrainment model with the closest-matching lifetime ($A = 10^{-4}$) and the model without CBM. The dashed lines show the mass coordinate of the Schwarzschild boundary. The entire convective region and CBM region (for both overshooting and entrainment) are assumed to be fully mixed (for both chemical species and entropy) and have an adiabatic temperature gradient.

boundary mixing needed to reproduce the observed MS width. We can already note that Ri_B decreasing with initial mass will lead to higher entrainment rates for more massive stars, which goes in the right direction.

4.2.3 Dependence of entrainment on the entrainment law parameters

Both 3D simulations and theoretical studies determined various values for the entrainment law parameters A and n . From a theoretical energy balance argument, n should be 1 (Stevens & Lenschow 2001). This arises from assuming that the only source of the turbulent kinetic energy which drives entrainment is the conversion of potential energy by buoyancy, as in Stage & Businger (1981). Under this assumption, the turbulent ki-

netic energy is then dissipated by entrainment overturning fluid layers. It is the kinetic energy present in the boundary region (due to dissipation being non-instantaneous) which leads to its movement at a speed v_e . Taking $n = 1$ therefore represents the idealised situation where the kinetic energy at the boundary yet to be dissipated by entrainment is proportional to the ratio of convective kinetic energy to the potential energy stored in the boundary (the inverse of Ri_B). Hydrodynamical simulation values for n range from ~ 0.7 to ~ 1 depending on the setup. Conversely, literature values for A vary from $A \approx 1$ (Meakin & Arnett 2007) to $A \approx 0.05$ (Cristini et al. 2019). See Müller (2020) and references therein for examples of entrainment law parameters derived from 3D simulation results. The fact that A and n are not the same between setups suggests that the entrainment law in its current form does not encompass every aspect of the growth of the convective region in these simulations.

In this study, we start by taking $n = 1$ and use published 1D **GENEC** evolution models with step overshoot and $\alpha_{ov} = 0.1$ to determine a value of A that would reproduce the published models. The value of $\alpha_{ov} = 0.1$ in **GENEC** models is constrained using the main sequence width for low/intermediate-mass stars (Ekström et al. 2012). The same value of α_{ov} is then applied to all higher masses (at all metallicities) in the published grids of **GENEC** models. Therefore, $2.5 M_\odot$ models were used to constrain an A value in entrainment models that matches the general properties of the $2.5 M_\odot$ **GENEC** model with step overshoot and $\alpha_{ov} = 0.1$: MS width in the HRD, core masses and MS lifetime. Table 4.1 and Fig. 4.4 show the comparison between entrainment models with different values of A and the default overshoot model. They confirm that the minimum effective temperatures reached by the models with $\alpha_{ov} = 0.1$ and $A = 10^{-4}$, $n = 1$ are very similar. Table 4.1 also indicates that the MS lifetimes are similar.

Figure 4.4 shows the evolution of the convective core mass in $2.5 M_\odot$ entrainment models. The left-hand panel shows how the entrainment depends on the value of A with values of A ranging from zero (no CBM) to 3×10^{-4} (all models with $n = 1$). As expected, a larger value of A leads to more entrainment and thus larger convective core masses and longer lifetimes. One point to note is that since entrainment rate is reduced if Ri_B increases, the potential problem of the convective region quickly encompassing

the whole star can be avoided. Indeed, as the entrainment extends further, the jump in composition and entropy at the boundary increases and makes the boundary stiffer, which makes it harder for additional entrainment. The use of the entrainment law thus provides an important feedback. This is best seen for the $A = 3 \times 10^{-4}$ model (brown curve), where entrainment leads to core growth only during the first part of the MS. After a while, the entrained mass plateaus since the entrainment rate drops significantly and the convective regions shrinks in mass due to the Schwarzschild boundary receding as in the step overshoot models. Note that much larger values of A may still lead to the entire model becoming convective. Much larger values of A are not needed or supported by observations anyway as discussed in Sec. 4.2.4.

Keeping $n = 1$, the value $A = 10^{-4}$ provides the closest match to the default step overshoot model in terms of MS lifetime. We see, however, that the time evolution of the convective core is very different in entrainment models compared to the step overshoot model, as shown in the right-hand panel of Fig. 4.4. The step overshoot model assumes that mixing is an instantaneous process (compared to the MS lifetime) and thus the convective core is significantly larger on the zero age main sequence (ZAMS) in these models. On the other hand, entrainment is a time-dependent process (in that the size of the entrained region is dependent on the earlier entrainment history) and builds up over the entire MS, as shown in Eq. 4.2. The dashed-red line indicates the Schwarzschild boundary in the $A = 10^{-4}$ model and shows how the entrained region (region between the solid and dashed red lines) grows in mass with time. This means that for a given lifetime, the entrainment models start with smaller and end with larger convective core masses compared to step overshoot models (see Table 4.1 and Sec. 4.2.5).

We also tested the dependence of entrainment on the value of n with various $15 M_{\odot}$ models with values of $n = 0.9, 1.2$ and 1.5 (keeping $A = 10^{-4}$, see Table 4.1). The dependence on n is strong. Indeed, values of n slightly larger than 1 (1.2 or 1.5) strongly reduce the total entrained mass (by a factor of 10 or more, see last column of Table 4.1) and values of n slightly smaller than 1 (0.9) lead to significantly more entrainment (by a factor of more than 3). While the dependence on n and A are not

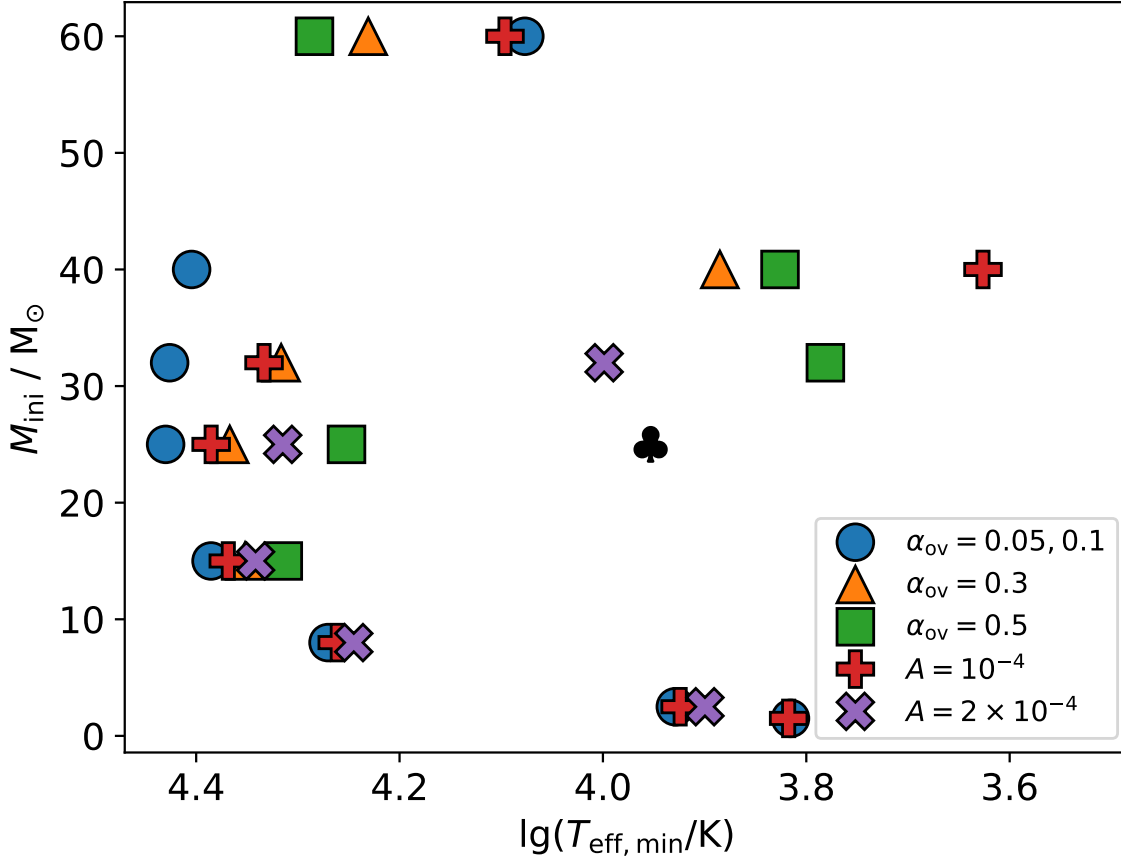


Figure 4.5: Minimum value of effective temperature on the main sequence for all models in the grid (as in Table 4.1). The mixing schemes used are denoted by different coloured markers as in the legend. The one-off $\alpha_{\text{ov}} = 0.7$ model with $25 M_{\odot}$ is shown with the black clover symbol (see Sec. 6.1).

independent, our models tend to show that n cannot be too far from 1. We will compare the values determined in this study to observational constraints and hydrodynamic simulations in the discussion.

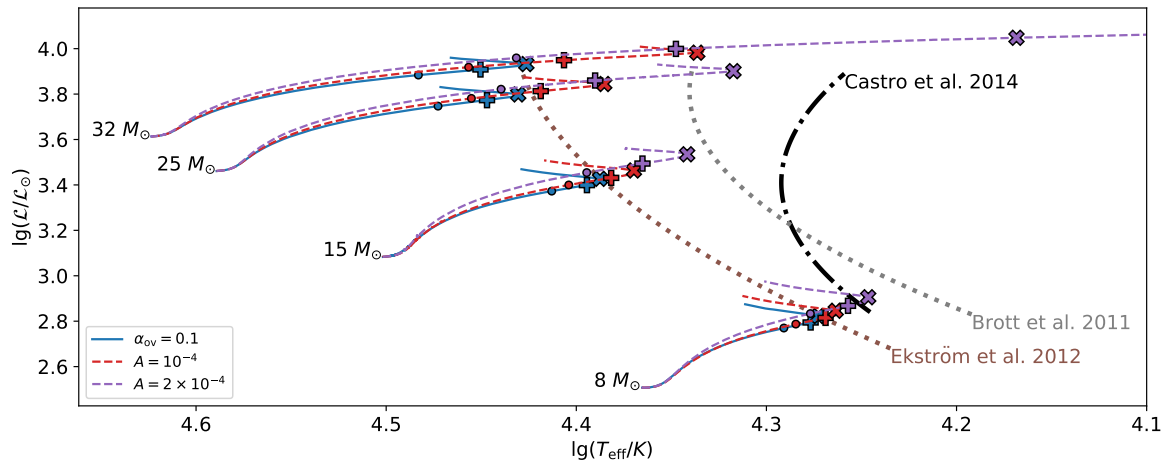


Figure 4.6: sHRD in the mass range 8 to $32 M_{\odot}$ with $\alpha_{ov} = 0.1$ step overshoot and two entrainment values, $A = 10^{-4}$ and 2×10^{-4} . The dotted lines represent the position of the TAMS from model grids with $\alpha_{ov} = 0.1$ (Ekström et al. 2012) and $\alpha_{ov} = 0.335$ (Brott et al. 2011). The dash-dotted line represents the position of the empirical TAMS determined by Castro et al. (2014); see their Table 1 for the polynomial coefficients of the three TAMS lines used in this figure. The dots, pluses and crosses have been placed where the model reaches 90%, 95% and 99% of the MS lifetime respectively.

4.2.4 Impact of entrainment on main sequence width

One of the main observational constraints on stellar models is the MS width. Castro et al. (2014) represents one of the most comprehensive study of MS width at solar metallicity. One of their key findings is that models using a mass-independent value of step overshoot (Ekström et al. 2012; Brott et al. 2011) do not reproduce the observed MS width. Instead, it appears that CBM must increase with initial mass. While the sample used in Castro et al. (2014) is far from complete, it is worth comparing our new entrainment models with models with various amounts of step overshoot and the MS width deducted by Castro et al. (2014). Castro et al. (2014) find that the MS generally extends to a $\lg(T_{\text{eff}}) \sim 4.3$ over a range of luminosities, which corresponds to stars in the mass range $\sim 10 - 20 M_{\odot}$. Above $20 M_{\odot}$, the MS does not seem to have a well-defined cool end and instead appears to extend down to very cool temperature.

Figure 4.5 shows the minimum effective temperature, $T_{\text{eff,min}}$ reached on the MS by each model in the grid. $T_{\text{eff,min}}$ for the default step overshoot models is shown with blue disks and we can see that they indeed predict an MS cool edge that deviates from the observed $\lg(T_{\text{eff}}) \sim 4.3$ further as the mass of the model increases from $10 M_{\odot}$ upwards. We also see that these models do not predict the observed widening of the MS above $20 M_{\odot}$. As discussed in the previous section, entrainment models with $A = 10^{-4}$ and $n = 1$ (red pluses) reproduce the main features of the default ($\alpha_{\text{ov}} = 0.1$) step overshoot models (MS lifetime and HRD tracks). Thus as expected, the $T_{\text{eff,min}}$ of the entrainment models is also hotter than the observed one for stars between 10 and $20 M_{\odot}$. One difference appears for stars above $20 M_{\odot}$ with the entrainment models predicting a cooler edge for the $32 M_{\odot}$ model and a very cool edge for the $40 M_{\odot}$. The $60 M_{\odot}$ models do not follow this trend because they experience strong mass loss towards the end of the MS, which keeps the models on the hot side of the HRD.

Increasing the value of A from 10^{-4} to 2×10^{-4} (purple crosses) provides a reasonable match to the observed MS edge at $T_{\text{eff,min}} \sim 4.3$. Indeed, $4.34 \leq T_{\text{eff,min}} \leq 4.24$ in the models between 8 and $25 M_{\odot}$. Furthermore, the $32 M_{\odot}$ model now extends to very cool T_{eff} . While the observational constraints are not very tight, the MS width for lower masses is slightly wider than observations so a larger value of A would not be favoured. The broader MS width can be reproduced with an increased value of α_{ov} (e.g. with $\alpha_{\text{ov}} = 0.5$, green squares) but in this case, the MS width for lower mass stars would be too wide. The reason why the entrainment models have broader MS width for more massive stars is due to the mass dependence of Ri_B discussed in Sec. 4.2.2, which is used in the entrainment law. This means that the entrainment law provides a partial physical explanation for the apparent mass dependence of the overshooting parameters and a way of providing a much better fit to the observations with a single value of the parameters A and n , which is harder for other CBM such as step overshoot or exponentially decaying diffusion coefficients. Whilst the fit to the terminal age main sequence (TAMS) edge could be improved, for example by varying n in addition to A , the usefulness of this approach would be limited. Other factors such as rotation, metallicity variations and different mass loss prescriptions could provide

additional mass-dependent factors which are not included in these models.

Castro et al. (2014) gathered observations of galactic stars and placed them on an sHRD (Langer & Kudritzki 2014), in which they show the density of observed stars in each region of the HRD. Since the sample is incomplete and possibly biased (Vink et al. 2010; McEvoy et al. 2015), it is difficult to compare densities of stars across the HRD. Nevertheless, it is still interesting to determine what fraction of the MS lifetime models spend in a given location in the HRD. This is indicated in Fig. 4.6 (dots at 90% of the MS lifetime, pluses at 95% and crosses at 99%).

Figure 4.6 shows our models on an sHRD so that we can compare directly to these observations. We focus on the 8 to 32 M_{\odot} range, which encompasses the region of the sHRD in which there is a clear observed TAMS boundary (marked on Fig. 4.6 with the dash-dotted line). Also shown are the TAMS boundaries obtained by Castro et al. (2014) from two model grids: Ekström et al. (2012) using $\alpha_{\text{ov}} = 0.1$ and Brott et al. (2011) using $\alpha_{\text{ov}} = 0.335$.

The Ekström et al. (2012) step overshoot value of $\alpha_{\text{ov}} = 0.1$ was calibrated using models on the lower MS, such as our 2.5 M_{\odot} models. As such, its TAMS boundary is closest to the Castro et al. (2014) empirical boundary in the lower mass range, but deviates strongly at higher masses. Conversely, the Brott et al. (2011) step overshoot value of $\alpha_{\text{ov}} = 0.335$ was calibrated at 16 M_{\odot} and corresponds best to the Castro et al. (2014) TAMS in the middle of the mass range, deviating at both the high-mass and low-mass extremes. This suggests that when using step overshoot to determine CBM, a mass-dependent α_{ov} is needed in models to reproduce observations over a large mass range.

The entrainment law naturally accounts for the mass dependence of CBM through the mass dependence of Ri_B (see Sec. 4.2.2). In Fig. 4.6, the entrainment models have a markedly different TAMS boundary shape (approximated by the positions of the cross markers) with an increased widening of the MS with increasing mass. In particular, the $A = 2 \times 10^{-4}$ model is closer to the Castro et al. (2014) observed TAMS than both the Ekström et al. (2012) and Brott et al. (2011) TAMS boundaries for the 8 and 25 M_{\odot} models. Whilst the MS width for 32 M_{\odot} models is unconstrained by the Castro et al.

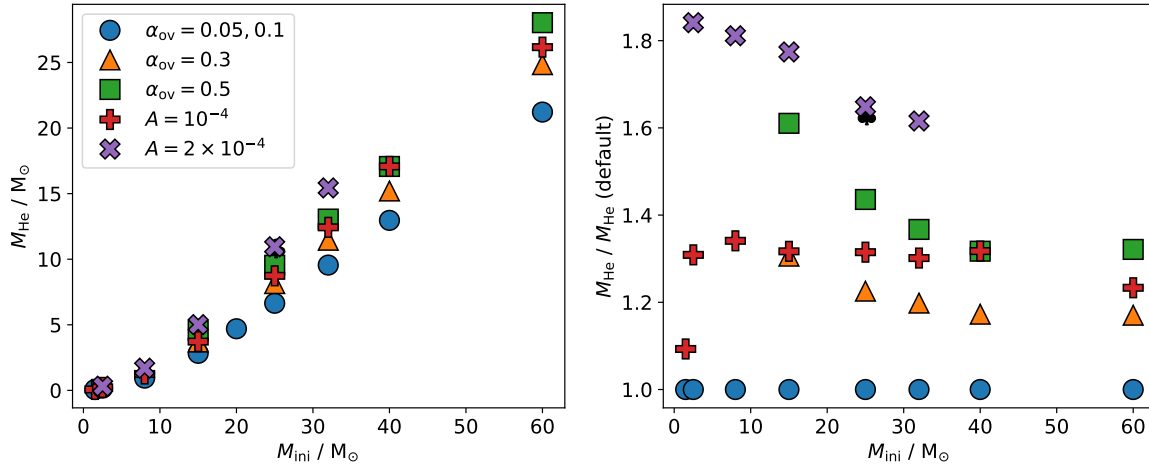


Figure 4.7: Final helium core mass, M_{He} , for various values of step overshoot α_{ov} and entrainment parameter A . All entrainment models use $n = 1$. Blue circles represent the default value of α_{ov} , which is 0.05 for $1.5 M_{\odot}$ and 0.1 otherwise. The one-off $\alpha_{\text{ov}} = 0.7$ model with $25 M_{\odot}$ is shown with the black clover symbol, nearby the $A = 2 \times 10^{-4}$ model (see Sec. 6.1). *Left*: Absolute value of M_{He} against initial mass. The $\alpha_{\text{ov}} = 0.1$ point at $20 M_{\odot}$ is taken from the Ekström et al. (2012) grid. *Right*: M_{He} normalised by the default step overshoot value.

(2014) observations, the $A = 2 \times 10^{-4}$ model does fulfil the requirement of reaching very low temperatures, with $\lg T_{\text{eff}} \leq 4.2$ at 99 per cent of the full MS lifetime.

4.2.5 Impact of entrainment on helium core masses and lifetimes

The type and degree of CBM also affects the mass of the helium core at the end of the MS. The size of this core, whilst not directly observable, has very important implications for post-MS evolution. The compactness and explodability of pre-supernova models is dependent on the post-MS structure, in which the helium core plays an important role (O’Connor & Ott 2011; Ertl et al. 2016; Sukhbold, Woosley & Heger 2018; Chieffi & Limongi 2020). Additionally, since the evolution is driven by the conditions in the core, CBM parameters that produce large cores can mimic the results of more massive models with less CBM.

In Table 4.1, the helium core mass at the end of the MS, M_{He} , is given in the penultimate column. We define M_{He} as the mass of the convective core (including CBM) when the central hydrogen mass fraction drops to one per cent. This definition gives similar results to taking the mass coordinate at which the hydrogen mass fraction drops to one per cent at the last time step of the MS.

Figure 4.7 shows both M_{He} (*left*) and M_{He} divided by its value in the default step overshoot model (*right*). As expected, the left panel shows that larger amounts of CBM produce larger core masses at the end of the MS. In absolute terms, this increase in core mass is greatest in the more massive stars. In the right-hand panel, the majority of CBM choices show the opposite trend, with a greater effect of CBM on relative core mass for the lower-mass models. This is particularly true for $\alpha_{\text{ov}} = 0.5$. In contrast, the $A = 10^{-4}$ models increase M_{He} by ~ 30 per cent across the mass range of the grid, except for the $1.5 M_{\odot}$ model which displays a milder change in core mass.

The value of entrainment that best produces the Castro et al. (2014) MS width in Fig. 4.6 is $A = 2 \times 10^{-4}$. As can be seen in the right-hand panel of Fig. 4.7, this value of A creates helium cores which are a factor of 1.6 to 1.8 larger than using default step

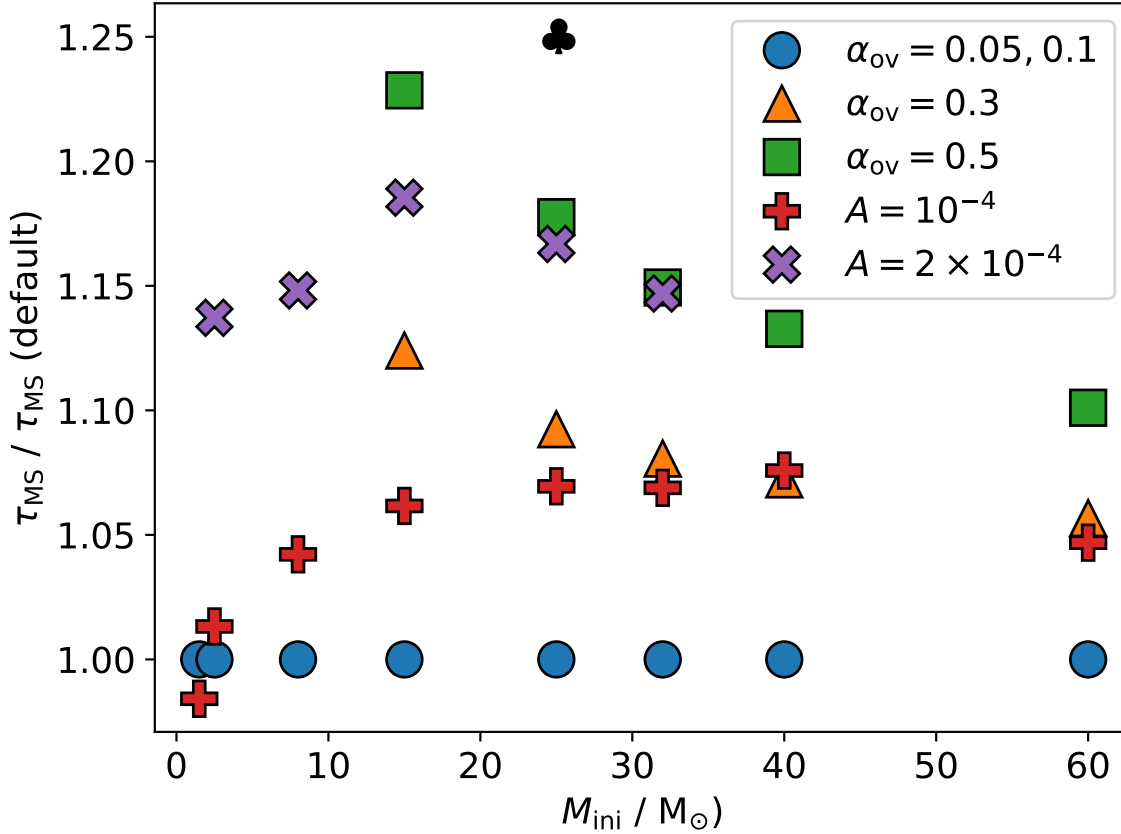


Figure 4.8: Main sequence lifetime relative to the default step overshoot models ($\alpha_{\text{ov}} = 0.05$ for $1.5 M_{\odot}$, 0.1 otherwise). The one-off $\alpha_{\text{ov}} = 0.7$ model with $25 M_{\odot}$ is shown with the black clover symbol (see Sec. 6.1).

overshoot models. The $20 M_{\odot}$ point (taken from Ekström et al. 2012) in the left-hand panel of Fig. 4.7 illustrates the implications of this; a $15 M_{\odot}$ model with $A = 2 \times 10^{-4}$ has a similar helium core mass to an $\alpha_{\text{ov}} = 0.1$ model, which is $5 M_{\odot}$ more massive initially. This shift of at least $5 M_{\odot}$ has wide-ranging implications for massive star evolution and their fate. Examples include the upper mass limit of observed supernova progenitors (Smartt 2009) and the mass range of black hole production (e. g. Chieffi & Limongi 2020).

Figure 4.8 shows the MS lifetime, τ_{MS} (column 5 in Table 4.1), relative to the

default step overshoot case for various CBM parameters across the mass range of the grid. This figure shows similar trends to the right-hand panel of Fig. 4.7, but with more CBM producing longer lifetimes rather than larger cores. When comparing step overshoot models only, it is clear that the relative increase in lifetime is smaller for higher-mass stars. The entrainment models show more complicated non-monotonic behaviour. However, it is important to note that the relative effect of increasing CBM on lifetime is milder compared to the effect on helium core masses; the maximum relative increase in lifetime in Fig. 4.8 is nearly 15 per cent for the $2.5 M_{\odot}$ model, whereas M_{He} is increased by a ~ 80 per cent for the same model in Fig. 4.7.

The strong effect on core masses and more modest effect on lifetimes can be understood from the difference between step overshoot and entrainment discussed in Sec. 4.2.3 and highlighted in Fig. 4.4. Whilst the mass contained within the CBM region in the step overshoot models decreases with time, entrainment is a cumulative process, which builds up over the main sequence and thus leads to much larger final core masses.

Another important difference for the later evolution is the initial sizes of convective cores. The step overshoot model starts with a much larger core. This will leave an imprint on the structure of that part of the star, which will affect the behaviour of later stages, e. g. the intermediate convective zone (Kaiser et al. 2020).

5 Models with shear mixing

In Ch. 4, I showed that entrainment can reproduce the advancement of the convective boundary with time seen in 3D simulations of convection, whilst also satisfying some observational constraints on the main sequence width. These elements relate to the position of the convective boundary in the star. However, the chemical structure in entrainment models still shows a step function profile, as in the step overshoot models. Both the 3D simulations and asteroseismic observations show that the convective boundary in fact has a smooth profile (Arnett & Moravveji 2017).

It is not known which processes are dominant in shaping the boundary. However, Freytag, Ludwig & Steffen (1996) suggested that the boundary shape could be described by an exponentially decaying diffusion coefficient. This was later adapted by Herwig (2000) into the form

$$D_{\text{CBM}} = D_0 \exp\left(\frac{-2z}{fH_P}\right), \quad (5.1)$$

where D_0 is a reference value of the diffusion coefficient within the convective region, z is the distance from the reference point, f is a parameter and H_P is the pressure scale height. I have added this prescription to the Geneva stellar evolution code, `GENEC`, as described in Ch. 3. The physical process posited as the origin of this exponentially decaying diffusion is Kelvin-Helmholtz instabilities resulting from shear as the convective flows turn at the boundary. The reasons for this and possible alternatives will be discussed in Ch. 6. In this chapter, I will investigate whether this shear mixing fits the convective boundary shape seen in the 3D simulations. Other processes responsible for the shape of the boundary will be discussed in Ch. 6.

5.1 3D carbon shell models

The 3D simulations discussed in this chapter were run by A. Cristini and are described in detail in Cristini et al. (2019). However, the relevant features of these models and a

new analysis of the convective boundary shape will also be described here.

As described in Cristini et al. (2019), the simulations were run with the `PROMPI` code and model a portion of a $15 M_{\odot}$ star in the late stages of evolution, between core carbon burning and core oxygen burning. This portion is a 3-dimensional box centred on a convective region known as the second carbon shell, in which carbon burning is driving convection from the bottom of the region. The simulation region has a resolution of 512^3 and uses plane-parallel geometry. The physical structure inside the box is initialised using a 1D `GENEC` model.

A series of simulations of this region were calculated, each with a different boosting factor, ranging from 1 to 3.3×10^4 . This factor multiplies the reaction rate, speeding up the convection. This is necessary since the computational time available for the simulation is limited¹, and a non-boosted simulation would produce too few convective turnovers to study time-dependent processes (such as entrainment) accurately. In this chapter, each 3D simulation will be referred to by its boosting factor, for example `eps1k` for the 1000 times boosted case, as in Cristini et al. (2019).

Figure 5.1 (Cristini et al. 2017 Fig. 1) shows the structure of the 1D `GENEC` model used to initialise the 3D simulations. The coloured areas show the convective regions, with the colour representing the mach number of the convective speed. The large red and yellow area is the convective envelope, which appears at around 10^6 yr before the last time step and persists until the end. The blue and mint green areas are the deep convection zones (cores and shells). The vertical red bar, positioned on the second carbon-burning shell, shows where the 3D simulations were run. Its height shows the extent in mass contained in the vertical direction of the 3D simulation area.

Since the 3D simulations were started from a 1D `GENEC` model, they needed to be seeded with small perturbations to allow convection to develop. The beginning of the simulation time (known as the transient phase) is spent reaching the steady

¹The computational cost of the simulations used is 225.6, 477.5, 282.8 and 293.0 kCPU-hr for the 1000, 3000, 10000 and 33000 times boosted simulations respectively. This computational cost is best dealt with using high performance computing facilities, although time on these machines is competitive.

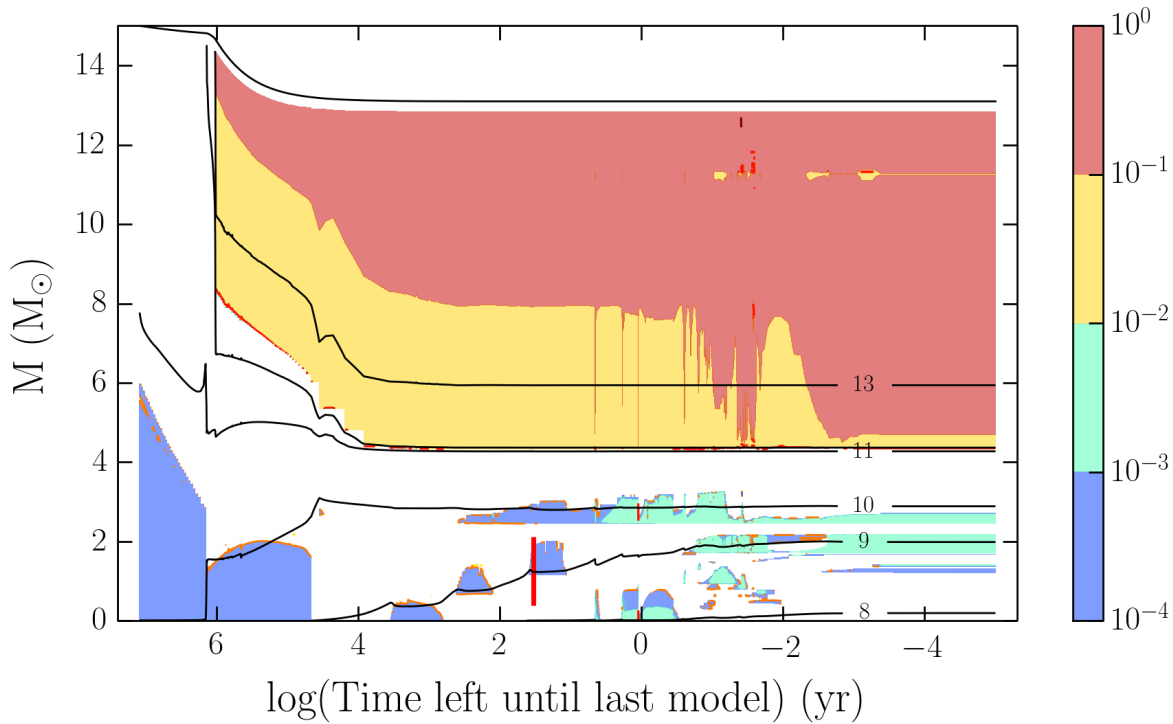


Figure 5.1: Structure diagram (Cristini et al. 2017 Fig. 1) showing the initial 1D model for the 3D carbon shell simulations, with mass coordinate on the y -axis and the logarithm of the time until the last model time step on the x -axis. The coloured areas show the position of convective regions, with the mach number of the flow given by the colour bar. Also plotted are lines of constant radius showing the expansion or contraction of regions in the star as it evolves. The red bar shows the time (x -axis position) and extent in mass (size in the y -direction) of the 3D simulations discussed in this chapter.

state where convection, driven by nuclear burning, has settled into the entire region of Schwarzschild instability.

To determine whether the convective shear prescription described by Eq. 5.1 reproduces the boundary shape seen in 3D simulations, the data from Cristini's models have been reanalysed. The upper panels of Fig. 5.2 show the profiles of the horizontally-averaged mean atomic mass, \bar{A} , for both the upper and lower boundaries of the `eps1k` 3D carbon shell simulation. The lower panels show the first and second spatial derivatives of \bar{A} .

The simulation area is split into three distinct zones, with the convective region in the middle, a stable region above and a stable region below. In the initial 1D model, both the lower and upper stable regions have flat \bar{A} profiles. For the lower region this is due to the previous history of carbon burning in the core and the first shell, whilst for the upper stable region it is due to core helium burning. The convective region also has a flat \bar{A} profile due to the fast convective mixing ongoing in the initial model, with $\bar{A} \sim 16.25$ (a value intermediate between the two stable region values). These plateau values in the three regions were used to calculate the positions of the square markers in Fig. 5.2 which represent 5% and 95% of the difference in \bar{A} between the convective and stable regions. The positions of the markers are then given by

$$\begin{aligned}\bar{A}_{5\%} &= \bar{A}_{\text{conv}} + 0.05(\bar{A}_{\text{stable}} - \bar{A}_{\text{conv}}) \\ \bar{A}_{95\%} &= \bar{A}_{\text{conv}} + 0.95(\bar{A}_{\text{stable}} - \bar{A}_{\text{conv}})\end{aligned}\tag{5.2}$$

where \bar{A}_{conv} and \bar{A}_{stable} refer to the plateau values of \bar{A} in the convective and stable sides of each boundary respectively. Thus $\bar{A}_{5\%}$ is the value of \bar{A} which has changed from \bar{A}_{conv} by 5% of the difference $\bar{A}_{\text{stable}} - \bar{A}_{\text{conv}}$, and $\bar{A}_{95\%}$ is the value for a 95% change. The radial position of the boundary, r_b , is similarly defined here as the position at which \bar{A} is halfway between its convective and stable region values:

$$\bar{A}_{50\%} = \bar{A}_{\text{conv}} + 0.5(\bar{A}_{\text{stable}} - \bar{A}_{\text{conv}}).\tag{5.3}$$

The positions corresponding to $\bar{A} = \bar{A}_{50\%}$ are marked for each boundary at the radius $r = r_b$ with the dashed line in Fig. 5.2.

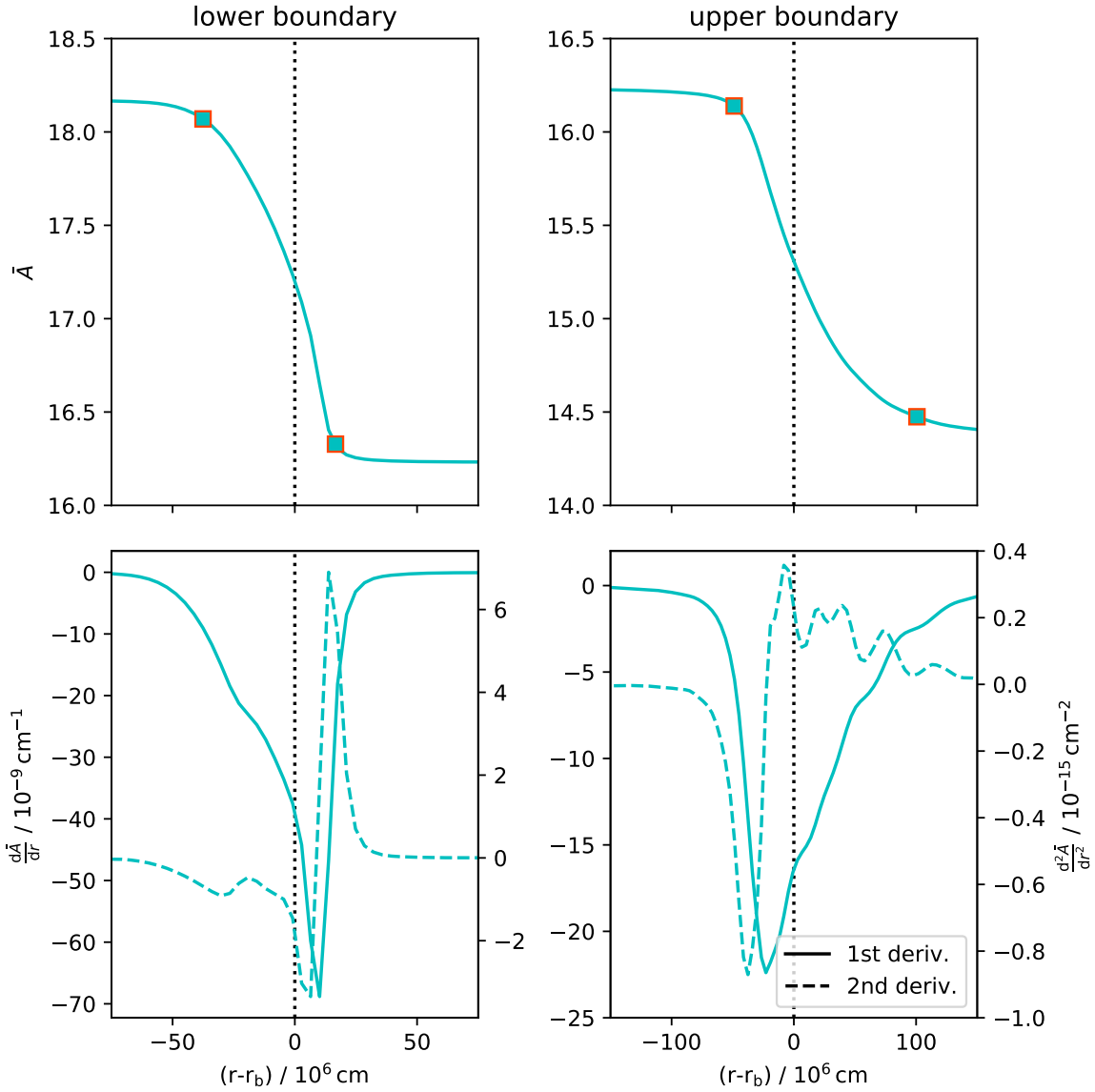


Figure 5.2: Profiles of horizontally-averaged mean atomic mass (\bar{A} , upper panels) and its spatial derivatives (lower panels, first derivative on the left axis and second derivative on the right) at the convective boundaries of the `eps1k` carbon shell simulation. The markers in the upper panels represent 95% and 5% of the difference between the plateau values of \bar{A} either side of the boundary. The radius r_b (the 0 of the x -axis) is positioned at the 50% mark between the two plateau values.

The profiles in Fig. 5.2 show several key features. Firstly, the upper and lower boundaries do not have the same width (note the difference in x -axis scale on each side of Fig. 5.2). The distance between the 95% and 5% markers is 54×10^6 cm for the lower boundary and 150×10^6 cm for the upper boundary. In Cristini et al. (2017) and Cristini et al. (2019), this is interpreted as the lower boundary being stiffer, hence more resistant to entrainment, which is reflected in a higher bulk Richardson number for the lower boundary.

Secondly, \bar{A} changes smoothly from the convective region value to the plateau value in the stable region. This suggests that whilst the convective region is very quickly mixed, there is also partial mixing at the boundary with the stable region.

Lastly, the shape of the boundary is asymmetric, as shown by the derivatives in the lower panels. Whilst the shape of the \bar{A} profile is roughly sigmoid, the peak of the first derivative (or alternatively the zero of the second derivative) does not occur at a radius of $r - r_b = 0$, which would be expected for a symmetrical sigmoid profile. For both the upper and lower boundaries, the boundary position as defined by Eq. 5.3 is closer to the convective plateau region than the stable plateau region. The highest-magnitude peaks of the first and second derivative are closer still to the convective region.

Given that the profiles shown in Fig. 5.2 are horizontally averaged, it is useful to also look at non-averaged profiles to determine whether the profile shapes are affected by the averaging. Figure 5.3 shows these data from the `eps1k` carbon shell simulation. In this figure, the position in one horizontal direction is kept constant in the centre of that axis, whilst the \bar{A} profiles on the other horizontal axis are coloured according to their position. The plot therefore represents a vertical 2D slice through the simulation area with the value of \bar{A} given for each point in the slice.

Figure 5.3 shows that there are some differences in the profile of \bar{A} depending on the horizontal position, but these are minimal for the stiffer lower boundary. The region with the most variation between profiles is at the edge of the convective region ($r - r_b \sim 20 \times 10^6$ for the lower boundary, $\sim -50 \times 10^6$ for the upper boundary). For example, the upper boundary profiles at a horizontal position of ~ 1250 to 1500×10^6 cm

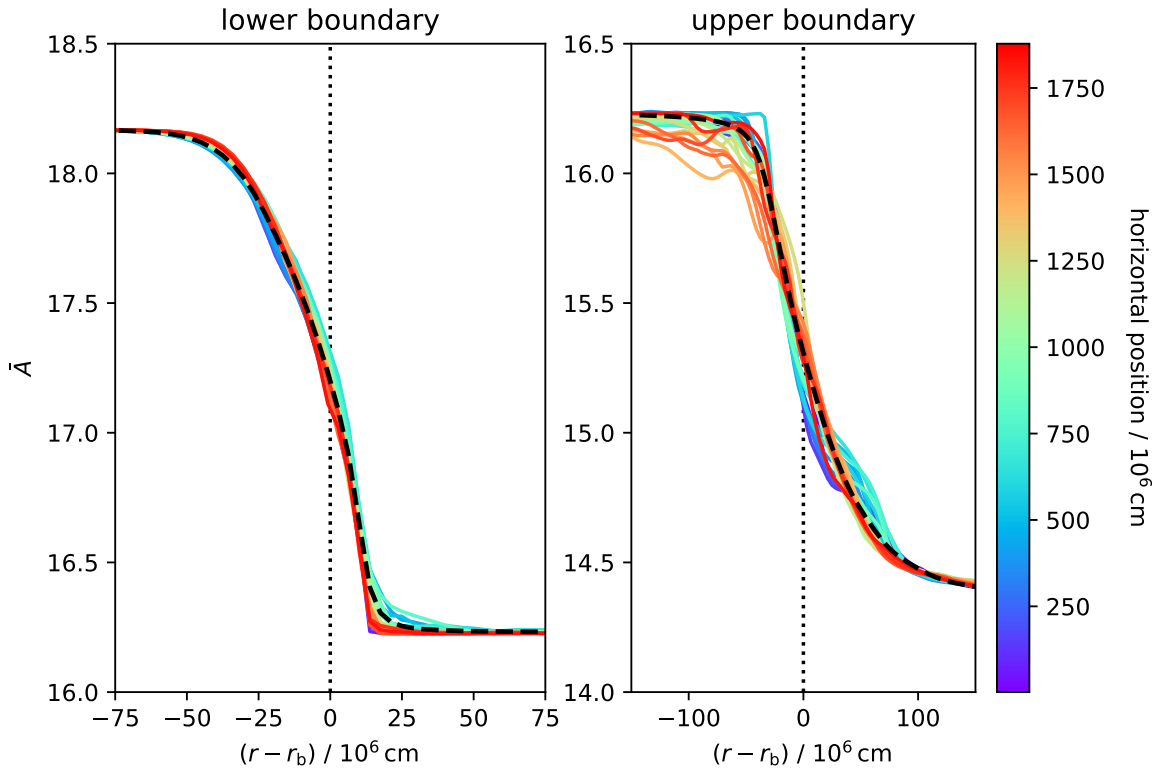


Figure 5.3: Individual (non-horizontally-averaged) radial (x -axis) profiles of \bar{A} at the convective boundaries of the 1000 times boosted 3D carbon shell simulation (`eps1k`). The colour bar denotes the position of the individual profiles in one horizontal direction (y -axis), whilst the position in the second horizontal direction (z -axis) remains fixed to the middle of the convective zone. For clarity, only one in every twenty profiles is plotted. The horizontally-averaged profile is shown by the black dashed line.

have a shallower drop in \bar{A} at the top of the convective region than the other profiles. This could be caused by an influx of material from the stable region, pulled in by a corresponding rise in material from the convective region. In any case, the variation in the profile shape is more extreme at the edge of the convective region than further away, where the profiles remain similar at most horizontal positions. The horizontally-averaged profile, shown with the dashed black line, does appear to be representative of the shapes seen in the non-averaged profiles.

The energy generation rate boosting factor should also be considered as affecting the boundary shape, since increasing this factor increases the convective speeds. Figure 5.4 shows \bar{A} profiles for four of the boosting cases (those which have completed > 10 convective turnovers). To make sure that the profiles are comparable, each (except `eps33k`) was taken from the last time step of the simulation when the convection was well beyond the initial transient phase. The `eps33k` simulation was taken at an earlier time step (but still past the transient phase), because the upper boundary of the last time step had progressed near the top of the simulation area, making it difficult to define a value for \bar{A}_{stable} .

Each of the higher boosting cases in Fig. 5.4 shows similar features to the `eps1k` case shown previously in Fig. 5.2, that is a narrower lower boundary than upper, a smooth transition from \bar{A}_{conv} to \bar{A}_{stable} and asymmetry. However, there appear to be some effects from the boosting factor. For the both boundaries, the boundary centre $r = r_b$ gets further from the $\bar{A}_{5\%}$ marker as the boosting factor increases, suggesting that \bar{A} changes more slowly near the convective region for higher boosting factors. In addition, the point at which the gradient has its highest magnitude appears to be closer to the boundary centre for the higher boosting factors, although this may be indicative of the same effect and is not clear for the lower boundary due to the more complex profile. However, the profiles are still asymmetric.

To summarise, Fig. 5.4 shows that there is a region which is strongly (but not completely) mixed near the convective region which is larger for higher boosting factors. This roughly corresponds to the region between $r_{5\%}$ and r_b . There is also a more weakly mixed region beyond r_b , the shape of which does not appear to be affected by

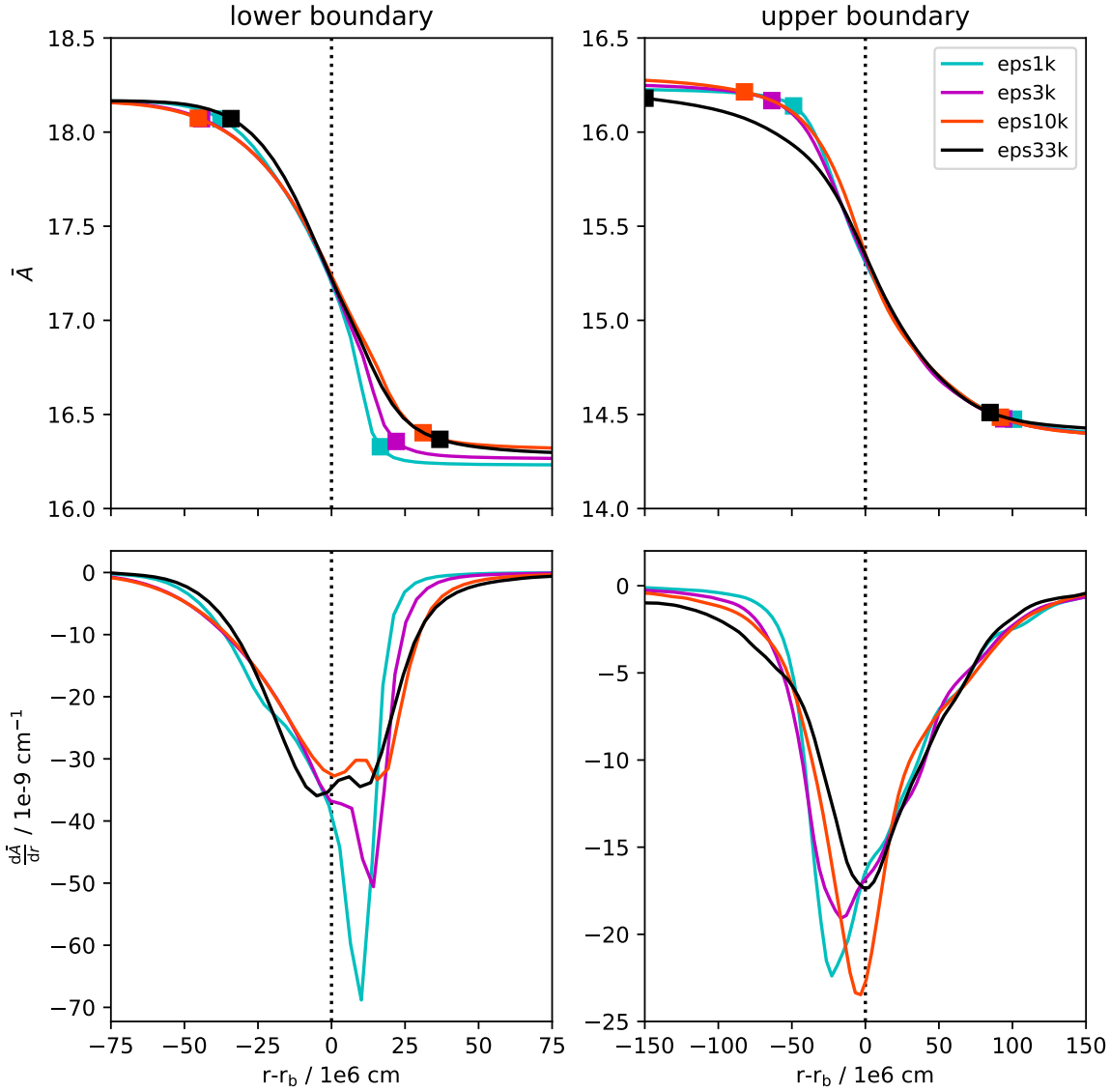


Figure 5.4: Profiles of horizontally-averaged mean atomic mass, \bar{A} , and its spatial derivative for the `eps1k`, `eps3k`, `eps10k` and `eps33k` simulations. As in Fig. 5.2, the square markers represent 95% and 5% of the difference between the plateau values of \bar{A} either side of the boundary and the dashed line at $r = r_b$ is positioned at the 50% mark between the two plateau values.

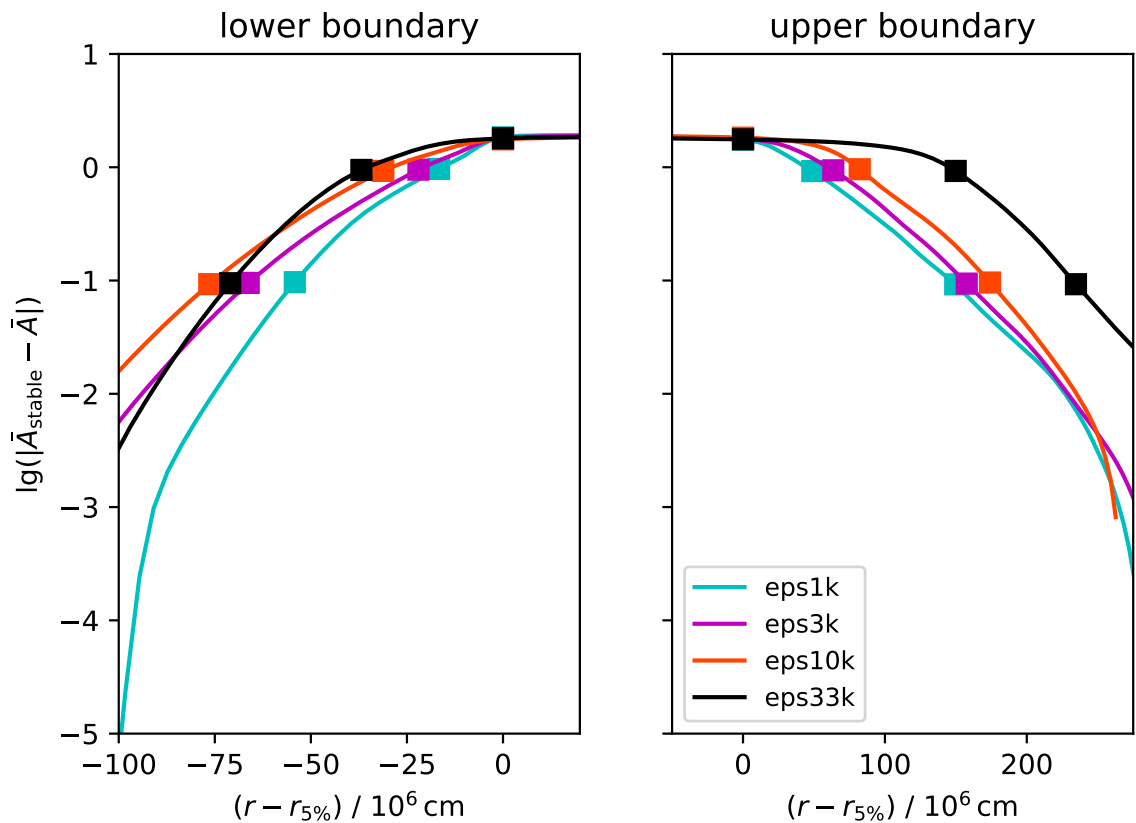


Figure 5.5: Logarithm of the change in \bar{A} with respect to \bar{A}_{stable} against radius for the 3D carbon shell simulations. The profiles are positioned on the radial axis such that the boundary edge at $r = r_{5\%}$ is at zero. Here there are three square markers per profile, representing $\bar{A} = \bar{A}_{5\%}$, $\bar{A}_{50\%}$ and $\bar{A}_{95\%}$.

the boosting factor.

To examine the change \bar{A} further away from the boundary, Fig. 5.5 shows the logarithmic change in \bar{A} with respect to \bar{A}_{stable} for each boundary plotted against radius. The zero of the radial axis is at the position $r = r_{5\%}$ so that the beginning of the change in \bar{A} from the convective region value is in the same place for each profile. This figure shows how \bar{A} approaches \bar{A}_{stable} further away from the convective region. In all cases shown in Fig. 5.5 (except the eps33k lower boundary), the logarithmic profiles appear to have similar gradients in the region between $r = r_{50\%}$ and $r = r_{95\%}$ (shown

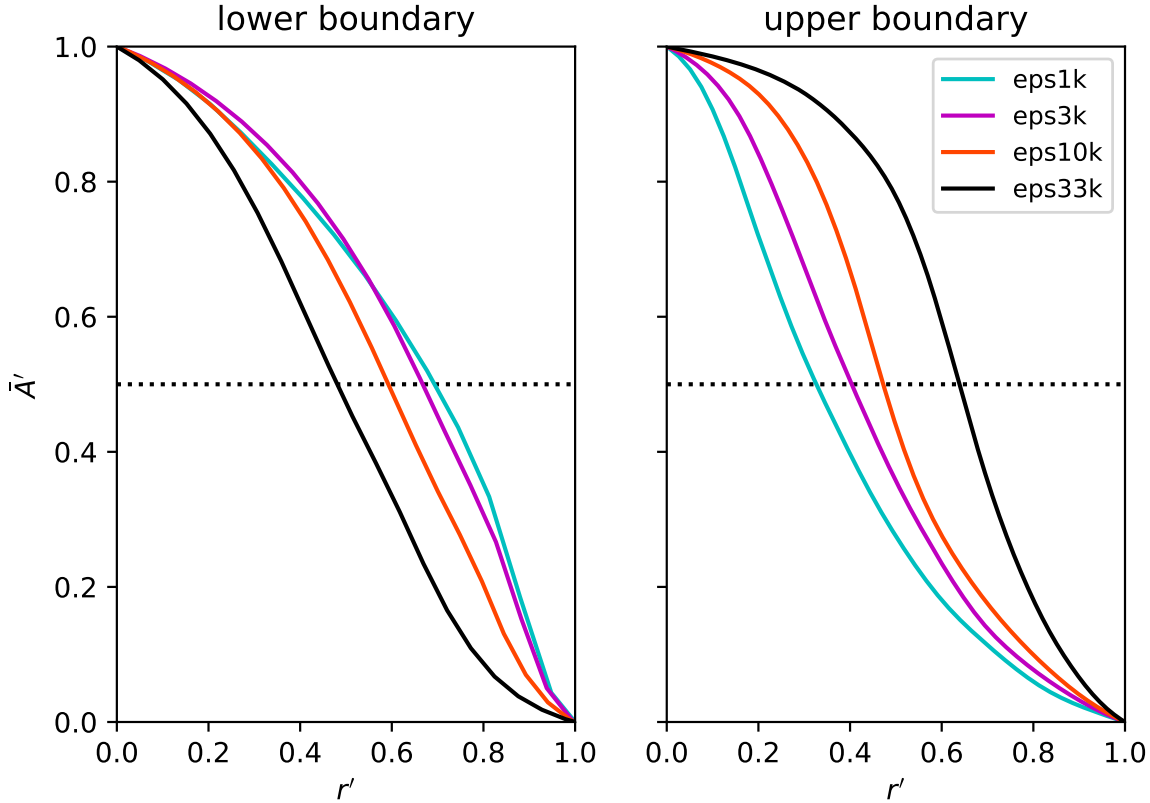


Figure 5.6: Comparison of boundary shape for the `eps1k`, `eps3k`, `eps10k` and `eps33k` simulations. \bar{A} and the radius have been normalised such that they vary between 0 and 1 between the 5% and 95% boundary markers, according to Eq. 5.4. The centre of the boundary at which $\bar{A} = \bar{A}_{50\%}$ is marked with the dotted line at $\bar{A}' = 0.5$

by the two square markers furthest away from $r - r_{5\%} = 0$). However, the profiles are shifted further from $r - r_{5\%} = 0$ as the boosting factor increases. This results from the increase in boundary width with boosting factor that is shown in Fig. 5.4. In the region beyond $r = r_{95\%}$ (furthest away from $r - r_{5\%} = 0$), the profile shapes do not appear to be as similar, although this region is beyond the convective boundary and inside the stable region, as evidenced by the very small values of $|\bar{A} - \bar{A}_{\text{stable}}|$ there.

Since the boosting factor affects boundary width, another useful way to examine the difference in boundary shape is to transform the axes of r and \bar{A} according to the

boundary values $r_{5\%}$, $r_{95\%}$, $\bar{A}_{5\%}$ and $\bar{A}_{95\%}$ to make them directly comparable. This transformation takes the form

$$\begin{aligned} r' &= \frac{r - r_{5\%}}{r_{95\%} - r_{5\%}} \\ \bar{A}' &= \frac{\bar{A} - \bar{A}_{5\%}}{\bar{A}_{95\%} - \bar{A}_{5\%}} \end{aligned} \tag{5.4}$$

such that r' and \bar{A}' vary between zero and one across the width of the boundary. Figure 5.6 shows the upper and lower boundaries of the four 3D carbon shell simulations using the transformations in Eqs. 5.4 as the axes. The stronger mixing near the convective region ($r' = 1$ for the lower boundary, $r' = 0$ for the upper) is apparent, particularly for the upper boundary. Here, the gradient of A' is shallower than elsewhere.

The trends with boosting factor in Figs. 5.4, 5.5 and 5.6 show that an increase in boosting factor both increases the boundary width and changes the boundary shape. In particular, the higher boosting factors seem to preferentially mix near the convective region, extending the region of strong mixing and leaving the region of weaker mixing further away from the boundary relatively unaffected. Since the main effect of the boosting factor is to change the convective speed in the simulation, these trends suggest that there are at least two separate mixing processes at the boundary which depend to a different degree on the convective velocity.

5.2 1D main sequence models

Having examined the properties of the convective boundaries in the 3D carbon shell simulations, the next step is to look at 1D models with shear CBM. Starting with the MS, a grid of models from 8 to $32 M_{\odot}$ was calculated for this purpose. As with the entrainment models in Ch. 4, the models are non-rotating with a metallicity of $Z = 0.014$.

For each mass, there are multiple values of the f parameter controlling the strength of shear mixing ($f = 0.01, 0.03$ and 0.05). This is based on the values of

Table 5.1: Summary of the model grid showing the initial mass M_{ini} , shear CBM parameter f , main sequence lifetime τ_{MS} , logarithm of the minimum effective temperature reached during the MS $\lg(T_{\text{eff,min}})$, logarithm of the average convective diffusion coefficient in the core $\lg\langle D_{\text{conv}}\rangle$ and mass of the helium core at the end of the MS (the two definitions are explained in the text) $M_{\text{He,cc}}$ and $M_{\text{He,1\%}}$.

M_{ini} [M_{\odot}]	f	τ_{MS} [Myr]	$\lg(T_{\text{eff,min}})$ [K]	$\lg\langle D_{\text{conv}}\rangle$ [$\text{cm}^2 \text{s}^{-1}$]	$M_{\text{He,cc}}$ [M_{\odot}]	$M_{\text{He,1\%}}$ [M_{\odot}]
8	0.01	31.5	4.27	10.7	0.806	0.860
8	0.03	35.3	4.25	10.8	0.941	1.14
8	0.05	38.6	4.23	10.8	1.07	1.41
15	0.01	10.8	4.39	11.8	2.61	2.84
15	0.03	11.8	4.36	11.8	3.01	3.49
15	0.05	12.6	4.33	11.8	3.41	4.14
25	0.01	6.15	4.43	12.5	6.26	6.59
25	0.03	6.60	4.38	12.5	7.03	7.84
25	0.05	7.00	4.30	12.5	7.77	8.93
32	0.01	5.20	4.43	12.8	9.03	9.43
32	0.03	5.52	4.34	12.8	10.0	11.1
32	0.05	5.79	4.09	12.8	11.0	12.4

the overshoot parameter, α_{ov} , used in the grid in Ch. 4 and the rough conversion between α_{ov} and f , where $\alpha_{\text{ov}} \sim 10f$ (Claret & Torres 2017; Moravveji et al. 2016).

Table 5.1 shows the grid parameters for the MS models in this chapter. The first quantities listed are the initial model parameters, that is mass, M_{ini} , and CBM parameter, f . Next are quantities describing the extent of the MS: the MS lifetime, τ_{MS} , and the logarithm of the minimum effective temperature reached during the MS, $\lg(T_{\text{eff,min}})$. The end of the MS is defined as the time when the central hydrogen mass fraction reaches 10^{-4} . The last columns are the average value of the convective diffusion coefficient in the core, $\lg\langle D_{\text{conv}}\rangle$, and the size of the helium core at the end of the MS according to two definitions. As in Ch. 4, $M_{\text{He,cc}}$ is taken to be the size of the convective core at a central hydrogen mass fraction of 1%. The other quantity,

$M_{\text{He},1\%}$, is the mass coordinate at which the hydrogen mass fraction reaches 1% in the final time step of the MS.

As can be seen in Tab. 5.1, increasing f leads to an increase in τ_{MS} and a decrease in $\lg(T_{\text{eff,min}})$. This is due to the increase in mixing (both due to the larger size of the CBM region and the faster diffusion) compared to smaller values of f . The increase in lifetime is due to the larger mass of hydrogen available for the star to burn in the extended core, whilst the envelope continues expanding during this increased lifetime, causing T_{eff} to reach lower temperatures. A similar relationship is known to occur for the step overshoot parameter and was also seen in Ch. 4 for the parameter controlling the strength of entrainment, A .

The values of $\lg\langle D_{\text{conv}}\rangle$ in Tab. 5.1 show that the speed of mixing, here represented as a diffusive process, increases with mass. This affects the shear CBM since the value of D_{conv} in the convective core is used as the starting point for the exponential decay of diffusion into the stable region. Hence, stars with higher values of D_{conv} in their cores will experience faster mixing in the shear CBM layer. The average core diffusion coefficient does not seem to be affected by the f parameter, with only the $8 M_{\odot}$ models showing any variation.

As well as average values of $\lg(D_{\text{conv}})$, it is also useful to look at profiles to see how the shear CBM scheme works. Figure 5.7 shows profiles of D_{conv} with different mass (top panel) and f parameter (bottom panel). Since the change of D_{conv} in the CBM region is an exponential decay (Eq. 5.1), the logarithm of D_{conv} changes linearly with radius. For all models in the grid, $\lg(D_{\text{conv}})$ remains constant with radius in the region of the core interior to the shear CBM region, represented for example by the plateaus in the bottom panel where $\lg(D_{\text{conv}}) \sim 12$. However, this plateau value does change throughout the MS, becoming smaller as the core shrinks. In stable regions outside the CBM region, D_{conv} drops to zero, with a cutoff at $D_{\text{conv}} = 100 \text{ cm}^2 \text{ s}^{-1}$. The width of the CBM region does not change significantly with mass if the central hydrogen mass fraction and f parameter are kept constant, since the plateau values of $\lg(D_{\text{conv}})$ are all ~ 10 , as can also be seen in Tab. 5.1. The bottom panel of Fig. 5.7 shows that there is a stronger effect on the width of the CBM region when varying f .

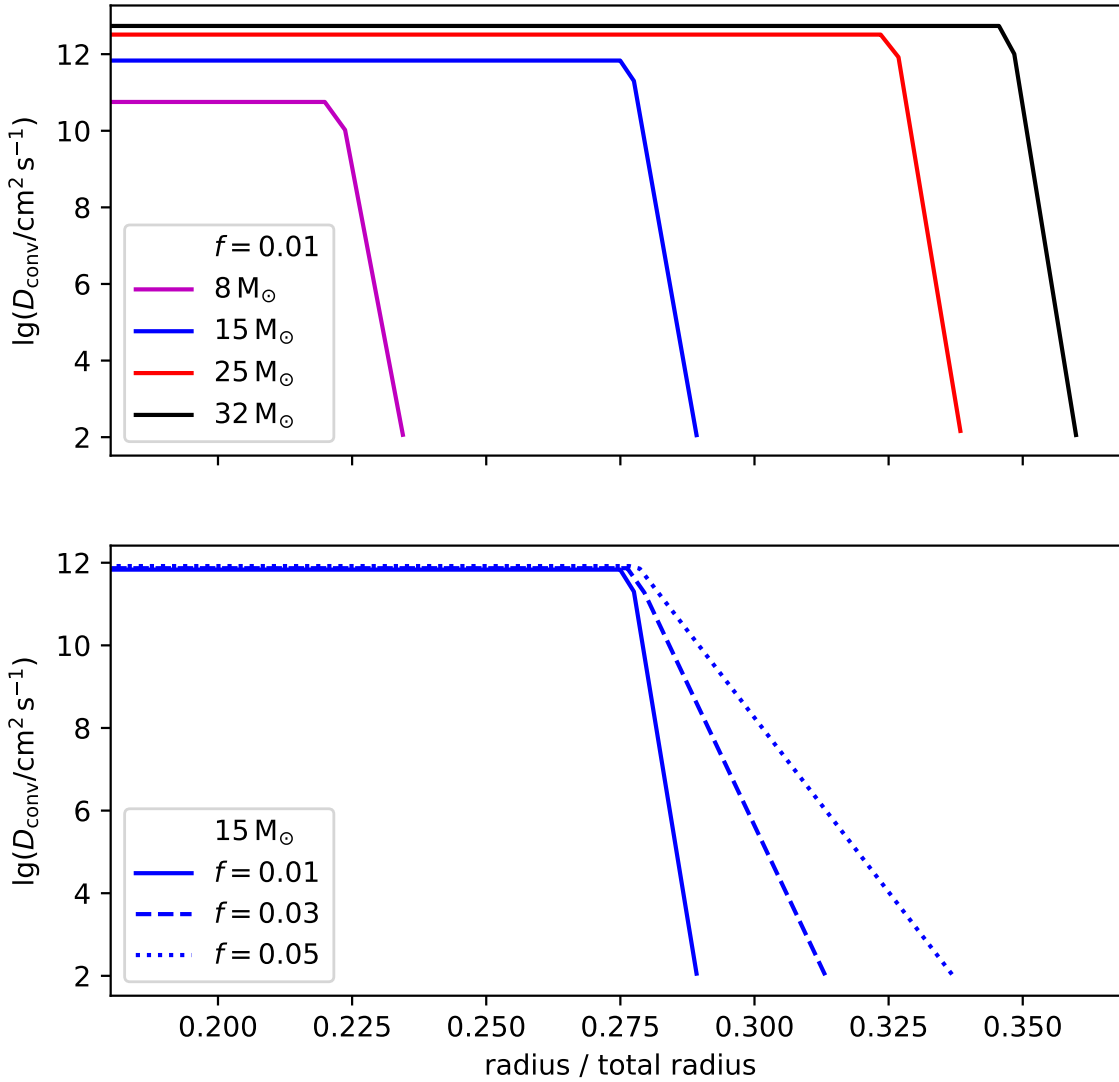


Figure 5.7: Examples of typical profiles of the diffusion coefficient as a function of fractional radius, all taken at a central hydrogen mass fraction of 0.35. *Top:* Models from $8 M_{\odot}$ to $32 M_{\odot}$ models with $f = 0.01$. *Bottom:* $15 M_{\odot}$ models with $f = 0.01$, 0.03 and 0.05.

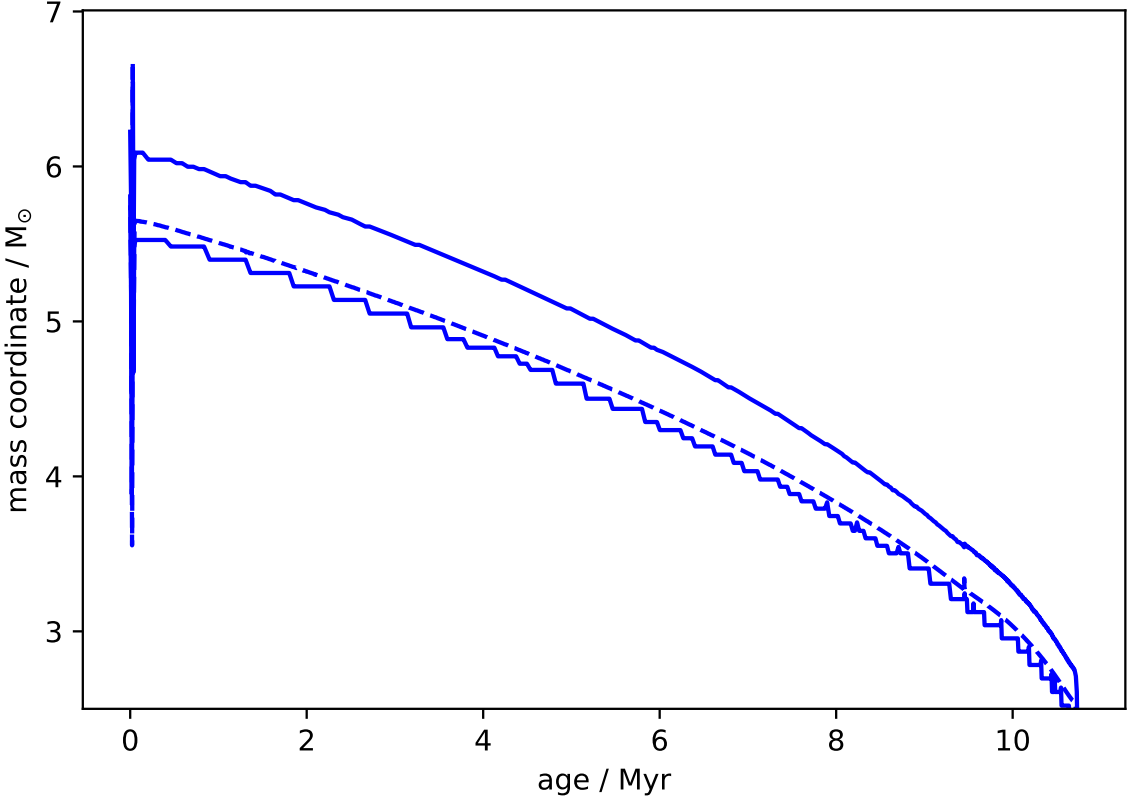


Figure 5.8: Time evolution of the mass of the shear mixing region on top of the convective core for the $15M_{\odot}$ model with $f = 0.01$. The solid lines represent the edges of the shear mixing region whereas the dashed line shows the mass coordinate of the Schwarzschild boundary. The steps on the inner edge of the shear region are related to resolution in the convective region. Since gradients are not typically high in the convective region, it is not as important to resolve this area compared to the exponential slope. See Fig. 5.10

to see the resolution of a typical profile in the carbon shell.

As a compliment to the profiles shown in Fig. 5.7, the time dependence of the size of the CBM region is shown in Fig. 5.8, this time in terms of mass. Whilst this figure uses the $15 M_{\odot}$ $f = 0.01$ model as an example, other masses behave in a similar manner with a core that recedes with time. The dashed line shows the mass of the formal convective region, which is Schwarzschild unstable. The solid lines at both above and below the Schwarzschild boundary show the edges of the shear CBM region. The mass of the CBM region shrinks as the core shrinks, and this causes the plateau value of D_{conv} to reduce with time as well.

The final two columns in Tab. 5.1 show two estimates of the mass of the helium core at the end of the MS, M_{He} . The column $M_{\text{He,cc}}$ calculates the helium core mass in the same way as described in Ch. 4, that is the mass of the fully mixed region at a central hydrogen mass fraction of 1%. The other column, $M_{\text{He,1\%}}$, is the mass coordinate at which the hydrogen mass fraction drops below 1% for the final model in the MS. For the models in Ch. 4, for which there is no partial mixing, the two definitions give similar estimates. However, the models in Tab. 5.1 include a partially-mixed region above an instantaneously mixed core, such that $M_{\text{He,cc}} < M_{\text{He,1\%}}$ for all the models in the grid. The models show the expected result of larger helium cores for stronger mixing (larger f), as seen also in Ch. 4. Also as expected is the fact that the values of $M_{\text{He,cc}}$ are smaller than those of M_{He} for the step overshoot models in Tab. 4.1 (using the conversion $\alpha_{\text{ov}} \sim 10f$), given that the CBM region is not included in that estimate for the shear models but is included for the overshoot models. However, the estimate of the helium core mass given by $M_{\text{He,1\%}}$ is roughly comparable between the shear and overshoot models.

The entire grid of models is presented in Fig. 5.9 in an sHRD in the same way as in Ch. 4. The dot, plus and cross markers represent 90%, 95% and 99% of the MS lifetime respectively; it can be seen that the cross markers of the $f = 0.05$ models, which are near the cool edge of the MS, are further to the right than the lower values of f . This was also shown previously by the decrease in $T_{\text{eff,min}}$ with increasing f in Tab. 5.1. The $f = 0.05$ models have MS widths comparable to their $\alpha_{\text{ov}} = 0.5$ counterparts, further confirming that the rough conversion $\alpha_{\text{ov}} \sim 10f$ holds for the most part in this case.

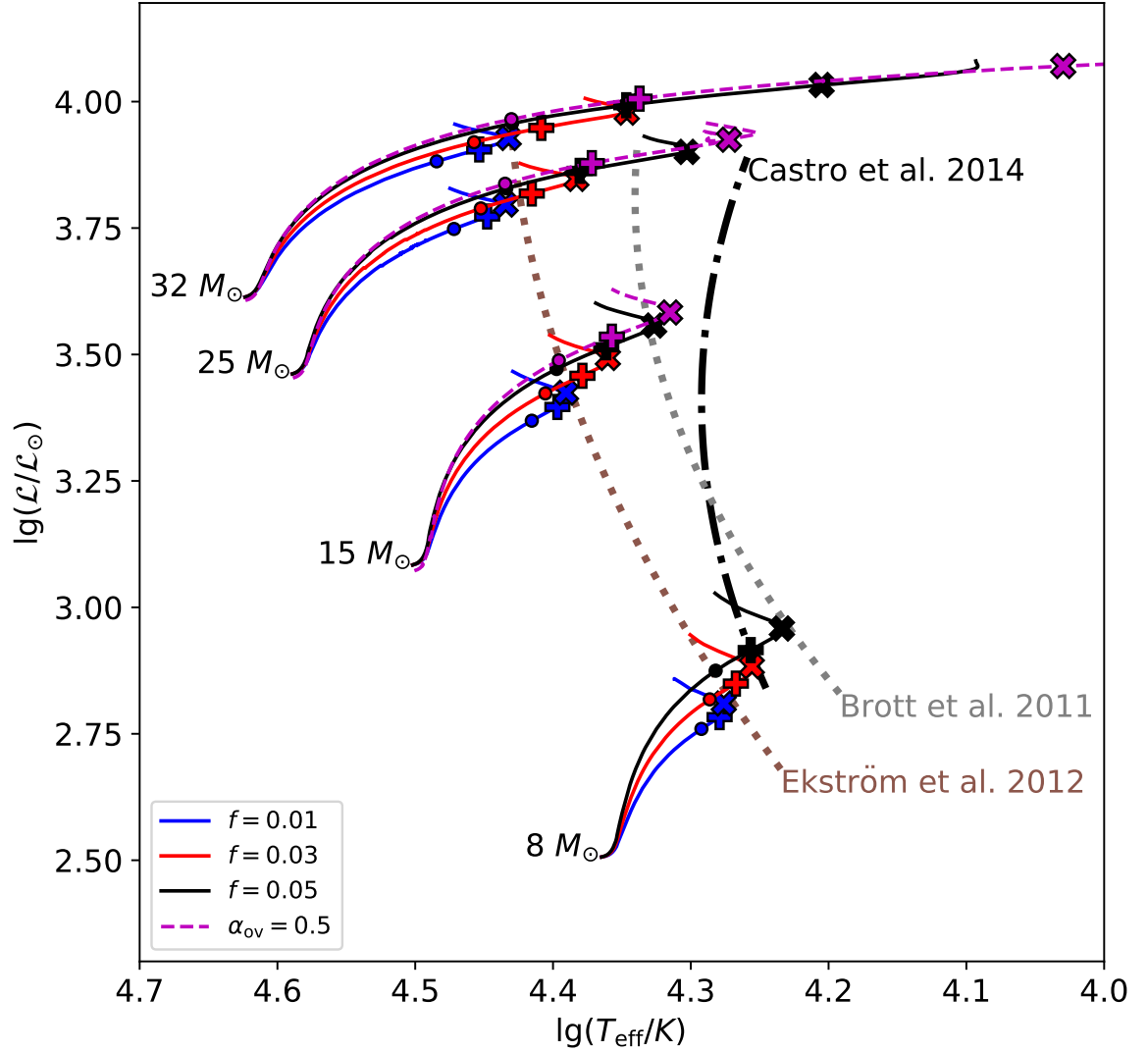


Figure 5.9: Spectroscopic Hertzsprung-Russell diagram of the shear model grid along with the step overshoot $\alpha_{\text{ov}} = 0.5$ models from Ch.4 for comparison. The dot, plus and cross symbols represent 90%, 95% and 99% of the MS lifetime respectively. Again, the TAMS of the model grids from Ekström et al. (2012) with $\alpha_{\text{ov}} = 0.1$ and Brott et al. (2011) with $\alpha_{\text{ov}} = 0.0335$ are plotted in the dotted lines, whereas the empirical TAMS of Castro et al. (2014) is plotted with the dot-dashed line.

The discrepancy between $\alpha_{ov} = 0.5$ and $f = 0.05$ becomes larger for the $32 M_{\odot}$, which has a very broad MS for these two cases. A similar trend was seen in Ch. 4, with the difference in MS width becoming much larger between CBM parameter values at this mass. However, the $32 M_{\odot}$ $f = 0.05$ shows the same very broad MS as the $\alpha_{ov} = 0.5$ model, reproducing the lack of an observable cool edge of the MS above $\sim 25 M_{\odot}$.

5.3 Carbon shell comparison of 3D and 1D models

In Secs. 5.1 and 5.2, both 3D carbon shell simulations and 1D MS models with shear CBM have been analysed in isolation. To compare the two, 1D models of the carbon shell phase will be analysed in this section. As in Sec. 5.2, these are non-rotating with metallicity $Z = 0.014$, but only $15 M_{\odot}$ models have been calculated since this is the mass used for the 3D simulations. Two values of the f parameter ($f = 0.05$ and 0.03) will be used in this section, since Fig. 5.9 suggests that $f = 0.05$ models are roughly consistent with the empirical TAMS from Castro et al. (2014), whilst $f = 0.03$ will be used as a comparison.

Rather than evolving models with $f = 0.05$ and $f = 0.03$ from the zero age MS to the carbon shell, these models were restarted from another model with no CBM. This is because differences in the size and position of convective regions can occur due to different amounts of CBM, and this difference accumulates over the evolution of the model. By using the model without CBM as a starting point, any differences in boundary shape due to the past evolution of the model are reduced, leaving only the mixing due to the shear CBM as a cause for differences in boundary shape.

The 3D simulations were initialised from a 1D model at a point where the carbon shell was growing in size (red bar in Fig. 5.1). The shear mixing models were started from the no-CBM model 500 time steps before this point, allowing the shape of the boundary to settle before they reach the equivalent point in the evolution of the carbon shell to the 3D simulations.

The carbon shell, unlike the main sequence hydrogen-burning core, also has a

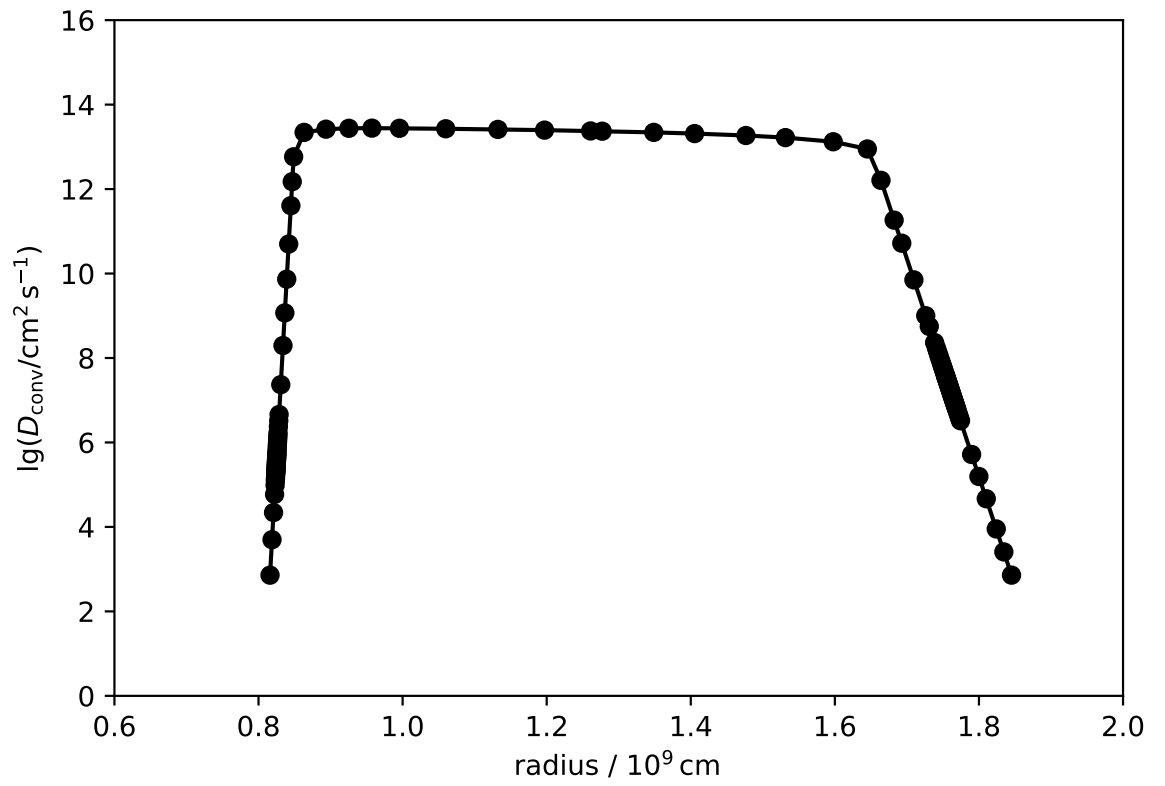


Figure 5.10: Profile of the diffusion coefficient D_{conv} in the second carbon shell for the 1D model with $f = 0.05$ and $f_{\text{u}} = 0.01$. Individual grid points are marked with dots.

lower convective boundary. Therefore, a value of f must also be chosen for this boundary as well. It was shown in Cristini et al. (2017) and Cristini et al. (2019) that the lower boundary of the carbon shell is roughly three times narrower than the upper due to its higher stiffness. Since this boundary width ratio is approximate anyway, I have used an f parameter for mixing underneath the shell, f_u , which is one fifth that of the upper boundary parameter in order to better see the effect of this difference in width.

Figure 5.10 shows a profile of $\lg(D_{\text{conv}})$ in the carbon shell for the $f = 0.05$, $f_u = 0.01$ 1D model. Note that unlike the MS models in Sec. 5.2, D_{conv} is not exactly flat in the formal convective region. This is because the time step in this evolutionary phase is much shorter than during the MS, so the upper limit for D_{conv} is higher than on the MS (refer to Sec. 3.2, Eq. 3.12 and surrounding text for an explanation of the limit on D_{conv}). The slope of the lower boundary is steeper than the upper boundary due to the fact that $f_u < f$. Thus, the width of the CBM region encompassed by the slope in D_{conv} is also smaller.

Figure 5.11 shows profiles of \bar{A} and its gradient for the $f = 0.05$ and $f = 0.03$ 1D models, along with the `eps1k` 3D simulation. Square markers representing $\bar{A}_{5\%}$ and $\bar{A}_{95\%}$ have been placed on each profile, as in Sec. 5.1, according to Eq. 5.2. As can be seen by the positions of the square boundary markers in the upper panels, the 3D simulation has significantly wider boundaries than the 1D cases. This is due to the nuclear reaction rate boosting which speeds up the convective flows. It was seen in Fig. 5.4 that increasing the boosting factor also increases the boundary width. However, the lower boundary is still narrower than the upper boundary in all cases.

The value of \bar{A}_{conv} also differs between the 1D models and the 3D simulation. It is likely that the carbon shell in the no-CBM model used as a basis for the shear CBM models does not occur in exactly the same conditions as the model used to initialise the 3D simulations. This leads to the difference in \bar{A} seen between the 1D profiles and the 3D simulation, despite the fact that the 1D profiles were taken at the same position relative to the start of the carbon shell as the 3D initial model.

Lastly, the lower panels of Fig. 5.11 show that the 1D models have mostly sym-

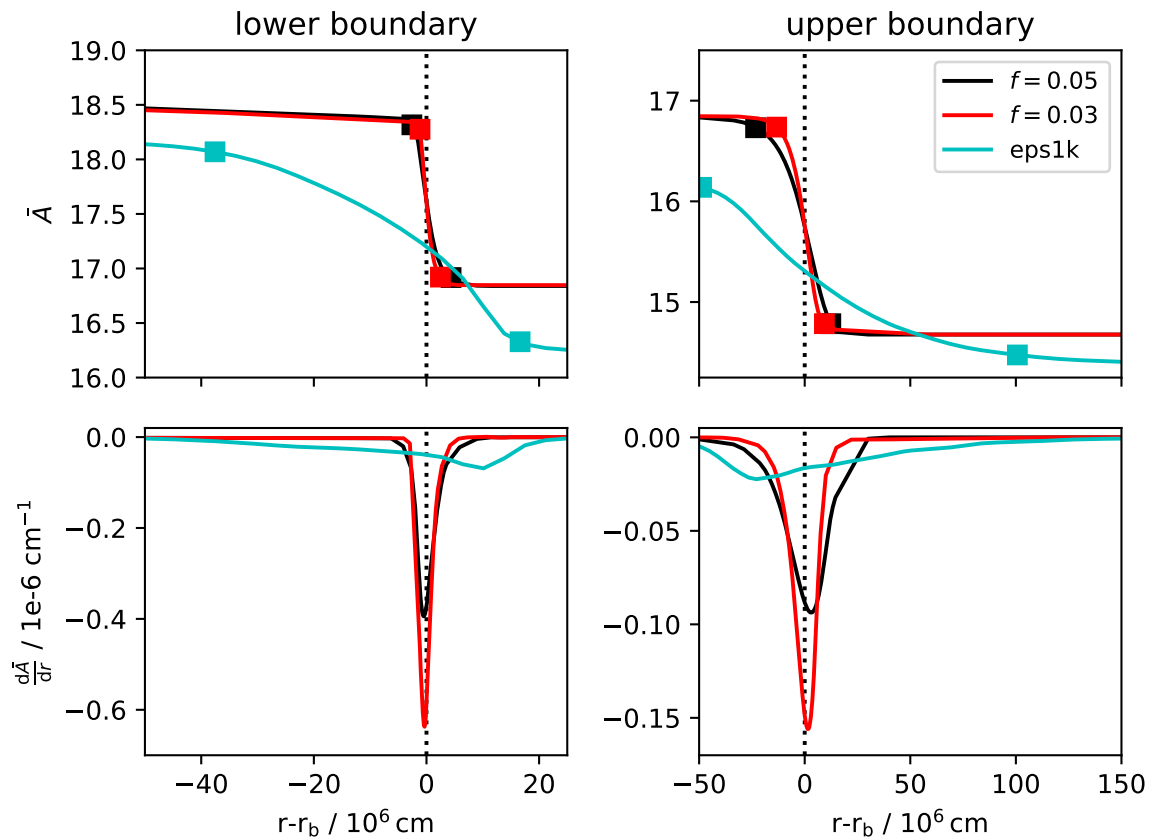


Figure 5.11: Profiles of mean atomic mass (\bar{A} , upper panels) and its spatial derivatives (lower panels) at the convective boundaries of the carbon shell. The markers in the upper panels represent 95% and 5% of the difference between the plateau values of \bar{A} either side of the boundary. The radius r_b (the 0 of the x -axis) is positioned at the 50% mark between the two plateau values. The models included are two 1D models with shear CBM ($f = 0.05$, $f = 0.03$) and the eps1k 3D simulation.

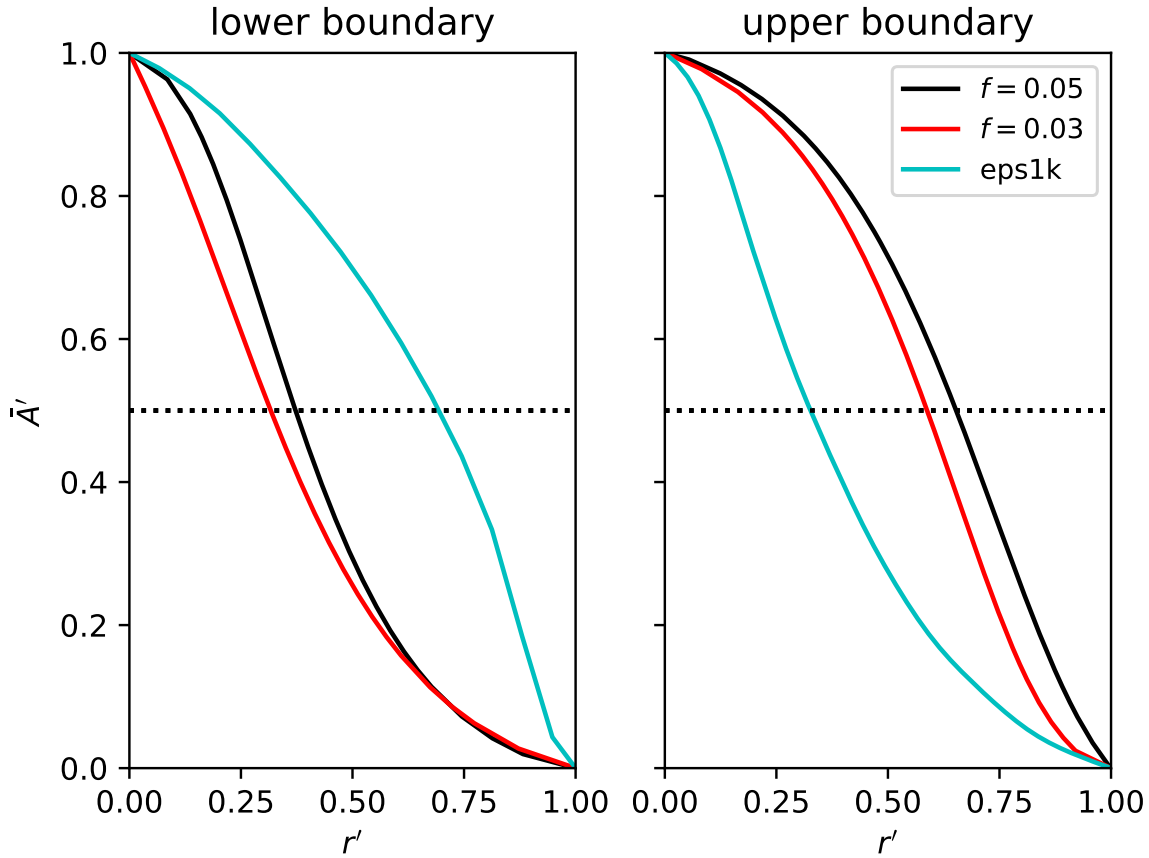


Figure 5.12: Comparison of boundary shape for two 1D shear models ($f = 0.05$, $f = 0.03$) and the `eps1k` 3D simulation. \bar{A} and the radius have been normalised such that they vary between 0 and 1 between the 5% and 95% boundary markers, according to Eqs.5.4. The centre of the boundary at which $\bar{A} = \bar{A}_{50\%}$ is marked with the dotted line at $\bar{A}' = 0.5$

metric boundaries with a sigmoid profile, where the slope of \bar{A} is steepest in the centre of the boundary at $r \sim r_b$. This contrasts the asymmetric boundaries of the `eps1k` simulation, in which \bar{A} changes quickest closer to to the convective region.

Since the boundaries of the 3D simulation are so much wider than the 1D models and the \bar{A}_{cinv} are different, it is useful to look at the normalised boundaries again, using the transformations given by Eq.5.4. This is shown in Fig. 5.12. Using normalised

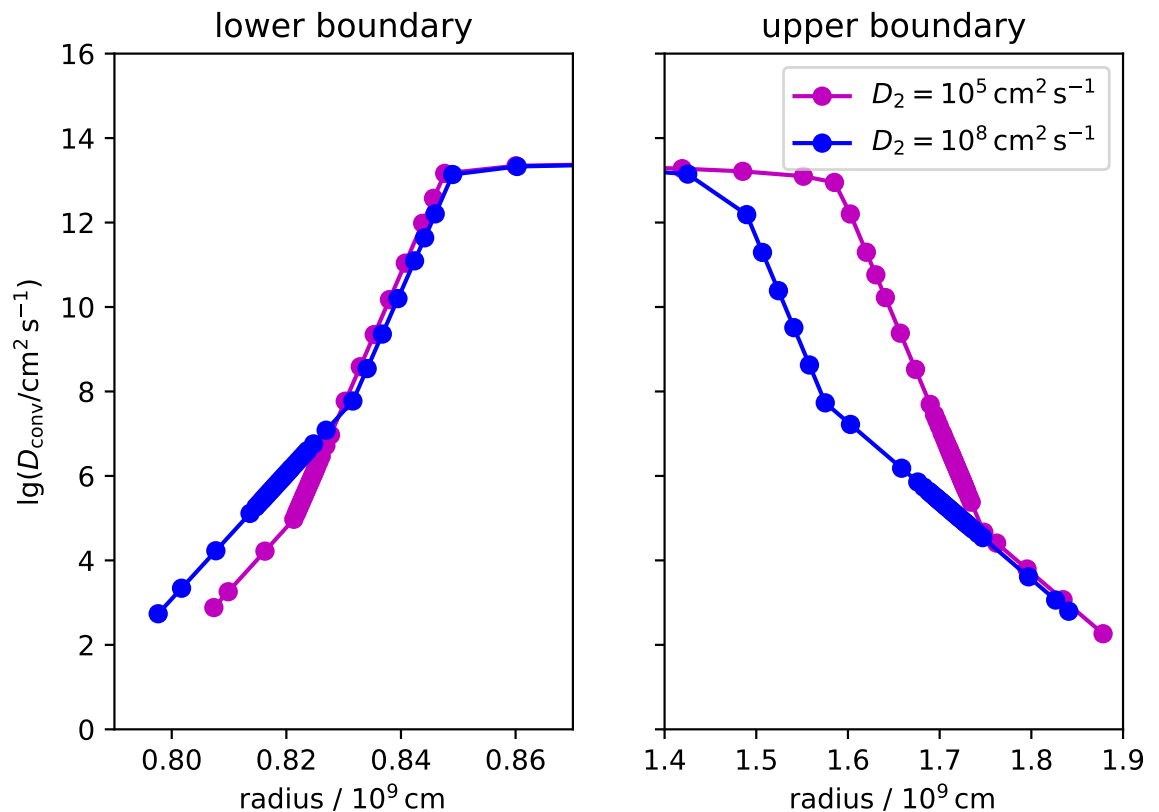


Figure 5.13: Lower and upper boundaries of the carbon shell for two double f models, both with $f = 0.05$, $f_2 = 0.14$, $f_u = 0.01$ and $f_{u,2} = 0.0208$. The models switch from f to f_2 at $D_{\text{conv}} = D_2$.

boundaries, there is little difference between the 1D $f = 0.05$ and $f = 0.03$ models, which both have a roughly sigmoid shape. In fact, the 1D boundaries appear similar to the 3D simulations with a higher boosting factor (e.g. the `eps10k` profiles in Fig. 5.6, which also have a roughly symmetrical sigmoid shape). Considering that the `eps1k` simulation is itself boosted, a non-boosted 3D simulation, which would be more representative of the boundaries in real stars if it could be computed for enough time steps, would be even further away from the 1D models in shape. Thus, these 1D models do not appear to reproduce the correct boundary shape expected from 3D simulations.

Since the shear CBM models with a single value of f per boundary do not fit the

eps1k simulation well, the next part of this section will deal with a 1D model in which the value of f increases to a higher value, f_2 , in the part of the CBM slope furthest from the convective region (double- f shear, see Sec. 3.3.2, Eq. 3.19). Figure. 5.13 shows the profiles of D_{conv} in the carbon shell for two models with $f = 0.05$ and $f_2 = 0.14$. These models were restarted from the no-CBM model in the same way as the single- f models previously and also have lower boundary values of f which are one fifth of those at the upper boundary ($f_u = 0.01$, $f_{u,2} = 0.0208$). The difference between the models is the value of D_{conv} at which the switch to the second slope happens, D_2 . The model with $D_2 = 10^5 \text{ cm}^2 \text{ s}^{-1}$ was based on Battino et al. (2016), who used this value of D_2 for the AGB phase. However, this value of D_2 was too low for the carbon shell phase and showed very little difference to the single- f $f = 0.05$ model. Therefore, only the $D_2 = 10^8 \text{ cm}^2 \text{ s}^{-1}$ model will be shown for the rest of this section.

Figure 5.14 shows the \bar{A} profiles and gradients of the single- f ($f = 0.05$), double- f ($D_2 = 10^8 \text{ cm}^2 \text{ s}^{-1}$) and **eps1k** models. The double- f model's boundaries are slightly wider than the single- f model's, but they are still much narrower than the 3D simulation boundaries. There is slight asymmetry on the upper boundary for the double- f model, since the $\bar{A}_{95\%}$ marker is slightly further out from the boundary centre than the $\bar{A}_{5\%}$ marker. However, the gradients in the lower panels do not show much asymmetry, with the highest magnitude of the gradient occurring at $r \sim r_b$, similarly to the single- f model. The peak of the gradient is flattened compared to the single- f model as a result of the broader boundary.

The normalised boundaries for the single- f , double- f and **eps1k** models are shown in Fig. 5.15. In this figure the double- f model appears very similar to the single- f model for the lower boundary, having a similar shape to the 3D simulations with higher boosting factors. The upper boundary shows different behaviour, with the double- f model intermediate between the 3D and single- f profiles. This is also visible in Fig. 5.14, where the boundary markers for both 1D models appear to be roughly equidistant from the lower boundary centre, whilst the 95% marker on the upper boundary is further away than the 5% marker for the double- f model. This is more similar to the 3D model, for which the 5% markers are also closer to the boundary

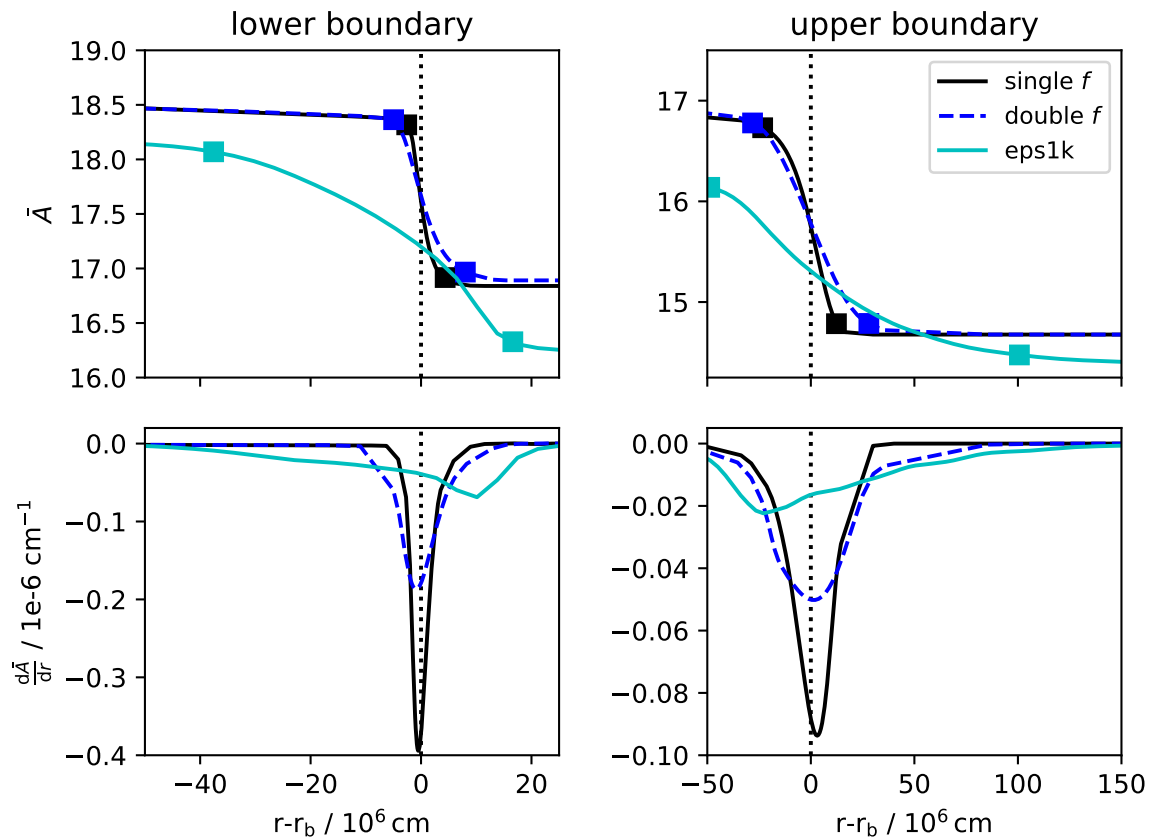


Figure 5.14: Profiles of mean atomic mass (\bar{A} , upper panels) and its spatial derivatives (lower panels) at the convective boundaries of the carbon shell. The markers in the upper panels represent 95% and 5% of the difference between the plateau values of \bar{A} either side of the boundary. The radius r_b (the 0 of the x -axis) is positioned at the 50% mark between the two plateau values. The models included are two 1D models with shear CBM (single- f and double- f) and the eps1k 3D simulation.

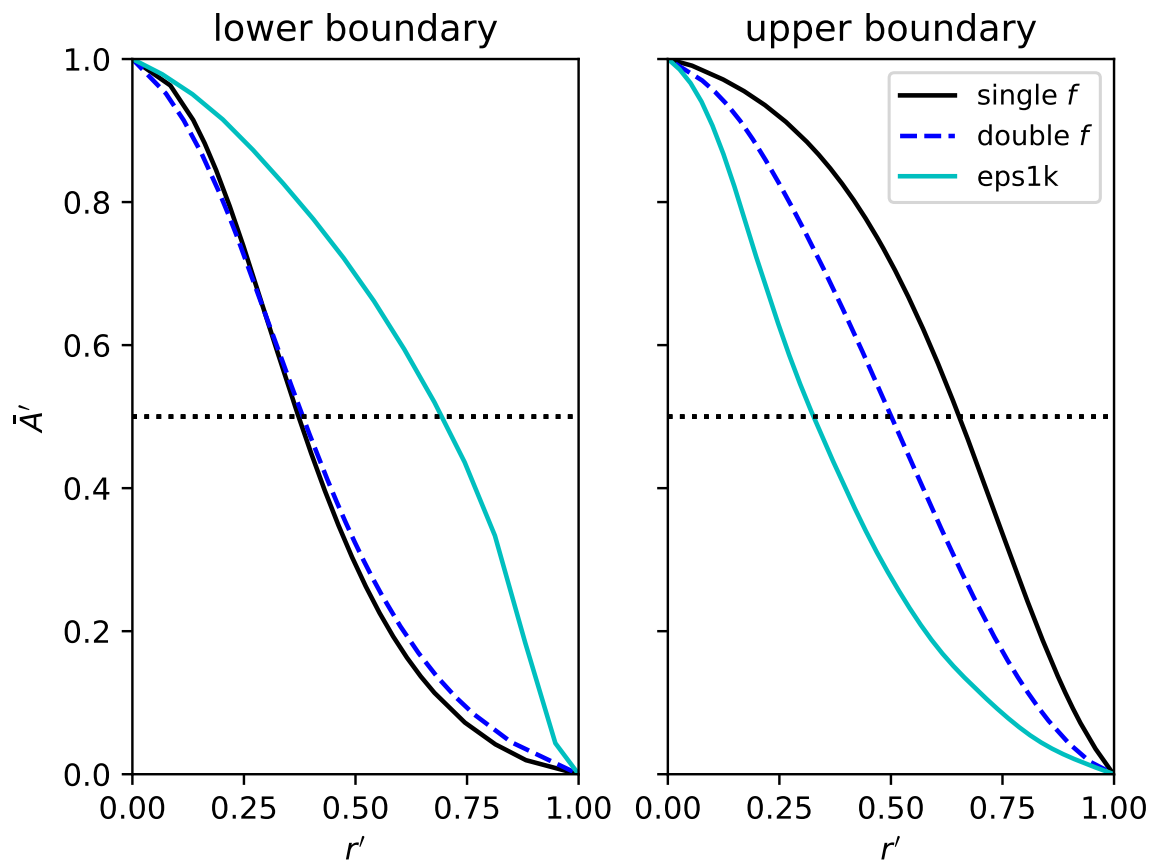


Figure 5.15: Comparison of boundary shape for two 1D shear models (single- f and double- f) and the eps1k 3D simulation. \bar{A} and the radius have been normalised such that they vary between 0 and 1 between the 5% and 95% boundary markers, according to Eqs.5.4. The centre of the boundary at which $\bar{A} = \bar{A}_{50\%}$ is marked with the dotted line at $\bar{A}' = 0.5$

centre than the 95% markers. It is possible that the difference in behaviour between the upper and lower boundaries in the 1D models may be due to the definition of \bar{A}_{stable} in the lower stable region. Unlike in the 3D simulations, the 1D models have a slight gradient in \bar{A} in the lower stable region, thus \bar{A}_{stable} was defined using a single grid point rather than an average over several grid points (as was used in all other cases). Alternatively, the gradient of D_{conv} may be too steep for the lower boundary for the double- f mixing to make an appreciable difference, perhaps because the choice to take $f_{\text{u},2} = \frac{1}{5}f_2$ was flawed (this will be discussed in Ch. 6). It is likely that the upper boundary is therefore more useful for seeing the effects of different mixing schemes.

By comparing Figs. 5.12 and 5.15, it appears that the double- f shear CBM scheme may provide a way to reach a boundary shape more similar to the 3D simulations. However, it is possible that the values of the parameters needed is different to those used in this chapter, which may provide a source of error in this analysis. Furthermore, since there is not yet an adequately developed 3D simulation of carbon burning using a natural reaction rate, these results can only provide trends towards the correct prescription.

6 Discussion

In this chapter, the results from the previous two chapters will be discussed. The main sequence entrainment models will be discussed in Sec. 6.1, whereas the shear models will be discussed in Sec. 6.2. Finally, further implications of these results and how they may apply to a more general model of convective boundaries will be discussed in Sec. 6.3.

6.1 Entrainment

Chapter 4 presented a grid of 1D stellar models with masses between 1.5 and $60 M_{\odot}$ and at solar metallicity ($Z = 0.014$). The boundary penetrability by convective flows, quantified by the bulk Richardson number Ri_B , decreases monotonically with increasing mass. This decrease is dominated by the increase in typical convective velocities due to the steep mass-luminosity relation for stars in the 1 to $20 M_{\odot}$ range. The boundary stiffness, $l_c \Delta b$, is nearly invariant with mass in the range studied.

Due to the decrease in Ri_B with mass, models with entrainment experience a mass-dependent increase in mixing. This is reflected in a corresponding mass-dependent MS widening in the HRD. In these models, the value of A which best reproduces the observed MS widths of massive stars is $A = 2 \times 10^{-4}$, with $n = 1$. However, more extended observational samples are desired to place a very tight constraint on A and the effects of rotation were not considered in this work (Martinet et al. 2021).

The choice of temperature gradient in the entrained region is also an important factor in the implementation of entrainment. As explained in Sec. 4.1.1, the temperature gradient is set to ∇_{ad} in the entrained region, since 3D simulations show that entropy is well mixed as the convective region grows (Cristini et al. 2017). 3D simulations also show a narrow boundary above the entrained region with a smooth chemical gradient rather than a switch from one μ to another; it is likely that the mixing of entropy is similarly slowed compared to the entrained region in this boundary. Indeed,

asteroseismic observations support MS convective cores with a smooth ∇ profile in the CBM region (e. g. Arnett & Moravveji 2017).

In standard models, the global evolutionary effect of a slight change in ∇ in the CBM region is subtle, especially if the CBM region is small. In entrainment models, however, the size of the CBM region towards the end of the MS can be significant, especially with larger values of A . The choice of ∇ may also have a more important role in entrainment models due to its effect on the buoyancy jump, Δb . In our current implementation, the CBM region has no contribution to Δb whatsoever, since it is fully mixed ($\nabla_\mu = 0$) and $\nabla = \nabla_{\text{ad}}$. This means that the buoyancy frequency in the entrained region is 0. If the temperature gradient were to instead transition smoothly from ∇_{ad} to ∇_{rad} within the entrained region (as explored in Michielsen et al. 2019), there would be a contribution to Δb from the entrained region. This contribution would grow larger as the entrained region grows in size, therefore providing more feedback slowing the entrainment for larger values of A . Consequently, these models would require larger values of A than models with $\nabla = \nabla_{\text{ad}}$ to produce the same MS width.

Since Sec. 4.2.2 demonstrates that the mass dependence of Ri_B is dominated by the change in typical convective velocities with mass, it is interesting to test whether a scaling based on v_c could provide a simpler alternative to entrainment. This seems reasonable since the dependence of Ri_B with mass is almost entirely controlled by v_c , with $l_c \Delta b$ staying nearly constant with mass (for convective cores on the MS - other convective regions may behave differently). To constrain this scaling, a value of $\alpha_{\text{ov}} = 0.5$ is used for $15 M_\odot$, as this most closely matches the Castro et al. (2014) observational $\lg(T_{\text{eff,min}}) \sim 4.3$. The scaled overshoot parameter for each mass, M_{ini} , is then given by

$$\alpha_{\text{ov,scaled}}(M_{\text{ini}}) = \alpha_{15 M_\odot} \frac{\langle v^m(M_{\text{ini}}) \rangle}{\langle v^m(M_{\text{ini}} = 15 M_\odot) \rangle}, \quad (6.1)$$

where $\alpha_{15 M_\odot} = 0.5$ and $\langle v^m(M_{\text{ini}}) \rangle$ is the average of the convective velocity to the power m over the MS of the model of initial mass M_{ini} .

Various scenarios support different values for m . According to Eq. 4.1, the mass entrainment rate \dot{M}_{ent} is proportional to v_c^3 . If α_{ov} in the step overshoot case most

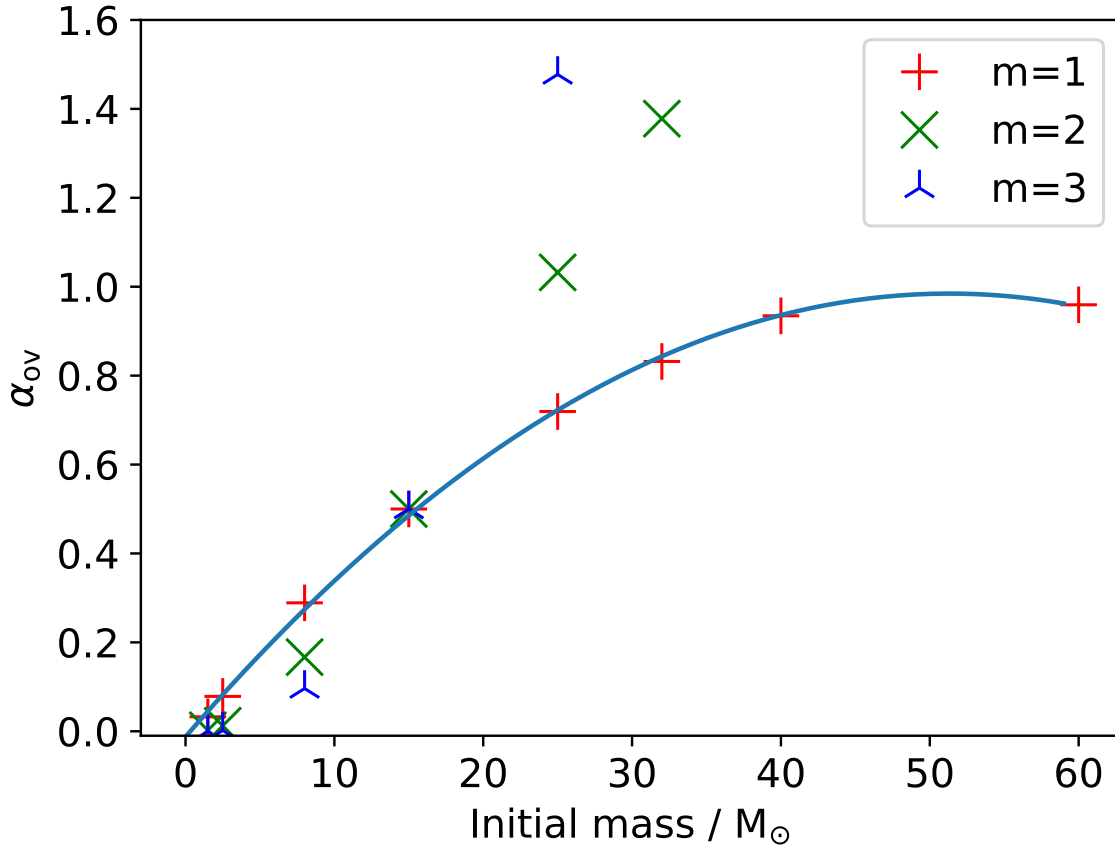


Figure 6.1: Step overshoot parameter α_{ov} scaled using Eq. 6.1. The polynomial fit to the $m = 1$ points uses the equation $\alpha_{ov}(M_{ini}) = -0.00037867M_{ini}^2 + 0.03885918M_{ini} - 0.01237484$. Previous studies such as Claret & Torres (2017) and Moravveji et al. (2016) show that similar results are obtained using an exp-D f parameter which is roughly a factor of 10 to 15 smaller than the equivalent step overshoot α_{ov} . Therefore a fit for $f(M_{ini})$ would be roughly 1/10 to 1/15 of $\alpha_{ov}(M_{ini})$, M_{ini} in solar masses.

closely corresponds to \dot{M}_{ent} in entrainment models, then $m = 3$ is appropriate. However, $m = 2$ would be supported if α_{ov} corresponds best to the penetrability of the boundary (Ri_B is inversely proportional to v_c^2 if $n = 1$). The $m = 1$ case of $\alpha_{ov} \propto v_c$ would be similar to the findings of Denissenkov et al. (2019), who reported that the exp-D f parameter scales linearly with the cubic root of the convective driving luminosity, or equivalently $f \propto v_c$.

Figure 6.1 shows the predicted values of α_{ov} according to Eq. 6.1 with $m = 1, 2$ and 3. The $m = 2$ and $m = 3$ cases quickly reach very high and unrealistic values of α_{ov} above $15 M_{\odot}$; thus the y-axis scale is zoomed onto the lower α_{ov} range. The values of $\alpha_{\text{ov}} = 0.05$ and $\alpha_{\text{ov}} = 0.1$ for $1.5 M_{\odot}$ and $2.5 M_{\odot}$ respectively have already been calibrated (Ekström et al. 2012). These values are underestimated by the $m = 2$ and $m = 3$ cases. Only $m = 1$ matches the already-known values for the lower mass range and does not produce extremely high values in the higher mass range.

Since the $m = 1$ case seems the most reasonable, we have provided a polynomial fit to this scaling, described in the caption of Fig. 6.1. We emphasise that this scaling should only be considered a temporary fix to the problem of mass-dependent CBM and behaviour of the mass range above $60 M_{\odot}$ is unknown. Whilst the $m = 1$ scaling supports previous findings (Denissenkov et al. 2019), the step overshoot values at $M_{\text{ini}} \geq 30 M_{\odot}$ are already much larger than the value of $\alpha_{\text{ov}} = 0.5$ favoured by Higgins & Vink (2019). Furthermore, Eq. 6.1 also does not take the stiffness of the boundary into account. This may be less of a problem for MS cores, but convective shells which have two boundaries are known to have different stiffnesses for each and different entrainment rates according to the entrainment law (Cristini et al. 2019). In addition, the possible mass dependence of $H_{P,b}$ (which is used to determine the total overshooting distance, $d_{\text{ov}} = \alpha_{\text{ov}} H_{P,b}$) should not be discounted, as it also contains information on the stellar structure near the boundary.

Nevertheless, an additional model at $25 M_{\odot}$ with $\alpha_{\text{ov}} = 0.7$ has been calculated, which is approximately the value suggested by the $m = 1$ case of Eq. 6.1. This model can be found in Table 4.1 and in Figs. 4.5, 4.7 and 4.8 represented by a black clover symbol. Fig. 4.5 in particular shows that this model produces a very broad MS with a minimum $\lg T_{\text{eff}} \sim 4$, which is consistent with Castro et al. (2014).

The focus of this study is on entrainment at the convective core boundary during the MS, but many 3D simulations which resulted in entrainment were concerned with later evolutionary phases. The effects of entrainment in post-MS 1D models are unknown, but may be similar to that of other CBM with phenomena such as increased likelihood of convective shell mergers. In convective envelopes, the length-scales and

pressure stratification can be significantly increased compared to convective cores (e. g. Pratt et al. 2020). The relatively high importance of thermal diffusion may mean that entrainment is not a suitable CBM prescription in convective envelopes (Viallet et al. 2015).

Since this entrainment implementation is cumulative, it is interesting to compare the results of Ch. 4 to those of Staritsin (2013), who used instantaneous entrainment. Staritsin’s values for A were also much smaller than the results of 3D simulations, with $A = 4.425 \times 10^{-4}$ for the $16 M_{\odot}$ model and $A = 4.054 \times 10^{-4}$ for the $24 M_{\odot}$. This is not dissimilar to our value of 2×10^{-4} , perhaps due to the similarity in calibration: Staritsin required that the entrained distance at the ZAMS was $0.1 H_P$, guided by asteroseismic results for the star HD 46202 (Briquet et al. 2011). We also based our initial estimate of $A = 10^{-4}$ on the MS lifetime of models with $\alpha_{\text{ov}} = 0.1$, as explained in Sec. 4.2.3.

However, there are also significant differences between the cumulative entrainment models and the models of Staritsin (2013). The key result of Staritsin (2013) was an entrainment region which decreased with time as the model evolved; the opposite is true for the cumulative models, since the mass of the entrained region can only ever increase (by construction). As such, Staritsin’s entrainment models produced less helium overall than standard $\alpha_{\text{ov}} = 0.1$ models, whereas the cumulative entrainment estimations for helium core sizes were much greater (see Table 4.1). In addition, the buoyancy jump continuously increases in Staritsin (2013), whereas in Ch. 4, the buoyancy jump plateaus near the middle of the MS (as explained in Sec. 4.2.1). This difference could be due to the buoyancy jump integration distance used by Staritsin, $h \sim 2v_c/N$. Since v_c grows with time during the MS (in Staritsin’s models as well as ours), the integration length h would similarly increase with time, potentially leading to the increase in Δb .

To conclude, the entrainment law, through its dependence on the bulk Richardson number, produces models with a wider MS for high mass stars than standard models. In addition, the extension of the MS increases with mass, as required by observation. However, the value of the entrainment law A parameter required to produce the correct MS width for the lower mass stars in our grid is orders of magnitude smaller than the

value derived from 3D simulations of convection in the later stages of stellar evolution. This value may change further if more aspects of convective boundary physics are included, such as shear. Although these models are not complete, they are an important step in the right direction since they show that convective boundary penetrability is a key part of the physics behind the mass dependence of CBM.

6.2 Shear

6.2.1 Behaviour of the 1D shear models compared to other CBM types

Figures 6.2 to 6.4 compare the values for the minimum MS effective temperature, MS lifetime and helium core mass at the end of the MS ($T_{\text{eff,min}}$, τ_{MS} and M_{He}) for the step overshoot, entrainment and shear models in the 8 to $32 M_{\odot}$ range. The plotted values are taken from Tab. 4.1 for the step overshoot and entrainment models, whilst Tab. 5.1 shows the shear model values. For the shear models, the column $M_{\text{He},1\%}$ has been chosen as the most suitable estimate of M_{He} for the reasons described in Sec. 5.2.

Beginning with the effective temperature, the rough scaling between step overshoot and shear CBM ($\alpha_{\text{ov}} \sim 10f$) was confirmed in Ch. 5 using the widths of evolutionary tracks on an sHRD. Figure 6.2 shows a more detailed view of how the shear models compare to the step overshoot (and entrainment) models by looking at the temperature of the cool edge of the MS. The empirical location of this cool edge, according to Castro et al. (2014), is $\lg(T_{\text{eff}}) \sim 4.25$ for 8 and $25 M_{\odot}$, or ~ 4.3 for $15 M_{\odot}$. The MS becomes very broad at $32 M_{\odot}$ such that the width is not as well constrained by the data, but $\lg(T_{\text{eff}})$ should be well below 4.25 at the TAMS. These numbers for the TAMS give some idea of what parameter values would be appropriate at different masses.

The $f = 0.01$ and $\alpha_{\text{ov}} = 0.1$ models in Fig. 6.2 correspond very well, but the $f = 0.05$ and $\alpha_{\text{ov}} = 0.5$ models are less similar. The fact that the relation $\alpha_{\text{ov}} \sim 10f$ becomes less accurate for larger parameters is simply a result of the larger mixing

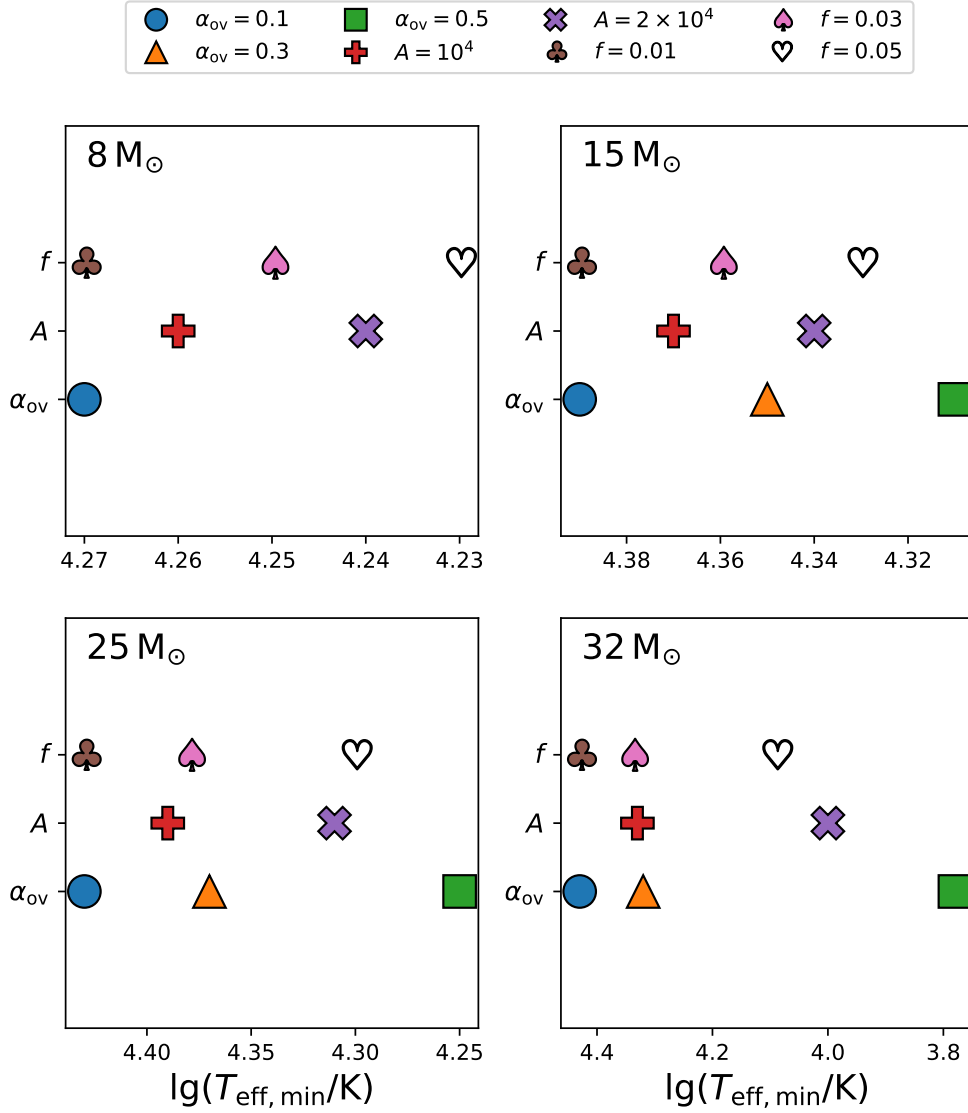


Figure 6.2: Minimum main sequence effective temperature for step overshoot, entrainment and shear models. Each sub-figure corresponds to a different mass, whilst markers designating CBM parameter value are grouped on the y axis according to CBM type.

regions amplifying the error in the relation. This approximate relation is taken from several studies which have fitted a value of $f \lesssim 0.25$ (e. g. $f = 0.016$ for Herwig (2000), $f = 0.024$ for Moravveji et al. (2016) and $f \lesssim 0.02$ for Claret & Torres (2017)) and it is possible that a different relationship would be appropriate for more massive stars. Since there appears to be mass dependence in entrainment mixing, attempting to find a linear relationship between A and the other CBM parameters would not be useful, but the mass dependence of the entrainment scheme may be captured using the convective velocity, as in Eq. 6.1.

The main sequence lifetime, τ_{MS} , is shown for the 8 to $32 M_{\odot}$ models in Fig. 6.3. Here it is interesting to note that whilst the $f = 0.01$ and $\alpha_{\text{ov}} = 0.1$ models were very similar in effective temperature at the TAMS, the MS lifetime differs, particularly for the 15 and $25 M_{\odot}$. Since τ_{MS} is closer for these parameters at both 8 and $32 M_{\odot}$, there does not appear to be a linear divergence with mass. It is perhaps significant that the $f = 0.01$ model has the shortest lifetime for all masses, since this could be an effect of the partial mixing used in the shear CBM prescription. For stars with a convective core, the MS ends when the core depletes its hydrogen. In a model with additional instantaneously mixed CBM (e. g. step overshoot, entrainment), then the hydrogen available at the end of the MS includes that contained in the CBM region. This is not the case for the partially mixed region in the shear models, since the diffusion coefficient quickly drops to a level too low to mix hydrogen into the formal convective core at the end of the MS. Since the luminosity remains roughly the same between equivalent shear and step overshoot models (seen in Fig. 5.9), the main difference in MS lifetime comes from the difference in the size of the fully mixed region. The difference in lifetime between shear and penetrative overshoot models would likely still appear in models with diffusive convection, since the diffusion timescales on the MS are still much shorter than the evolutionary timescales, leading to convection which is still approximately instantaneous.

The last comparison of the tabulated quantities from Tabs. 4.1 and 5.1 is the helium core mass, M_{He} , shown in Fig. 6.4. The quantity taken as M_{He} for the diffusive models is in the last column of Tab. 5.1, $M_{\text{He},1\%}$. Similarly to the step overshoot models

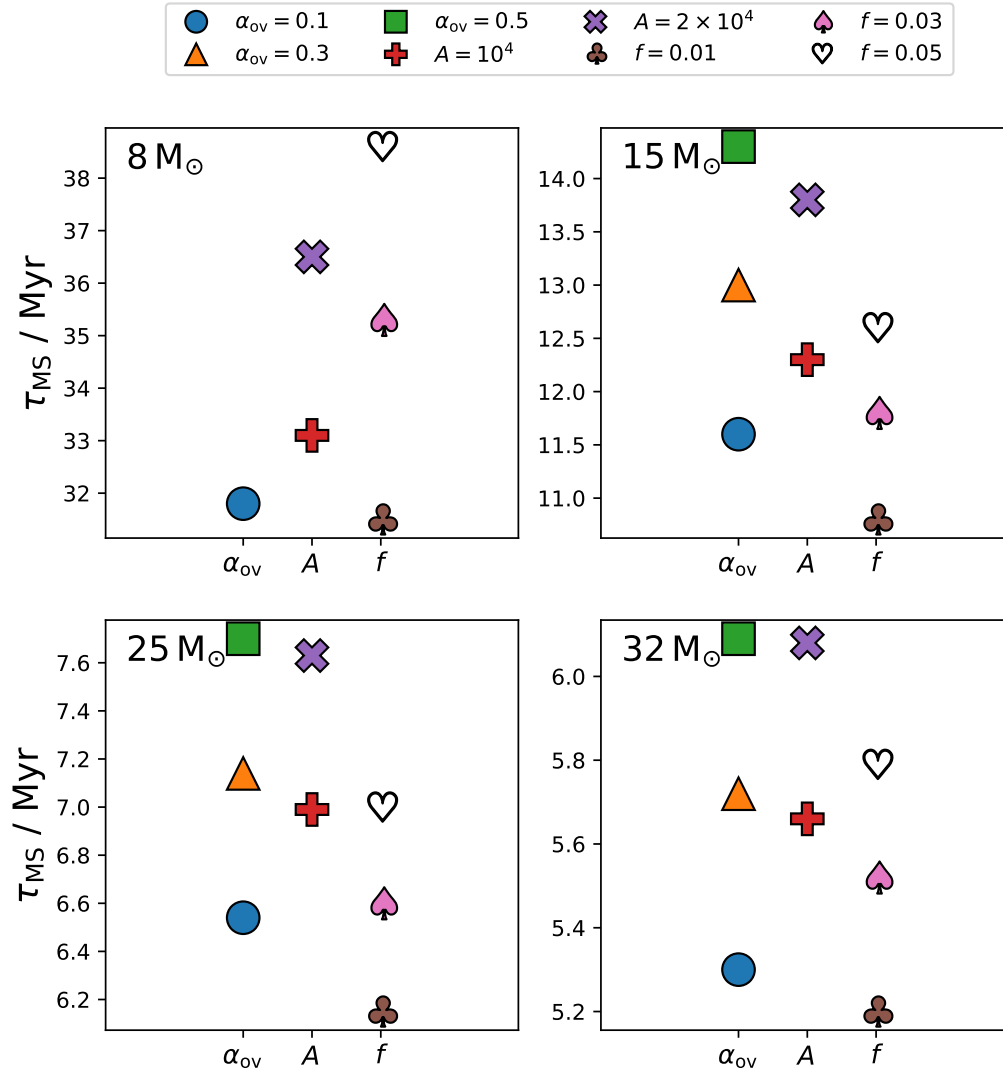


Figure 6.3: Main sequence lifetime for step overshoot, entrainment and shear models. Each sub-figure corresponds to a different mass, whilst markers designating CBM parameter value are grouped on the x axis according to CBM type.

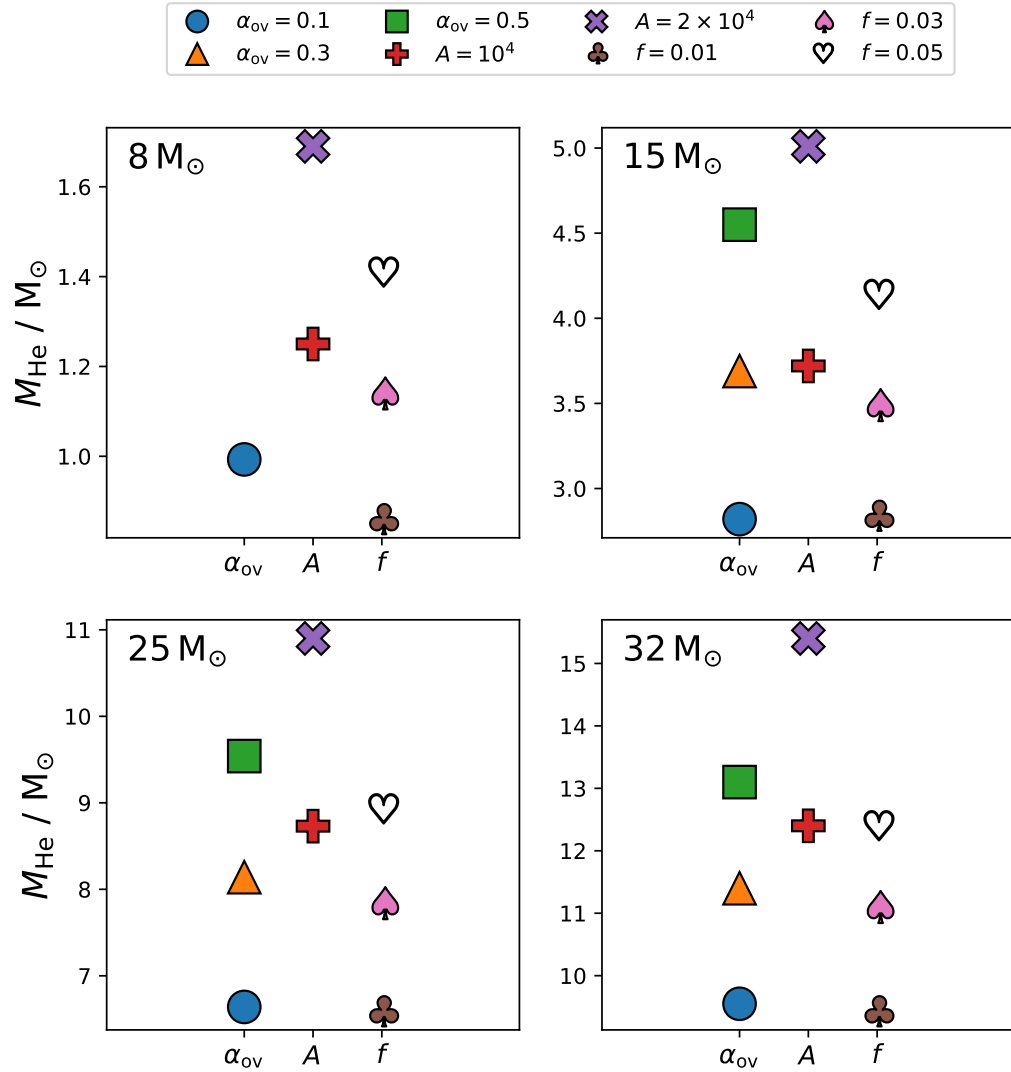


Figure 6.4: Helium core mass, M_{He} , at the end of the main sequence for step overshoot, entrainment and shear models. The definition of M_{He} used for the shear models is $M_{\text{He},1\%}$ (see Sec. 5.2). Each sub-figure corresponds to a different mass, whilst markers designating CBM parameter value are grouped on the x axis according to CBM type.

in Ch. 4, the diffusive models have generally smaller cores than the entrainment models. As with $T_{\text{eff,min}}$, the step overshoot and diffusive models appear fairly similar for low α_{ov} or f , apart from the $8 M_{\odot}$ models. In fact, the effect of increasing mixing strength for all mixing types is similar for all masses (the distribution of markers on each sub-figure looks similar, despite the y -axis scale changing). Comparing the diffusive models to the entrainment models shows a slight exception, since the $A = 10^{-4}$ models are closest to $f = 0.03$ for 8 and $15 M_{\odot}$, whereas $f = 0.05$ is a better match at 25 and $32 M_{\odot}$. Helium core mass is mainly a measure of the size of the mixed region at the end of the MS; it makes sense therefore that adding a fixed distance of mixing increases the core by roughly the same percentage for all the masses. The fact that the amount of entrainment at the end of the MS depends on the boundary stiffness throughout the previous evolution explains why it does not remain as similar with mass as the other two mixing types, since convective velocities increase as the mass increases.

The comparison of the various CBM types has shown that in terms of the three quantities shown in Figs. 6.2 to 6.4, there are similarities in the effect of increasing f and increasing α_{ov} ; in particular, models with $f = 0.01$ and $\alpha_{\text{ov}} = 0.1$ have similar $T_{\text{eff,min}}$ and M_{He} for almost all cases shown. Since the extent of both step overshoot and diffusive CBM depends on the pressure scale height, a linear conversion between them should be able to reproduce similar helium core masses (since M_{He} is simply a measure of core size as explained previously). However, the conversion $\alpha_{\text{ov}} = 10f$ used to choose the f parameter values in Ch. 5 is not exact, as proven by the departure in values as α_{ov} and f increase. A linear conversion between α_{ov} and f seems to also hold for $T_{\text{eff,min}}$, even if the effect of increasing CBM is not as direct as for M_{He} ; the proportional reduction in $T_{\text{eff,min}}$ with increasing CBM parameter appears similar for both α_{ov} and f , even if the absolute reduction is different. The main outstanding feature of the diffusive models in the previous figures is the MS lifetime, which is less affected by diffusive CBM than by the other mixing types. In this case, a different conversion between α_{ov} and f could produce similar values for τ_{MS} , since the proportional effect of increasing CBM does seem similar for both cases, although the usefulness of this would be limited since τ_{MS} is not a directly observable quantity, unlike $T_{\text{eff,min}}$. However, it is

still important to note that it does not appear to be possible for models with diffusive CBM on the core to match step overshoot models in both MS width and lifetime.

6.2.2 Mechanism of mixing at the boundary

In Sec. 5.3, there were two key results from comparing 3D and 1D models of carbon burning. Firstly the 3D models showed that the boundary is composed of two main sections. These are the strongly mixed region (closest to the convective region) and the weakly mixed region (further away from the convective region). The size of the two regions varies with boosting factor. Secondly, the standard single- f CBM was not able to model the boundary shape seen in the 3D simulations. However, a double- f prescription, which splits the mixed region into two sections with different slopes, was a closer match to the upper boundary of the least boosted 3D simulation.

Starting with the boundary shape in the 3D simulations, the presence of the strongly and weakly mixed regions became apparent when comparing the simulations with different boosting factors. The effect of the boosting factor is to multiply the nuclear reaction rate, such that the 1000 times boosted simulation has a reaction rate which is 1000 times larger than that expected in a real star. The theoretical effect of the boosting factor ϵ on the convective velocity v_c is $v_c \propto \epsilon^{1/3}$, which is satisfied by the simulations (Fig. 7 in Cristini et al. 2019). The size of the strongly mixed region, in which the chemical abundances do not change much with radius, grows larger for larger boosting factors (larger convective velocities). In contrast, the weakly mixed region remains similar in size for all of the boosting factors from 1000 to 33×10^4 .

The fact that one part of the boundary grows as the convective velocity grows whilst the other does not suggests that the two parts of the boundary are created by different processes; one process depends on the convective velocity whilst the other does not (or only depends weakly on the convective velocity). Shear is one possible process that may be responsible for the strongly mixed region. In the diffusive approximation, the strength of shear mixing is directly proportional to velocity (Maeder & Meynet 1996). If velocities are sufficiently high, shear will cause Kelvin-Helmholtz instabil-

ities at the convective border, contributing to significant mixing. Kelvin-Helmholtz instabilities are known to appear in 3D simulations of convection (Herwig et al. 2014; Woodward, Herwig & Lin 2015) and are also proposed to be the mechanism by which entrainment occurs (Meakin & Arnett 2007).

In the 2D simulations of Freytag, Ludwig & Steffen (1996), the origin of the exponentially-decaying velocities at the convective boundary was explained through strong, narrow plumes penetrating the stable layer. However, these simulations were of envelope convection, for which diffusive processes play a significant part. In this regime (low Péclet number), plumes are not decelerated as strongly as in the interior and so can contribute greatly to mixing. When diffusive processes are mostly negligible, as in the interior, braking outside the formal convective region is stronger and the mixing processes at the boundary are different than in envelope convection. The plumes do not penetrate the stable layer, instead deforming the boundary before returning into the convective region.

The deformation of the boundary may still complicate the interpretation of the boundary shapes seen in Ch. 5. Apart from Fig. 5.3, the 3D simulation profiles shown are all horizontally averaged. Thus, any vertical deformation of the boundary may contribute to the apparent shape of the boundary. However, it is clear from the differences in individual non-averaged profiles in Fig. 5.3 that averaging over a deformed boundary does not account for all of the apparent strongly mixed region.

The second part of the boundary, the weakly mixed region, does not change significantly with boosting factor and is therefore most likely due to a mixing process which does not depend as strongly on convective velocity. One process seen in 2D and 3D simulations is mixing by internal gravity waves (IGW). These waves were interpreted by Battino et al. (2016) (in the first paper using double- f CBM) as the cause of the second slope in mixing seen in the 2D convection simulations of Herwig et al. (2007). IGW are excited by both convective plumes and eddies (Rogers et al. 2013) and have been proposed as affecting processes such as lithium depletion (Garcia Lopez & Spruit 1991) and the formation of the carbon-13 pocket (Denissenkov & Tout 2003). The degree of mixing due to these waves is non-linear with velocity,

since an entire spectrum of waves is produced by convective motions at the boundary. Therefore, it is difficult to say whether IGW are compatible with the weak velocity scaling suggested by the 3D simulation boundary profiles in Ch. 5. Rogers et al. (2013) find that the highest amplitude IGW are generated by plumes rather than eddies, so the absences of plumes in the Cristini et al. (2019) simulations may mean that any IGW are weakly generated by eddies at the boundary, providing little mixing. In this case, the velocity scaling of the mixing would not be as obvious as for stronger mixing.

If the mechanism behind the weakly mixed region is indeed IGW, then the choice to reduce the f value for the second slope at the lower boundary may have been an error, since the mixing due to IGW is not known to depend on the boundary stiffness. The small value of f for the lower boundary may have contributed to the fact that the double- f model did not show any difference from single- f , since the size of the second mixed region had been reduced.

To summarise, the boundary shapes of the 3D simulations of Cristini et al. (2019) are characterised by two mixing regions: a strongly mixed region near the convective zone and a weakly mixed region beyond. I suggest the strongly mixed region is dominated by convective shear and Kelvin-Helmholtz instabilities which become more powerful with increased convective velocity, whilst the weakly mixed region is dominated by internal gravity waves excited by the convective eddies at the boundary. The double- f CBM prescription can approximate this structure, but is sensitive to the parameter values used and is lacking an adequate non-boosted carbon shell simulation for comparison. A non-boosted simulation for the neon shell will be part of the upcoming simulations of Georgy et al. (in prep.), which will also be valuable to compare with the double- f models.

6.3 Modelling the multi-layered boundary

The two features of 3D models addressed by Chs. 4 and 5 are the progression of the boundary with time (entrainment) and the smooth boundary shape created by partial

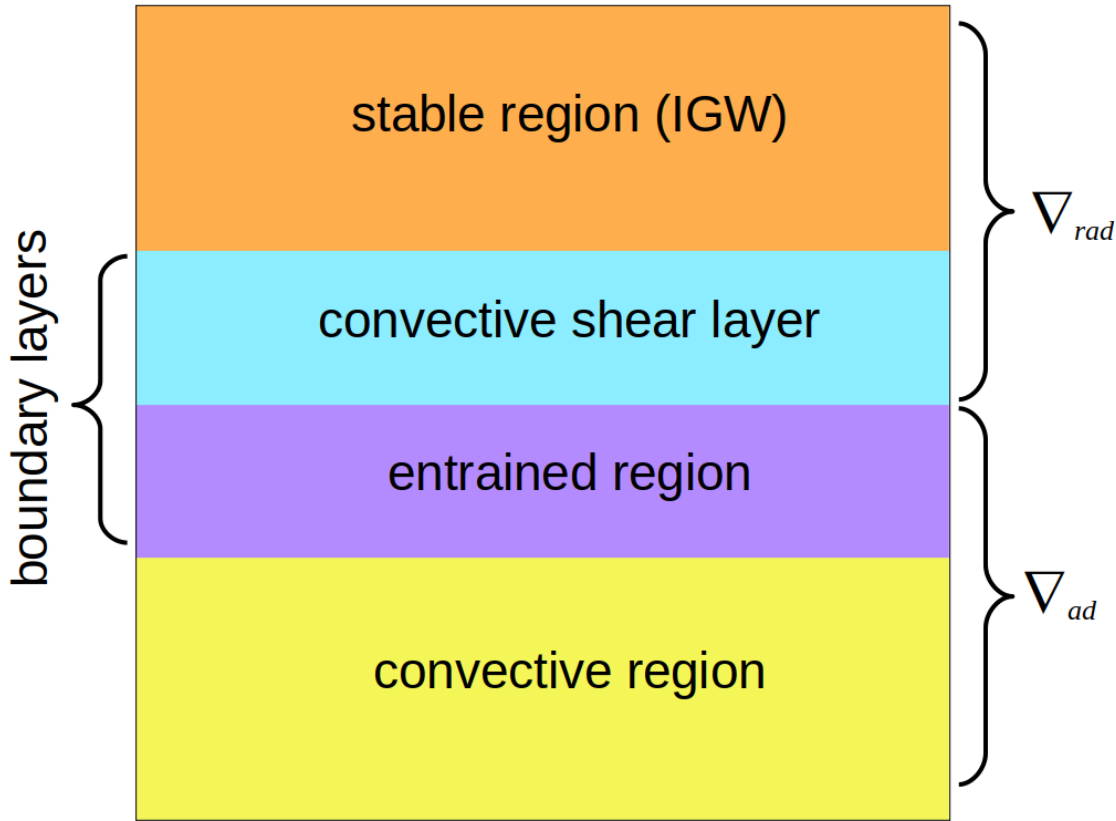


Figure 6.5: Diagram of proposed convective boundary sub-layers. The temperature gradients (as used in **GENEC**) are shown on the right hand side. Internal gravity waves excited by the boundary propagate through the stable region.

mixing. The results of Ch. 5 also suggest that there are two layers contributing to the smooth boundary shape. Therefore, modelling these sub-layers in 1D evolution codes may be beneficial. Figure 6.5 shows a summary of how these layers would appear above a convective core.

The first boundary sub-layer immediately above the core is the entrained region, which is almost instantaneously mixed. In **GENEC**, this region is assumed to have an adiabatic temperature gradient. The size of this region, under the cumulative entrainment prescription, grows with time.

Above the entrained region is a shear layer; the main mixing process in this region

Table 6.1: Properties of three $15 M_{\odot}$ models with different mixing types: pure entrainment, pure shear and an entrainment plus shear combination. Models including entrainment use $n = 1$.

CBM parameters	τ_{MS} [Myr]	$\lg(T_{\text{eff,min}})$ [K]	$M_{\text{He,cc}}$ [M_{\odot}]	$M_{\text{He,1\%}}$ [M_{\odot}]
$A = 10^4$	12.3	4.37	3.72	3.73
$f = 0.03$	11.8	4.36	3.01	3.49
$A = 5 \times 10^{-5}, f = 0.01$	12.3	4.37	3.34	3.50

would be Kelvin-Helmholtz instabilities. This region is partially mixed and modelled using the exponentially decaying diffusion coefficient. In **GENEC**, the temperature gradient here is assumed to be the radiative temperature gradient, as in the stable region above.

The stable region is populated with IGW; in deep convection, these seem to be excited by the rolling of eddies at the boundary. Convective plumes may be a more important source of waves for other convective regions, particularly convective envelopes. In this case, the mixing profile of the waves may well be different to the case of the interior.

In **GENEC**, the shear CBM scheme is in addition to other mixing, rather than replacing it. This means that it can be used in conjunction with entrainment or penetrative overshoot as in Fig. 6.5. In a model with both shear and another form of CBM, the parameter values must be reduced to reproduce quantities such as the MS width seen in a model with only one type of mixing. This is seen in Tab. 6.1, which compares three $15 M_{\odot}$ models: one with pure entrainment, one with pure shear, and the last with a combination of the two. The parameters in the combination model were chosen by halving the entrainment parameter A and reducing the shear parameter f to a level that produces the same MS lifetime as the pure entrainment model. The $f = 0.03$ model is taken as an example of a shear model with a similar MS lifetime and width.

As the models in Tab. 6.1 were chosen to have similar MS lifetimes and widths, their tracks in the HRD are also extremely similar. However, the distinctive effect of

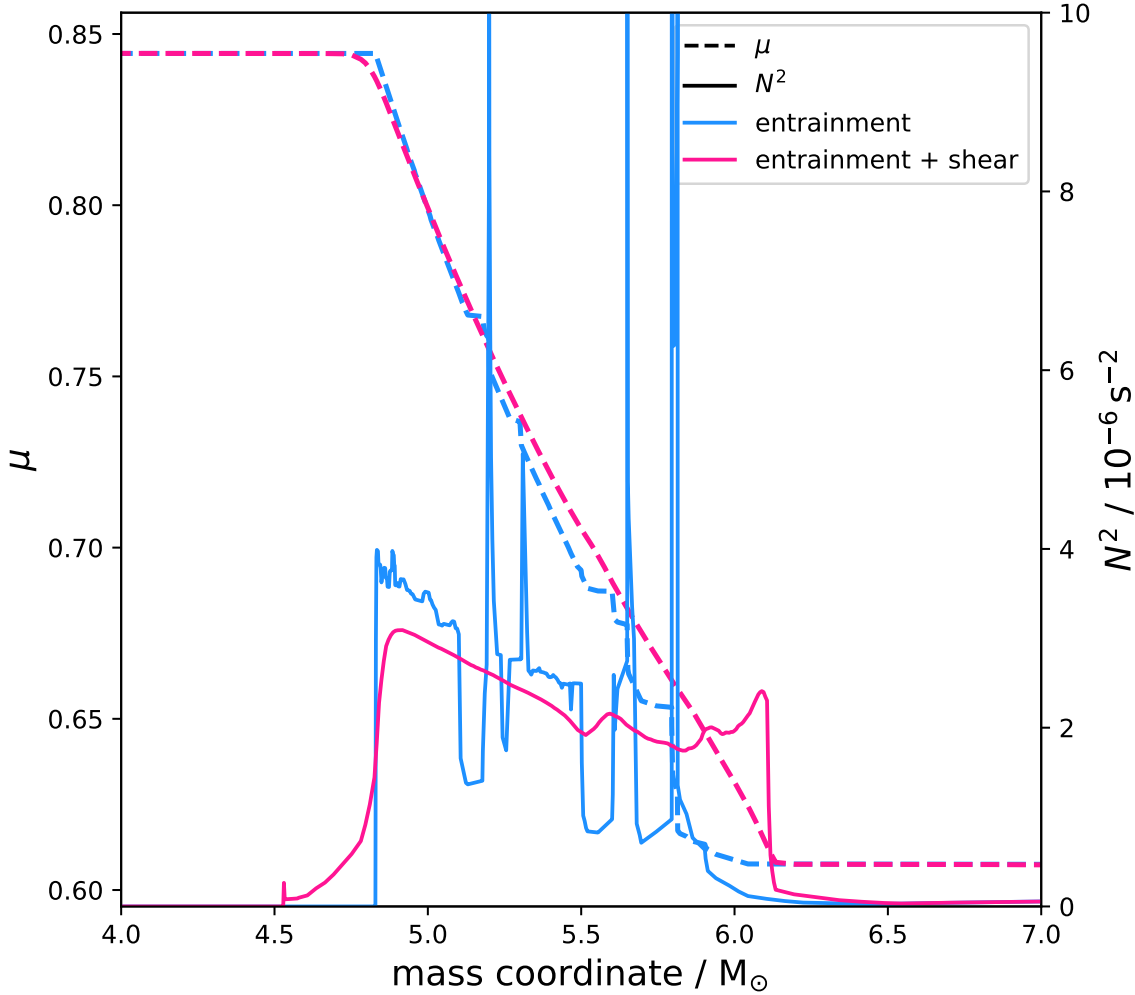


Figure 6.6: Profiles of mean molecular weight, μ (dashed line), and squared buoyancy frequency, N^2 (solid line), for the $A = 10^{-4}$ entrainment model (blue) and the $A = 5 \times 10^{-5}$, $f = 0.01$ combined CBM model (pink) from Tab. 6.1. Both profiles are taken in the middle of the MS at a central hydrogen mass fraction of 0.35.

entrainment on the helium core mass at the end of the MS (using the two definitions used earlier in Tab. 5.1) is apparent, with the pure entrainment model having the largest helium core, followed by the combined model, then the pure shear model with the smallest core.

Other than the helium core size, the other effect of adding shear CBM is to

smooth the chemical abundance profile in the model’s interior. Figure 6.6 compares the profiles of mean molecular weight, μ , and squared buoyancy frequency, N^2 , in the middle of the MS for the pure entrainment and combined CBM models. Despite having no mixing in the stable region, the entrainment plus shear model still has a significantly smoother μ profile. This is because the majority of step-like features on the μ profile, which are essentially numerical features, are caused by the change in size of the convective core over the MS. Thus, a little diffusive mixing on top of the entrained region has the benefit of smoothing numerical features as they are left by the convective core. The gradient of μ is included as part of N^2 , which also becomes smoother in the entrainment plus shear model. Since the integration of N^2 is required for the calculation of the entrainment rate, the model with shear does not suffer from sharp fluctuations in the mass entrainment rate which is seen in the pure entrainment model.

The multi-layered boundary shown in Fig. 6.5 is based on the results of Chs. 4 and 5. However, various boundary structures have been suggested by 2D and 3D simulations and theoretical work. Classically, penetrating plumes were suggested as the mechanism behind CBM for interior convective regions (hence the term penetrative overshoot). Some recent 3D simulations support this on the MS (Edelmann et al. 2019). However, entrainment is also seen to produce similarly strong mixing in other 3D simulations, sometimes even causing convective shells to interact (Andrassy et al. 2020). Therefore, both penetrative plumes and gradual entrainment can result in similar effects over evolutionary timescales. Which process is dominant depends on the properties of the turbulence (Viallet et al. 2015).

Whether the boundary is best described by multiple layers is also contentious. Arnett et al. (2015) suggest that the differing profiles of horizontal and vertical velocities in 3D simulations of convective boundaries are caused by a separate braking region and shear layer (the braking region would be equivalent to the entrained region in Fig. 6.5), hence supporting the presence of both instantaneously mixed and partially mixed layers outside the formal convective region. Multiple CBM regions were also found in the 2D helium shell simulations of Herwig et al. (2007). However this was

only the case for the lower boundary; the upper boundary could be well fitted using a single- f diffusion coefficient. Likewise, Jones et al. (2017) were able to explain the upper boundary shape in their 3D simulations of oxygen shell burning using single- f CBM with $f = 0.03$. In these cases, there is no particular evidence for multiple layers of partial mixing, but the presence of an entrained region is not ruled out.

The fact that the upper and lower boundaries of a convective region in a single simulation (Herwig et al. 2007) can include some of the sub-layers proposed in Fig. 6.5 but not others suggests that the individual mixing processes can be suppressed by the structure present in different regions of a star (and likely different evolutionary phases, too). The fact that IGW are produced by convective boundaries is well known (Press 1981; Rogers & Glatzmaier 2005; Arnett et al. 2019), but their mixing can be significantly weakened in some situations, for example by strong buoyancy (Garcia Lopez & Spruit 1991).

Since the presentation of convective boundaries varies so much between simulations, observational data may be able to rule out many possible boundary structures at different stages in stellar evolution. Asteroseismology can provide valuable constraints on boundary structure since g-mode frequencies are strongly dependent on the size of the resonant cavity, i. e. the outer radiative region. Slowly pulsating B-stars are good targets for these types of observations due to the quantity of g-modes present in their frequency spectra. By calculating the mode spectra of evolutionary models with different CBM structures, the data can be used to confirm or rule out the presence of multiple boundary sub-layers. However, the resonant modes are not the only useful part of the frequency spectrum; Bowman et al. (2019) showed that the low-frequency power excess seen in asteroseismic spectra can be related to the IGWs excited by convective boundaries. Thus, this element of the CBM may also be tested with asteroseismology.

Surface abundances in AGBs and other post-MS stars also present a valuable observational constraint since the formation of the carbon-13 pocket is sensitive to the CBM in both the envelope and the helium shell. This has been important in many studies of CBM and other types of mixing (Boothroyd & Sackmann 1999; Charbonnel & Lagarde 2010; Wagstaff, Miller Bertolami & Weiss 2020). However, the involvement

of more than one convective region (likely with different CBM structures) means that it would be more complicated to constrain CBM in post-MS models than in MS models, due to potential degeneracy in the solutions.

If the properties of the multi-layered boundary can be constrained to some degree, then the next step would be to use 1D models with this boundary structure to initialise 3D simulations. Whilst it is possible that turbulence would simply wipe out any structure present in the initial 1D model (as it appears to in the case of the step-like Schwarzschild boundaries of the initial model of the carbon shell simulations), the new 3D simulations may show different evolution. For example, the softening of the 1D boundary by shear mixing may increase entrainment in the 3D simulation. Since entrainment rates affect the frequency of evolutionary events such as shell mergers (Ritter et al. 2018), this would be a valuable result from the development of new 1D models. The boundary shape may also remain similar in 3D models initialised from 1D models with a new boundary structure. This would also be valuable, since it would demonstrate convergence between the 3D simulation and 1D model boundary shapes.

7 Conclusions

Stellar models are important tools for the astrophysical community, and are instrumental for our understanding of stars. Convection is ubiquitous in stellar evolution, so improving convective boundary mixing in stellar models is a valuable step towards increasing the accuracy of these tools (see Chs. 1 and 2). Hydrodynamic simulations provide an avenue for such improvement; the work in this thesis has used results from these simulations to explore different aspects of convective boundary physics.

7.1 Thesis Summary

The contributions made in this thesis work include the extension of the Geneva stellar evolution code (**GENEC**) with two new CBM prescriptions (Ch. 3). The first of these, the entrainment prescription, translates an entrainment law scheme from 3D simulation results into the 1D code. The cumulative prescription in this work provides an alternative approach to the previous 1D entrainment models of Staritsin (2013). The elements needed for the entrainment prescription (i. e. improved resolution at the convective boundaries, calculation of the boundary stiffness) have also provided general benefits to users of the code. Even outside of the use of the entrainment prescription, these features will improve further research and development of CBM in **GENEC**.

In the analysis of models with entrainment in Ch. 4, the behaviour of the boundary penetrability was analysed, finding a strong mass dependence dominated by the convective velocities. This mass dependence was found to translate into the entrainment prescription, with one set of parameters producing a main sequence width that broadens more strongly with mass than standard CBM. The main sequence widths of the entrainment models were compared to the observations of Castro et al. (2014). They were found to better reproduce the shape of the cool edge of the main sequence than standard CBM models, staying relatively narrow at lower masses whilst becoming very broad at higher masses. An order of magnitude of $\sim 10^{-4}$ was found for the

entrainment law A parameter to produce reasonable main sequence widths and lifetimes, in agreement with the previous work of Staritsin (2013). Due to the difference in implementation, a departure from Staritsin’s results was found in the large cores at the end of the main sequence for the new entrainment models.

The second CBM prescription, the exponentially decaying diffusion coefficient (proposed to model convective shear in stellar interiors) has been implemented in GENE, with both single-slope and double-slope versions and separate parameter values for envelope and interior convective regions. The prescription also allows combination with either entrainment or step overshoot. This will provide a flexible framework for the implementation of multi-layered boundaries for further research into the mixing processes at work in the hydrodynamic simulations.

In Ch. 5, the 3D hydrodynamic simulations of Cristini et al. (2019) were reanalysed with a focus on the convective boundary shape. Comparing boundary shapes between simulations with different energy generation boosting revealed the presence of two layers (a strongly mixed layer and a weakly mixed layer) in the boundary; the relative size of these layers changed with boosting factor, with the mixing in the strongly mixed layer having a stronger dependence on convective velocity. The single-slope shear prescription, whilst able to provide a roughly sigmoid boundary shape, does not replicate the two layers seen in the 3D simulations. The double-slope prescription showed promising results, being closer in shape to the 3D simulation boundaries than the single-slope prescription.

In Ch. 6, the entrainment and convective shear prescriptions were then discussed and compared to other work. A more general model of the convective boundary with multiple layers dominated by different mixing regimes was proposed. The implementations of entrainment and shear in the Geneva code allow this more general boundary structure to be modelled, which will pave the way for future research in this area.

7.2 Future work

To continue on from the work in this thesis, there are several avenues of investigation worth pursuing. The entrainment prescription, having now been successfully implemented in main sequence models, should also be explored in later stages of evolution. In this context it would be useful for e. g. predicting shell mergers whilst taking into account feedback from the boundary stiffness, which can then be investigated in targeted hydrodynamic simulations.

The cumulative prescription in its current form works for convective cores. The ability to track entrainment for multiple convective regions including shells, as would be required in the advanced evolutionary phases, is not possible in the current implementation. The main barrier to an implementation of entrainment for convective shells is the problem of identifying the convective region; this can become complicated if multiple small convective zones appear and disappear, or merge with existing zones.

A potential first step is to track entrainment only for the closest convective region to the core; this would include the carbon shell phase analysed in Ch. 5. For phases where identifying the shell in this way is not practical (e. g. if other convective regions appear and disappear below the shell), the entrainment may be attached to convective regions at a particular mass coordinate. This would clearly only be suitable for studying one or two shells at a time which are expected to appear at a certain position. A full implementation of entrainment for the advanced phases would require an intelligent way of identifying individual shells and dealing with shell mergers.

The temperature gradient used in the CBM region in `GENEC` is currently limited to either adiabatic or radiative, although I have already started putting in the framework for different options. The aim is for the temperature gradient options to be flexible in the same manner as the CBM options, i. e. separate temperature gradients will be defined for different CBM layers. An example would be an instantaneously mixed CBM region on a main sequence convective core, with an adiabatic temperature gradient transitioning to a radiative temperature gradient in a partially mixed layer above. The code will be structured in such a way as to make defining functions controlling the

temperature gradient in the CBM layers simple; this will make further research into more complex boundary structures easier for others using the code.

The re-analysis of the carbon shell models in Ch. 5 showed that the shear prescription with multiple slopes is promising for modelling the boundary shape seen in the 3D hydrodynamic simulations. However, future work should include analysis of different shells to confirm whether the same boundary structure is present. Neon shell simulations by C. Georgy and F. Rizzuti are in progress; it will be informative to repeat the analysis of Ch. 5 for this evolutionary phase. In addition, further work on characterising the mixing due to internal gravity waves would be valuable, since the boundary shape in the 1D models is sensitive to the specific implementation of the double-sloped shear models (e.g. position and gradient of the second slope). The velocity profile of the 3D simulations may also prove useful for calculating a diffusion coefficient directly from the simulation results. This can be compared to the diffusion coefficient profile used in the 1D models and used to verify the existence of the two boundary layers.

Bibliography

Aerts C., Thoul A., Daszyńska J., Scufflaire R., Waelkens C., Dupret M. A., Niemczura E., Noels A., 2003, *Science*, 300(5627), 1926

Aerts C., Molenberghs G., Michielsen M., Pedersen M. G., Björklund R., Johnston C., Mombarg J. S. G., Bowman D. M., Buyschaert B., Pápics P. I., Sekaran S., Sundqvist J. O., Tkachenko A., Truyaert K., Van Reeth T., Vermeyen E., 2018, *ApJS*, 237(1), 15

Aerts C., Mathis S., Rogers T. M., 2019, *ARA&A*, 57, 35

Andrassy R., Herwig F., Woodward P., Ritter C., 2020, *MNRAS*, 491(1), 972

Arnett W. D., Moravveji E., 2017, *ApJL*, 836(2), L19

Arnett W. D., Meakin C., Viallet M., Campbell S. W., Lattanzio J. C., Mocák M., 2015, *Astrophysical Journal*, 809, 30

Arnett W. D., Meakin C., Hirschi R., Cristini A., Georgy C., Campbell S., Scott L. J. A., Kaiser E. A., Viallet M., Mocák M., 2018, *arXiv e-prints*, , arXiv:1810.04659

Arnett W. D., Meakin C., Hirschi R., Cristini A., Georgy C., Campbell S., Scott L. J. A., Kaiser E. A., Viallet M., Mocák M., 2019, *ApJ*, 882(1), 18

Battino U., Pignatari M., Ritter C., Herwig F., Denisenkov P., Den Hartogh J. W., Trappitsch R., Hirschi R., Freytag B., Thielemann F., Paxton B., 2016, *ApJ*, 827(1), 30

Biermann L., 1932, *ZA*, 5, 117

Böhm-Vitense E., 1958, *ZA*, 46, 108

Boothroyd A. I., Sackmann I. J., 1999, *ApJ*, 510(1), 232

- Bowman D. M., Aerts C., Johnston C., Pedersen M. G., Rogers T. M., Edelmann P. V. F., Simón-Díaz S., Van Reeth T., Buysschaert B., Tkachenko A., Triana S. A., 2019, *A&A*, 621, A135
- Briquet M., Aerts C., Baglin A., Nieva M. F., Degroote P., Przybilla N., Noels A., Schiller F., Vučković M., Oreiro R., Smolders K., Auvergne M., Baudin F., Catala C., Michel E., Samadi R., 2011, *A&A*, 527, A112
- Brott I., de Mink S. E., Cantiello M., Langer N., de Koter A., Evans C. J., Hunter I., Trundle C., Vink J. S., 2011, *A&A*, 530, A115
- Canuto V. M., Mazzitelli I., 1991, *ApJ*, 370, 295
- Canuto V. M., Goldman I., Mazzitelli I., 1996, *ApJ*, 473, 550
- Castro N., Fossati L., Langer N., Simón-Díaz S., Schneider F. R. N., Izzard R. G., 2014, *A&A*, 570, L13
- Chabrier G., Baraffe I., 1997, *A&A*, 327, 1039
- Charbonnel C., Lagarde N., 2010, *A&A*, 522, A10
- Chieffi A., Limongi M., 2020, *ApJ*, 890(1), 43
- Claret A., Torres G., 2017, *ApJ*, 849(1), 18
- Claret A., Torres G., 2019, *ApJ*, 876(2), 134
- Cristini A., Meakin C., Hirschi R., Arnett D., Georgy C., Viallet M., Walkington I., 2017, *MNRAS*, 471, 279
- Cristini A., Hirschi R., Meakin C., Arnett D., Georgy C., Walkington I., 2019, *MNRAS*, 484(4), 4645
- Degl’Innocenti S., Prada Moroni P. G., Marconi M., Ruoppo A., 2008, *Ap&SS*, 316(1-4), 25

- Deheuvels S., Brandão I., Silva Aguirre V., Ballot J., Michel E., Cunha M. S., Lebreton Y., Appourchaux T., 2016, *A&A*, 589, A93
- Deng L., Xiong D. R., Chan K. L., 2006, *ApJ*, 643(1), 426
- Denissenkov P. A., Tout C. A., 2003, *MNRAS*, 340(3), 722
- Denissenkov P. A., Herwig F., Woodward P., Andrassy R., Pignatari M., Jones S., 2019, *MNRAS*, 488(3), 4258
- Desmet M., Briquet M., Thoul A., Zima W., De Cat P., Handler G., Ilyin I., Kambe E., Krzesinski J., Lehmann H., Masuda S., Mathias P., Mkrtichian D. E., Telting J., Uytterhoeven K., Yang S. L. S., Aerts C., 2009, *MNRAS*, 396(3), 1460
- Dupret M. A., Thoul A., Scuflaire R., Daszyńska-Daszkiewicz J., Aerts C., Bourge P. O., Waelkens C., Noels A., 2004, *A&A*, 415, 251
- Edelmann P. V. F., Ratnasingam R. P., Pedersen M. G., Bowman D. M., Prat V., Rogers T. M., 2019, *ApJ*, 876(1), 4
- Eggenberger P., Meynet G., Maeder A., Hirschi R., Charbonnel C., Talon S., Ekström S., 2008, *Astrophysics and Space Science*, 316, 43
- Ekström S., Georgy C., Eggenberger P., Meynet G., Mowlavi N., Wyttenbach A., Granada A., Decressin T., Hirschi R., Frischknecht U., Charbonnel C., Maeder A., 2012, *A&A*, 537, A146
- Ertl T., Janka H. T., Woosley S. E., Sukhbold T., Ugliano M., 2016, *ApJ*, 818(2), 124
- Fernando H. J. S., 1991, *Annual Review of Fluid Mechanics*, 23, 455
- Forestini M., Arnould M., Paulus G., 1991, *A&A*, 252(2), 597
- Freytag B., Ludwig H. G., Steffen M., 1996, *A&A*, 313, 497
- Gabriel M., 1995, *A&A*, 302, 271

- Garcia Lopez R. J., Spruit H. C., 1991, *ApJ*, 377, 268
- Georgy C., Saio H., Meynet G., 2014, *MNRAS*, 439, L6
- Gough D. O., 1967, *AJ*, 72, 799
- Herwig F., 2000, *A&A*, 360, 952
- Herwig F., Freytag B., Fuchs T., Hansen J. P., Hueckstaedt R. M., Porter D. H., Timmes F. X., Woodward P. R., 2007, in Kerschbaum F., Charbonnel C., Wing R. F., eds, *Why Galaxies Care About AGB Stars: Their Importance as Actors and Probes*, *Astronomical Society of the Pacific Conference Series Vol. 378*, p. 43
- Herwig F., Woodward P. R., Lin P.-H., Knox M., Fryer C., 2014, *ApJL*, 792(1), L3
- Higgins E. R., Vink J. S., 2019, *A&A*, 622, A50
- Horst L., Edelmann P. V. F., Andr assy R., R opke F. K., Bowman D. M., Aerts C., Ratnasingam R. P., 2020, *A&A*, 641, A18
- Iglesias C. A., Rogers F. J., 1996, *ApJ*, 464, 943
- Jones S., Andrassy R., Sandalski S., Davis A., Woodward P., Herwig F., 2017, *MNRAS*, 465(3), 2991
- Kaiser E. A., Hirschi R., Arnett W. D., Georgy C., Scott L. J. A., Cristini A., 2020, *MNRAS*
- Kippenhahn R., Weigert A., 1990, *Stellar Structure and Evolution*, Springer-Verlag
- Kolmogorov A., 1941, *Akademiia Nauk SSSR Doklady*, 30, 301
- Kuhfuss R., 1986, *A&A*, 160(1), 116
- Landau L. D., Lifshitz E. M., 1959, *Fluid mechanics*, Pergamon Press
- Langer N., Kudritzki R. P., 2014, *A&A*, 564, A52

Langer N., Maeder A., 1995, *A&A*, 295, 685

Langer N., 1986, *A&A*, 164(1), 45

Langer N., Kiriakidis M., El Eid M. F., Fricke K. J., Weiss A., 1988, *A&A*, 192(1-2), 177

Ledoux P., 1947, *ApJ*, 105, 305

Ludwig H.-G., Freytag B., Steffen M., 1999, *A&A*, 346, 111

Maeder A., Mermilliod J. C., 1981, *A&A*, 93, 136

Maeder A., Meynet G., 1989, *A&A*, 210, 155

Maeder A., Meynet G., 1996, *A&A*, 313, 140

Maeder A., Meynet G., 2000, *ARA&A*, 38, 143

Maeder A., 1975, *A&A*, 40(3), 303

Martinet S., Meynet G., Ekström S., Simón-Díaz S., Holgado G., Castro N., Georgy C., Eggenberger P., Buldgen G., Salmon S., Hirschi R., Groh J., Farrell E., Murphy L., 2021, arXiv e-prints, , arXiv:2103.03672

McEvoy C. M., Dufton P. L., Evans C. J., Kalari V. M., Markova N., Simón-Díaz S., Vink J. S., Walborn N. R., Crowther P. A., de Koter A., de Mink S. E., Dunstall P. R., Hénault-Brunet V., Herrero A., Langer N., Lennon D. J., Maíz Apellániz J., Najarro F., Puls J., Sana H., Schneider F. R. N., Taylor W. D., 2015, *A&A*, 575, A70

Meakin C. A., Arnett D., 2007, *Astrophysical Journal*, 667, 448

Meynet G., Maeder A., 1997, *A&A*, 321, 465

Michielsen M., Pedersen M. G., Augustson K. C., Mathis S., Aerts C., 2019, *A&A*, 628, A76

- Miglio A., Montalbán J., Eggenberger P., Noels A., 2008, *Astronomische Nachrichten*, 329(5), 529
- Mocák M., Campbell S. W., Müller E., Kifonidis K., 2010, *A&A*, 520, A114
- Moravveji E., Townsend R. H. D., Aerts C., Mathis S., 2016, *ApJ*, 823(2), 130
- Müller B., 2020, arXiv e-prints, , arXiv:2006.05083
- Müller B., Viallet M., Heger A., Janka H.-T., 2016, *ApJ*, 833(1), 124
- O'Connor E., Ott C. D., 2011, *ApJ*, 730(2), 70
- Paterno L., Ventura R., Canuto V. M., Mazzitelli I., 1993, *ApJ*, 402, 733
- Paxton B., Bildsten L., Dotter A., Herwig F., Lesaffre P., Timmes F., 2011, *ApJS*, 192(1), 3
- Pratt J., Baraffe I., Goffrey T., Constantino T., Viallet M., Popov M. V., Walder R., Folini D., 2017, *A&A*, 604, A125
- Pratt J., Baraffe I., Goffrey T., Geroux C., Constantino T., Folini D., Walder R., 2020, *A&A*, 638, A15
- Press W. H., 1981, *ApJ*, 245, 286
- Renzini A., 1987, *A&A*, 188(1), 49
- Ribas I., Jordi C., Giménez Á., 2000, *MNRAS*, 318(4), L55
- Ritter C., Andrassy R., Côté B., Herwig F., Woodward P. R., Pignatari M., Jones S., 2018, *MNRAS*, 474(1), L1
- Rogers T. M., Glatzmaier G. A., 2005, *MNRAS*, 364(4), 1135
- Rogers T. M., McElwaine J. N., 2017, *ApJL*, 848(1), L1
- Rogers T. M., Lin D. N. C., McElwaine J. N., Lau H. H. B., 2013, *ApJ*, 772(1), 21

Schaller G., Schaerer D., Meynet G., Maeder A., 1992, *A&AS*, 96, 269

Schootemeijer A., Langer N., Grin N. J., Wang C., 2019, *A&A*, 625, A132

Schwarzschild M., 1958, *Structure and evolution of the stars.*, Princeton University Press

Scott L. J. A., Hirschi R., Georgy C., Arnett W. D., Meakin C., Kaiser E. A., Ekström S., Yusof N., 2021, *MNRAS*

Scuflaire R., Théado S., Montalbán J., Miglio A., Bourge P. O., Godart M., Thoul A., Noels A., 2008, *Ap&SS*, 316(1-4), 83

Shaviv G., Salpeter E. E., 1973, *ApJ*, 184, 191

Smartt S. J., 2009, *ARA&A*, 47(1), 63

Stage S. A., Businger J. A., 1981, *Journal of Atmospheric Sciences*, 38(10), 2213

Staritsin E. I., 2013, *Astronomy Reports*, 57(5), 380

Stellingwerf R. F., 1976, *ApJ*, 206, 543

Stephens D., Herwig F., Woodward P., Denissenkov P., Andrassy R., Mao H., 2021, *MNRAS*

Stevens B., Lenschow D. H., 2001, *Bulletin of the American Meteorological Society*, 82(2), 283

Stothers R. B., Chin C.-w., 1997, *ApJL*, 478(2), L103

Sukhbold T., Woosley S. E., Heger A., 2018, *ApJ*, 860(2), 93

Unno W., 1961, *PASJ*, 13, 276

Verma K., Antia H. M., Basu S., Mazumdar A., 2014, *ApJ*, 794(2), 114

Viallet M., Meakin C., Prat V., Arnett D., 2015, *A&A*, 580, A61

- Vink J. S., Brott I., Gräfener G., Langer N., de Koter A., Lennon D. J., 2010, *A&A*, 512, L7
- Wagstaff G., Miller Bertolami M. M., Weiss A., 2020, *MNRAS*, 493(4), 4748
- Weaver T. A., Zimmerman G. B., Woosley S. E., 1978, *ApJ*, 225, 1021
- Woodward P. R., Herwig F., Lin P.-H., 2015, *ApJ*, 798(1), 49
- Young P. A., Arnett D., 2005, *ApJ*, 618(2), 908
- Yusof N., Hirschi R., Meynet G., Crowther P. A., Ekström S., Frischknecht U., Georgy C., Abu Kassim H., Schnurr O., 2013, *MNRAS*, 433(2), 1114
- Zahn J. P., 1991, *A&A*, 252, 179
- Zahn J. P., 1992, *A&A*, 265, 115